



**Politecnico
di Torino**

Politecnico di Torino

Master of Science in Petroleum Engineering

October 2021

**Relationship between porosity type and
petroelastic properties for a complex
carbonate reservoir**

Supervisor:

Professor Laura Valentina Socco

Candidate:

Gabriel Sarantopoulos Bergamaschi

ABSTRACT

The focus of this Thesis is to study the reservoirs of the Sapinhoá field , located in the Santos Basin on the southeastern Brazilian continental margin. The Santos Basin is a huge hydrocarbon province (Faria et al 2017) with a great variety of oil discoveries in the early 2000s at ultra-deep waters carbonate reservoirs. These discovered reservoirs are known as the Pre-Salt province.

The carbonate reservoirs usually are very complex to understand and characterize. Normally they have a great variety of geological facies, diverse composition and distinct petrophysical properties. Particularly, the porosity permeability relationship is one of the greatest uncertainties related to these rocks, and have strong implications in reservoir management.

The purpose of this thesis is to investigate the porosity types and pore geometries, by using the petroelastic properties, with the intention to fully understand the porosity-permeability relation. To investigate these characteristics of these reservoirs, two sets of data from three different vertical wells were evaluated. The first set of data are the wireline logs that went through a petrophysical formation evaluation in order to identify the rock mineralogy, estimate the porosity and classify the porosity types. In addition, laboratory core analysis were used to apply the petroelastic model and also to validated the log analysis.

From this set of data and previous results, a petroelastic model was developed, applying the pore space stiffness method (Mavko & Mukerij, 1995), to proper understand the variation of elastic moduli values of the rocks and its properties. Particularly, models of pore space stiffness that appreciate the variety of pore space geometries showed and differentiate diverse features of the reservoir rocks.

The integration of pore space geometry and the porosity types classification, generated a proposition of three diverse petroelastic classes. These classes represent different porosity types associations, diverse log identities and mostly important, three unique equations to predict the permeability of the reservoir.

ACKNOWLEDGEMENTS

“If I have seen further is by standing on the shoulder of Giants”, Sir Isaac Newton, 1676.

When Isaac Newton wrote a letter to his rival physicist Robert Hooke in February 1676, despite some controversy, many interpret the written sentence as a gesture of modesty, recognizing that all their success came from the accumulation of knowledge generated by their predecessors. For me, this phrase can also be interpreted as an acknowledgment and recognitions to everyone who somehow contributed to the progression of others.

Therefore, I would like to acknowledge everyone who somehow contributed to the construction of my thesis.

I am particularly grateful to the company PETROBRAS for providing the data that allowed all the analysis and studies carried out. Furthermore, considerable part of my knowledge was acquired during more than a decade of working within the company. I specifically thank Eduardo Mezzomo for taking part in my personally required release for studies, as well as for my gradual return to work. To several colleagues who gave me technical support during this period, thank you.

I would also like to thank Politecnico di Torino and its fantastic team of professors, for the opportunity to take this master's degree and expand my knowledge. Special appreciation to my supervisor Prof Laura Valentina Socco.

From a personal point of view, a heartfelt thanks to my family. The constant support of my parents, especially in these years when they helped me take care of my daughters, was essential for my dedication to my studies. The biggest thanks goes to my partner, wife and friend who has always been by my side, especially in these 2 years that were extraordinarily challenging. Without her help during this period with the birth of our daughters, moving between countries and facing the pandemic, the conclusion of this thesis would not be possible.

TABLE OF CONTENTS

Abstract	1
Acknowledgements	2
List of Figures	5
List of tables	8
Nomenclatures	10
1. Introduction	13
1.1. Objectives	13
1.2. Geological Background	13
1.3. Available data	15
1.3.1. Wireline logging data	15
1.3.2. Laboratory Analysis	17
2. Theoretical Background	19
2.1. Carbonates Porosity Classification	19
2.1.1. Choquette & Pray Carbonate Porosity Classification	19
2.1.2. Lucia Carbonate Porosity Classification	20
2.1.3. Porosity-Permeability Relationship	22
2.2. Petroelastic Models	25
2.2.1. Rock Elastic Moduli and Velocity	25
2.2.2. Empirical Wyllie Velocity Model	26
2.2.3. Velocity Models	27
3. Methods and Results	31
3.1. Petrophysical Formation Evaluation	32
3.1.1. Mineral Matrix Analysis	36
3.1.1.1. Methods	36
3.1.1.2. Results	36
3.1.2. Porosity Calculation	45
3.1.2.1. Methods	45
3.1.2.2. Results	46
3.1.3. Porosity Types Identification	53
3.1.3.1. Methods	53
3.1.3.2. Results	54
3.2. Petroelastic Model	59
3.2.1. Elastic moduli model	59
3.2.1.1. Methods	59
3.2.1.2. Results	61
3.2.2. Pore space stiffness assessment	64
3.2.2.1. Methods	64

3.2.2.2. Results	65
3.2.3. Pore Geometry Analysis	68
3.3. Petroelastic Classes	70
3.3.1. Petroelastic Class 1	70
3.3.2. Petroelastic Class 2	73
3.3.3. Petroelastic Class 3	75
3.3.4. Permeability Prediction	78
4. Conclusions	80
References	82

LIST OF FIGURES

1.1	<i>Location of Sapinhoá oil field</i>	14
1.2	<i>Representation of sedimentary facies classification for pre-salt reservoir</i>	15
1.3	<i>Schematic diagram of electronic –acoustic system</i>	18
2.1	<i>Choquette and Pray porosity type classification</i>	20
2.2	<i>Carbonate interparticle pore space classification</i>	23
2.3	<i>Petrophysical vuggy pore space classification</i>	23
2.4	<i>Lucia classes Porosity-Permeability cross plots</i>	24
2.5	<i>Porosity Permeability cross plot with Lucia Classes and the effects of Touching and Separate Vugs</i>	24
2.6	<i>Description of the most important models of elastic properties</i>	27
3.1	<i>Scheme demonstrating the thesis methodology workflow</i>	31
3.2	<i>Description of formation evaluation workflow</i>	32
3.3	<i>Log data composite of well 9-BRSA-594-SPS</i>	33
3.4	<i>Log data composite of well 9-BRSA-928-SPS</i>	34
3.5	<i>Log data composite of well 9-BRSA-1037-SPS</i>	35
3.6	<i>Charts NPOR X RHOZ and DTMatApp x RhoMatApp for well 9-BRSA-938-SPS</i>	37
3.7	<i>Matrix apparent density (RhoMatApp) histogram for well 9-BRSA-928-SPS</i>	37
3.8	<i>Matrix apparent slowness (DTMatApp) histogram for well 9-BRSA-928-SPS</i>	38
3.9	<i>X-Ray diffraction ternary plot for well 9-BRSA-928-SPS</i>	38
3.10	<i>Normalized elemental spectroscopy log curve ternary plot for well 9-BRSA-928-SPS</i>	39
3.11	<i>Charts NPOR x RHOZ and DTMatApp x RhoMatApp for well 9-BRSA-1037-SPS</i>	40
3.12	<i>Matrix apparent density (RhoMatApp) histogram for well 9-BRSA-1037-SPS, zone BVE100</i>	40
3.13	<i>Matrix apparent slowness (DTMatApp) histogram for well 9-BRSA-1037-SPS, zone BVE100</i>	41
3.14	<i>X-ray diffraction ternary plot for well 9-BRSA-1037-SPS</i>	41
3.15	<i>Normalized elemental spectroscopy log curve ternary plot for well 9-BRSA-1037-SPS</i>	42
3.16	<i>Charts NPHI x RHOZ and DTMatApp x RhoMatApp for well 9-BRSA-594-SPS</i>	43
3.17	<i>Matrix apparent density (RhoMatApp) histogram for well 1-BRSA-594-SPS</i>	43

3.18	<i>Matrix apparent slowness (DTMatApp) histogram for well 1-BRSA-594-SPS</i>	44
3.19	<i>X-ray diffraction ternary plot for well 1-BRSA-594-SPS</i>	44
3.20	<i>Density porosity (Phi_Den) histogram for well 9-BRSA-928-SPS</i>	46
3.21	<i>Sonic porosity (Phi_son) histogram for well 9-BRSA-928-SPS</i>	47
3.22	<i>Density-Neutrons porosity (PhiNDxp) histogram for well 9-BRSA-928-SPS</i>	47
3.23	<i>Nuclear Magnetic Resonance effective porosity (nmrPhie) histogram for well 9-BRSA-928-SPS</i>	48
3.24	<i>Density porosity (Phi_Den) histogram for well 9-BRSA-1037-SPS, for zone BVE100</i>	49
3.25	<i>Sonic porosity (Phi_son) histogram for well 9-BRSA-1037-SPS, for zone BVE100</i>	49
3.26	<i>Density-Neutrons porosity (PhiNDxp) histogram for well 9-BRSA-1037-SPS, for zone BVE100</i>	50
3.27	<i>Nuclear Magnetic Resonance effective porosity (nmrPhie) histogram for well 9-BRSA-1037-SPS, for zone BVE100</i>	50
3.28	<i>Density porosity (Phi_Den) histogram for well 1-BRSA-594-SPS</i>	51
3.29	<i>Sonic porosity (Phi_son) histogram for well 1-BRSA-594-SPS</i>	51
3.30	<i>Density-Neutrons porosity (PhiNDxp) histogram for well 1-BRSA-594-SPS</i>	52
3.31	<i>Nuclear Magnetic Resonance effective porosity (nmrPhie) histogram for well 1-BRSA-594-SPS</i>	52
3.32	<i>Interpretation model for NMR T2 distribution in vuggy regions</i>	54
3.33	<i>Porosity type logs composite for well 9-BRSA-928-SPS</i>	55
3.34	<i>Porosity type logs composite for well 1-BRSA-594-SPS</i>	56
3.35	<i>Porosity type logs composite for well 9-BRSA-1037-SPS</i>	57
3.36	<i>Porosity-Permeability cross plot for laboratory analysis for well 9-BRSA-928-SPS</i>	57
3.37	<i>Porosity-Permeability cross plot for laboratory analysis for well 9-BRSA-1037-SPS</i>	58
3.38	<i>Porosity-Permeability cross plot for laboratory analysis for well 1-BRSA-594-SPS</i>	58
3.39	<i>Elastic moduli calculation workflow for well logs</i>	60
3.40	<i>Elastic moduli calculation workflow for core data</i>	61
3.41	<i>Porosity- Kphi cross plot for the laboratory analysis for well 9-BRSA-928-SPS</i>	62
3.42	<i>Porosity- Kphi cross plot for the laboratory analysis for well 9-BRSA-1037-SPS</i>	62
3.43	<i>Porosity- Kphi cross plot for well log analysis for well 1-BRSA-594-SPS</i>	63

3.44	<i>Porosity- Kphi cross plot for well log analysis for well 9-BRSA-928-SPS</i>	63
3.45	<i>Porosity- Kphi cross plot for well log analysis for well 9-BRSA-1037-SPS, for zone BVE100</i>	64
3.46	<i>Porosity-Kdry/Km cross plot for laboratory analysis for well 9-BRSA-928-SPS</i>	65
3.47	<i>Porosity-Kdry/Km cross plot for laboratory analysis for well 9-BRSA-1037-SPS</i>	66
3.48	<i>Porosity-Kdry/Km cross plot for well log analysis for well 1-BRSA-594-SPS</i>	67
3.49	<i>Porosity-Kdry/Km cross plot for well log analysis for well 9-BRSA-928-SPS</i>	67
3.50	<i>Porosity-Kdry/Km cross plot for well log analysis for well 9-BRSA-1037-SPS</i>	68
3.51	<i>Porosity-Kdry/Km cross plot for well log analysis for well 9-BRSA-1037-SPS</i>	69
3.52	<i>Porosity-Kdry/Km cross plot for well log analysis for well 9-BRSA-928-SPS</i>	69
3.53	<i>Porosity-Kdry/Km cross plot for well log analysis for well 1-BRSA-594-SPS</i>	70
3.54	<i>Petroelastic class 1 and porosity types logs composite for well 1-BRSA-594-SPS</i>	71
3.55	<i>Nuclear magnetic resonance T2 logarithmic mean curve histogram for petroelastic class 1</i>	71
3.56	<i>Rock thin section image representing petroelastic class 1</i>	72
3.57	<i>Porosity – Permeability cross plot for laboratory core analysis, filtered for petroelastic class 1</i>	72
3.58	<i>Petroelastic class 2 and porosity types logs composite for well 9-BRSA-928-SPS</i>	73
3.59	<i>Nuclear magnetic resonance T2 logarithmic mean curve histogram for petroelastic class 2</i>	74
3.60	<i>Rock thin section image representing petroelastic class 2</i>	74
3.61	<i>Porosity – Permeability cross plot for laboratory core analysis, filtered for petroelastic class 2</i>	75
3.62	<i>Petroelastic class 3 and porosity types logs composite for well 1-BRSA-594-SPS</i>	76
3.63	<i>Nuclear magnetic resonance T2 logarithmic mean curve histogram for petroelastic class 3</i>	76
3.64	<i>Rock thin section image representing petroelastic class 3</i>	77
3.65	<i>Porosity – Permeability cross plot for laboratory core analysis, filtered for petroelastic class 3</i>	77

3.66	<i>Petroelastic classes and permeability curves logs composite for well 1-BRSA-594-SPS</i>	78
3.67	<i>Petroelastic classes and permeability curves logs composite for well 1-BRSA-594-SPS</i>	79

LIST OF TABLES

1.1	<i>Available data</i>	15
2.1	<i>Petrophysical carbonate porosity type classification comparison</i>	20
3.1	<i>Summary of mean values of porosity (dec) curves for the different</i>	
<i>three well</i>		46

NOMENCLATURES

AT10: Array induction resistivity log, investigation 10 inches (ohm.m)
AT20: Array induction resistivity log, investigation 20 inches (ohm.m)
AT30: Array induction resistivity log, investigation 30 inches (ohm.m)
AT60: Array induction resistivity log, investigation 60 inches (ohm.m)
AT90: Array induction resistivity log, investigation 90 inches (ohm.m)
BVE100: Barra Velha Formation zone 100
BVE200: Barra Velha Formation zone 200
BVE300: Barra Velha Formation zone 300
CA_NORM: Elemental spectroscopy Calcium normalized log (dec)
CALC:CAL: Elemental spectroscopy normalized Calcite (dec)
CALC:DOL: Elemental spectroscopy normalized Dolomite (dec)
CALC:QTZ: Elemental spectroscopy normalized Quartz (dec)
CALC:VDIF: Velocity deviation log (m/s)
CALC:PermClass: Calculated permeability for petroelastic classes (mD)
CBFT2CU: Nuclear magnetic resonance clay bound water cutoff
Cp: compaction factor (unitless)
DEN: Undefined formation density log (g/cm³)
DT: Sonic log (μs/ft)
DTC: Undefined compressional slowness log (μs/ft)
DTCO: Delta T compressional wave, compressional slowness log (μs/ft)
DTfl: Fluid slowness (μs/ft)
DTm: Apparent matrix slowness (μs/ft)
DTMatApp: Matrix apparent slowness (μs/ft)
DTS: Undefined shear slowness log (μs/ft)
DTSM: Detal S shear wave, shear slowness log (μs/ft)
E: Young's modulus (Gpa)
ESPEC: Undefined elemental spectroscopy log
GR: Gamma-ray log (API)
HCAL: Caliper log, Borehole diameter (inches)
LAB:PERM: Routine core analysis permeability (mD)
LAB:POR: Routine core analysis porosity (dec)
M: Compressional wave modulus (GPa)
MG_NORM: elemental spectroscopy Magnesium normalized curve (dec)
NEU: Undefined Neutrons log (dec)
NMR: Nuclear magnetic resonance log
NMRFF: Nuclear magnetic resonance free fluid log (dec)
NMRPERM: Nuclear magnetic resonance permeability (mD)
NMRPHIBW: Nuclear magnetic resonance bound fluid (dec)
NMRPHICBW: Nuclear magnetic resonance clay bound fluid (dec)
NMRPHIConVug: Nuclear magnetic resonance connectec vugs porosity (dec)
NMRPHIE: Nuclear magnetic resonance effective porosity log (dec)

NMRPHIinter: Nuclear magnetic resonance interconnected porosity(dec)
NMRPHIIsoVug: Nuclear magnetic resonance isolated vugs porosity (dec)
NMRPHIMudVug: Nuclear magnetic resonance mud filled vugs(dec)
NMRPHIT: Nuclear magnetic resonance total porosity log (dec)
NMRT2M: Nuclear magnetic resonance log T2 logarithmic mean (ms)
NPHI: Thermal Neutron porosity log (dec)
NPOR: Thermal Neutron porosity log (dec)
Phi_Den: Density porosity log (dec)
PhiNDxp: Density- Neutrons porosity (dec)
Phi_Son: Sonic porosity log (Dec)
PEFZ: Photo-eletric log (uniteless)
RES: Undefined resistivity log (ohm.m)
RHOZ: Formation Density log (g/cm³)
RhoMatApp: Matrix apparent density log (g/cm³)
SI_NORM: Elemental spectroscopy Silicon normalized log (dec)
T2: Nuclear magnetic resonance T2 distribution log
T2cutoff: Nuclear magnetic resonance T2 cutoff for Free Fluid
T2_DIST: Nuclear magnetic resonance T2 distribution log (m³/m³)
Vfl: fluid compressional wave velocity (m/s or Km/s)
Vp: compressional wave velocity (m/s or Km/s)
Vpma: mineral matrix compressional wave velocity (m/s or Km/s)
Vp_{sat}: saturated rock compressional wave velocity (m/s or Km/s)
Vs: shear wave velocity (m/s or Km/s)
Vs_{sat}: saturated rock shear wave velocity (m/s or Km/s)
XRD:CAL: x-ray diffraction normalized Calcite (dec)
XRD:DOL: X-ray diffraction normalized Dolomite (Dec)
XRD:QTZ: X-ray diffraction normalized Quartz (Dec)
α: aspect ratio
K: bulk compressional modulus (Gpa)
Kdry: dry rock bulk modulus (GPa)
Kfl: effective pore fluid bulk modulus (GPa)
Km: mineral matrix bulk modulus (GPa)
Kmv: mineral matrix bulk modulus Voigt average (GPa)
Kmr: mineral matrix bulk modulus Reuss average (GPa)
Kphi: pore space stiffness (GPa)
Kphi_needle: pore space stiffness Needle geometry (GPa)
Kphi_penny : pore space stiffness penny geometry (GPa)
Kphi_sphere: pore space stiffness sphere geometry (GPa)
Kphi_tubes: pore space stiffness tubes geometry (GPa)
Ksat: effective saturated bulk modulus (GPa)
μ: shear modulus (GPa)
μdry: dry rock shear modulus (GPa)

μ_{sat} : effective saturated shear modulus (GPa)
v: Poisson's ratio (uniteless)
 ρ : formation bulk density (Kg/m³ or g/cm³):
 ρ_b : Formation density log (g/cm³)
 ρ_{fl} : **fluid density** (g/cm³)
 ρ_{mat} : apparent matrix density (g/cm³)
 ρ_{sat} : saturated formation bulk density (Kg/m³ or g/cm³)
 ϕ : porosity (dec)

1. Introduction

1.1. Objectives

Techniques that attempt to evaluate elastic properties of carbonate rocks have been developed by several different authors (Xu & Payne 2009; Russell & Smith 2007; Babasafari 2020) with the intention to relate the rock elastic properties with present porosity and fluids. Modeling these properties is a process with a number of uncertainties. The first is related to the composition of the rock, considering that carbonate reservoirs are a mixture of diverse minerals such as Calcite, Dolomite and Quartz. The second uncertainty concerns to the porosity, which can vary by the shape of pore (pore type) and total porosity magnitude. In addition, this complex system can be saturated by different mixture of fluids, made of formation water, oil or gas.

Another complex aspect regarding the carbonate reservoir rocks is the porosity-permeability relationship. For a proper reservoir characterization, the estimation of effective porosity is crucial to calculate the original volume of hydrocarbon in place. Furthermore, the permeability estimation will reflect the flow rates for producing and injecting wells, which will reflect on the economy of a hydrocarbon field.

The Pre-salt reservoirs are a hydrocarbon province, located on the offshore of the southwest Brazil, and it is formed by complex carbonates rocks. Particularly, the porosity permeability relationship is very variable, characterized by extreme permeability variations (4 order of magnitude) for a same range of porosities.

A petroelastic models consist of a set of equations that relate the elastic response of a rock, based on petrophysical properties, such as mineralogy, porosity, pore fluid, pore shape and pore size (Mavko et al. 2009). Particularly, models of pore space stiffness that appreciate the variety of pore space geometries showed and differentiate diverse features of the reservoir rocks. The objective of this thesis is to investigate and develop a petroelastic model, focused on the pore space geometries, for the pre-salt reservoir, as well as identify the present porosity types and suggest petroelastic classes that associate the elastic properties with the pore system.

1.2. Geologic background

The study wells are located on the Sapinhoá oil field in the Santos Basin on the southeastern Brazilian continental margin (Figure 1.1). The Santos Basin is classified as a continental passive margin, formed by the separation of Africa and South America during the Early Cretaceous, in the so-called Brazilian Rift System (Chang et al. 1992). The Santos Basin is a huge hydrocarbon province (Faria et al. 2017) with a great variety of oil discoveries in the early 2000s at ultra-deep waters. These reservoirs are known as the Pre-Salt province.

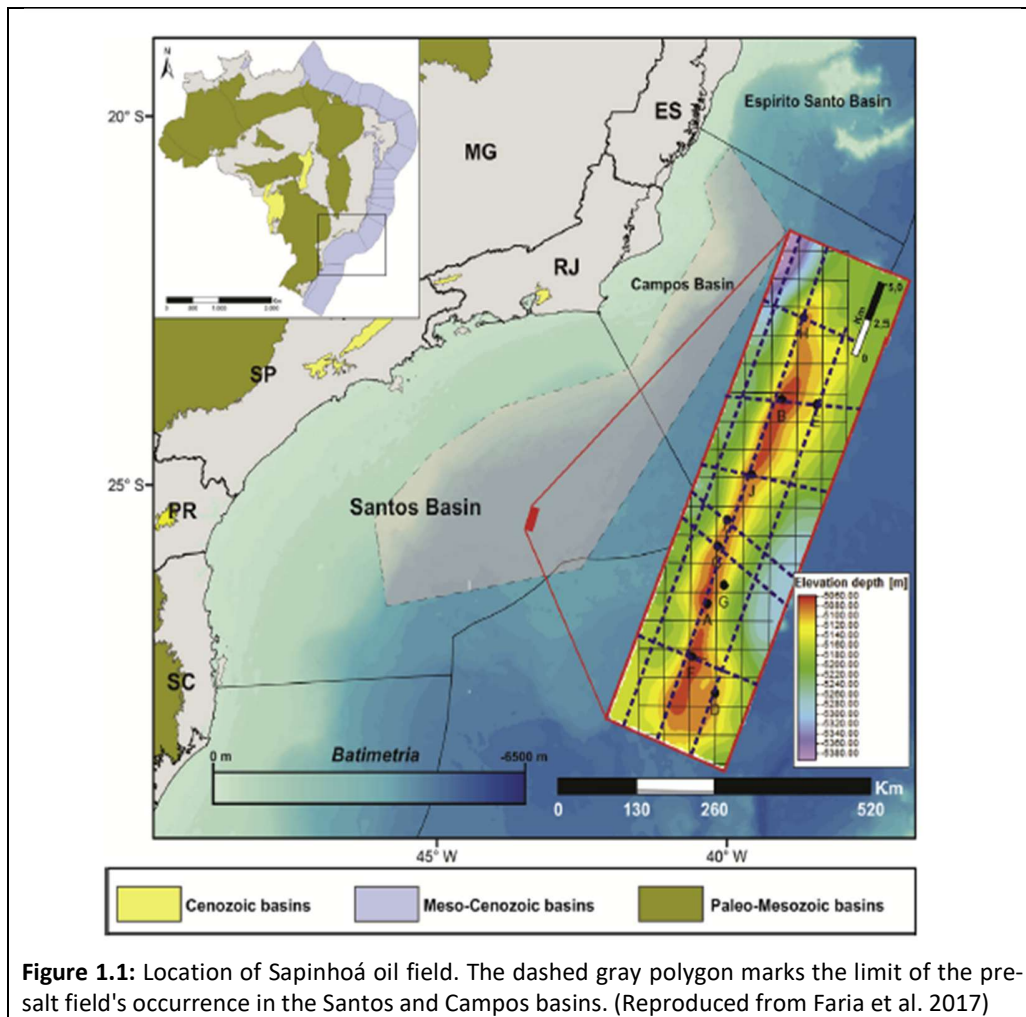


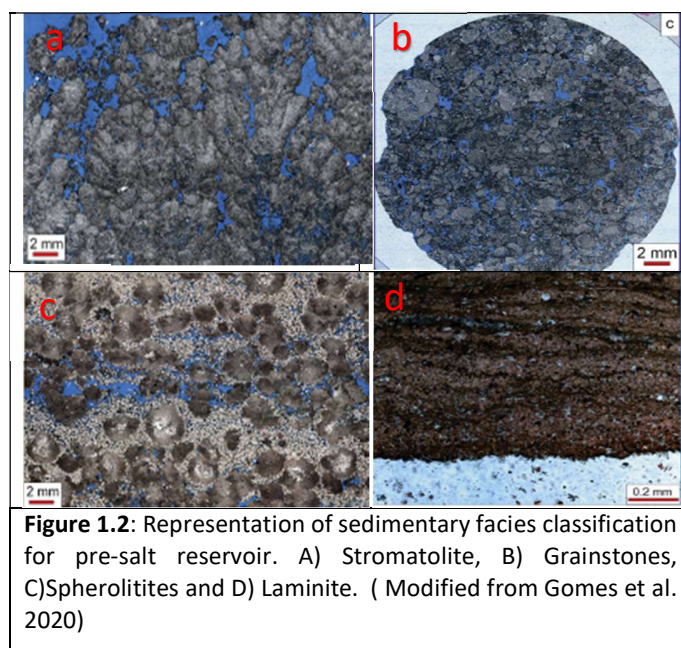
Figure 1.1: Location of Sapinhoá oil field. The dashed gray polygon marks the limit of the pre-salt field's occurrence in the Santos and Campos basins. (Reproduced from Faria et al. 2017)

The Pre-Salt reservoir studied in this thesis were sedimented during the Aptian in a carbonate platform, characterized by a transitional setting between continental to shallow marine conditions (Faria et al. 2017). The upper layer is marked by the presence of evaporites that represent the passage from a mixed clastic-carbonate sedimentary sequence to an evaporitic environment (Moreira et al. 2007). In Santos Basin, the evaporites (halite, anhydrite, sylvite and carnalite) have very thick accumulations reaching more than 2 kilometers (Mohriak et al. 2008).

In terms of stratigraphy, the reservoir belongs to the Barra Velha Formation, Guaratiba Group (Moreira et al. 2007). The depositional model for Sapinhoá Field is interpreted as reservoirs deposited in an isolated carbonatic platform developed in a shallow water horst in a NE-SW orientation, in a long and strait geometry (Naveiro and Haimson 2015).

Four main sedimentary facies can be identified within the stratigraphic sequence of the carbonate platform (Terra et al. 2010): stromatolites, grainstones, laminites and

spherulitites (Figure 1.2). The stromatolites are formed by shrub that are milimetric to centimetric in size, composed of radial fibrous calcite with a single or branched structure (Faria et al. 2017). The grainstones facies are composed mainly by reworked shrubs. The laminites are formed of millimeter sheets of fibrous calcite. The spherulitites facies are composed by symmetric spheres of fibro-radiated calcite (Faria et al. 2017).



The Sapinhoá field has PETROBRAS as Operator and BG E&P Brasil and Repsol Sinopec Brasil as partners. The reservoir fluid is characterized by 29.5° API density and GOR between 231 and 240 m³/m³ (Naveiro and Haimson 2015).

1.3. Available data

To investigate the petroelastic properties and the porosity types of the studied reservoir, the data of three vertical wells were available. Two different sets of data were used, wireline logs and laboratory analysis. The wireline logs were acquired immediately after the end of the drilling phase in 12,25" well diameter, in the presence of synthetic oil drilling mud. The rock samples were extracted or by wireline coring tools (rotary sidewall) or by direct sampling on available hole cores. The well number and the available data for which well is described in table 1.1.

1.3.1. Wireline logging data

Internal PETROBRAS reports were consulted to check for possible problems or occurrences that may affect the quality of the data. The Caliper log (HCAL) represents

a measurement of the well diameter (in inches) and it is an important tool to check the quality of the other logs. The Gamma ray log (GR) is the reading of natural radioactivity of the formation, and it is usually used to identify shaly zones. In our reservoir particularly, the GR curve is useful to stratigraphy correlation and depth correction between curves. The resistivity was acquired using an electromagnetic induction probe that represents the apparent resistivity of the formation. The resistivity curves were used as a saturation indication, to interpret the oil and water bearing zones, and also the oil-water contact.

WELL NUMBER	WELL LOGS	X-RAY DIFRACTION	ROUTINE CORE ANALYSIS			SPECIAL CORE ANALYSIS
			POROSITY	PERMEABILITY	DENSITY	ROCK PHYSICS
1-BRSA-594-SPS	GR-CAL- PEFZ-DEN- NEU-DTC- DTS-RES- NMR-ESPEC	60	264	264	264	24
9-BRSA-928-SPS	GR-CAL- PEFZ-DEN- NEU-DTC- DTS-RES- NMR-ESPEC	1809	1787	1787	1787	96
9-BRSA-1037- SPS	GR-CAL- PEFZ-DEN- NEU-DTC- DTS-RES- NMR-ESPEC	88	507	507	507	15

Table 1.1: Available data. Well logs mnemonics and number of samples analyzed.

Nuclear logs work by the bombardment of gamma rays or neutrons in the formation, and their response indicate the density and porosity of the rocks. The density log (RHOZ) and the neutrons log (NPOR) were used as indicators of porosity and mineral matrix composition. The photo-electric factor curve (PEFZ) can be used as a mineral identifier however, also as a permeability indicator. Permeable zones have the tendency to allow drilling fluid invasion that has dense minerals (barite) in its composition that cause anomalies in the PEFZ curve acquisition.

One of the most important log acquired is the Nuclear Magnetic Resonance. The transverse relaxation time T2 is proportional to the total porosity of the rock formation. Moreover, this porosity measurement is independent of the matrix mineral composition, in contrast with density and neutrons logs. Furthermore, the T2 distribution is proportional with the pore size (and present fluid), and it can be used as porosity type identifier (see Chapter 3 Section 3.1.3).

The spectroscopy log curves are a modern tool that use the elemental spectrum responses to calculate the proportion of elements present in the formation. It is a very valuable tool to interpret the mineral composition of the rock.

The acoustic logging measurements are a part of interest of this thesis. The readings are related to the critical refraction of acoustic wave at the wellbore wall and are useful to porosity, mineral composition and elastic properties estimation. By that, the compressional slowness (DTCO) and shear slowness (DTSM) were implemented in several interpretations of this work.

Information regarding the technologies of acquisitions, processing and presentation of wireline logs, are abundant in literature (Ellis and Singer, 2007), and are not part of this thesis.

All the interpretations and calculations using the logging curves, such as mineral composition, porosity estimation, porosity types identification and the petroelastic model, are presented in the following chapters of this Thesis.

1.3.2. Laboratory Analysis

All the rock core samples were collected or during wireline logging operations (rotary sidewall) or direct core sampling in hole cores. They were transported and analyzed at PETROBRAS Research center.

The core samples preparation consisted in extraction of original fluids, followed by drying in dry oven at 60°C. For the routine core analysis (density, porosity and permeability), the samples were analyzed at confined pressures, similar to values estimated for the reservoirs. These analyses followed the American Petroleum Institute (API RP 40) procedures.

The rock physics tests were carried out by the Rock Physics Laboratory of PETROBRAS Research Center, and consist of measuring elastic wave velocities in rock samples by transmitting ultrasonic pulses under controlled conditions of pressure, saturation and temperature (Figure 1.3).

Rock Physics tests were performed on cylindrical shaped rock samples with a diameter of 1, 1½ or 2 inches. The plugs were tested on the AutoLab 1000™ system, manufactured by New England Research. This measurement system consists of an electronic module, a hydraulic module and a Linux station for data acquisition and processing.

The electronic module has a function generator and a power amplifier that provides a known signal to ceramic material piezoelectric transducers located in the ultrasonic pulse measuring head coupled to the hydraulic module. Piezoelectric transducers transform the electronic signal into mechanical, compression or shear vibration, as

appropriate. After traversing the rock sample, the mechanical vibration is received by another set of transducers, which convert it into an electrical signal. The receiver's electronic signal is analyzed on an oscilloscope after passing through an amplifier. Waveforms are stored in a computer for later analysis.

The system also has devices for imposing pore pressure and confinement pressure, thus allowing the complete simulation of reservoir conditions.

The propagation velocities of elastic waves in rocks are calculated by dividing the length (or diameter, in radial measurement) of the sample, by the travel-time through the sample.

The equipment is periodically calibrated with reference samples to verify the accuracy and repeatability of measurements and also the quality of the waveforms. Considering the uncertainties in the measurements of time and length, the uncertainty in the determination of velocities varies from 1% to 2%, reaching 5% in cases of poorly consolidated samples, with fractures or very heterogeneous, that produce high attenuation of the signal and therefore poor signal-to-noise ratio and higher uncertainty in travel-time readings.

Considering the reservoir effective pressure, the measured values of velocities from axial and radial pressure of 4000psi, were considered as the closest to reservoir conditions.

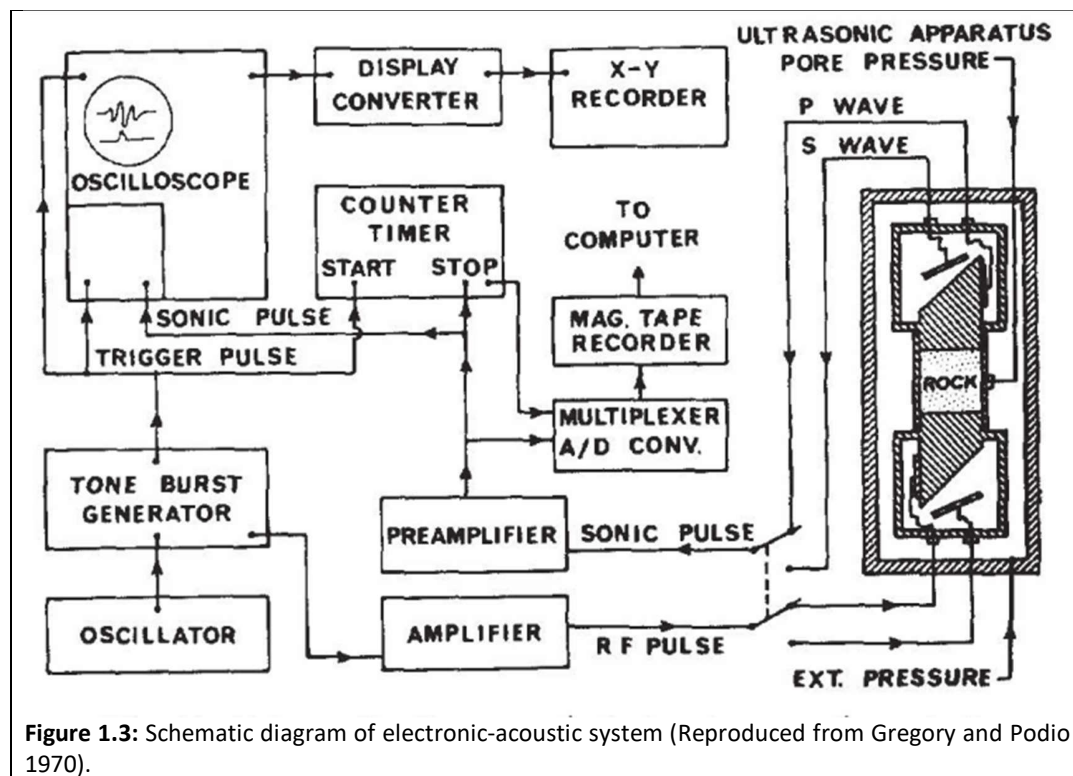


Figure 1.3: Schematic diagram of electronic-acoustic system (Reproduced from Gregory and Podio 1970).

2. Theoretical Background

To improve the characterization of the studied reservoir, two main subjects were taken into account. The first topic regards the importance of understanding the pore system for carbonate rocks, through the theoretical description of the existing porosity types. The understanding of how the pores occur, are formed and are classified by different authors, will facilitate the comprehension of the petrophysical and petroelastic models.

The second topic, aims to appreciate how the theory of elasticity is applied to rocks. As well as a review of methods, that, through the elastic moduli models, manage to describe the rock system, where minerals, fluids and porous space interact. Particularly, understanding what affects compressional velocities in logs and core analysis, is an essential assignment for the petroelastic modelling.

2.1. Carbonates Porosity classification

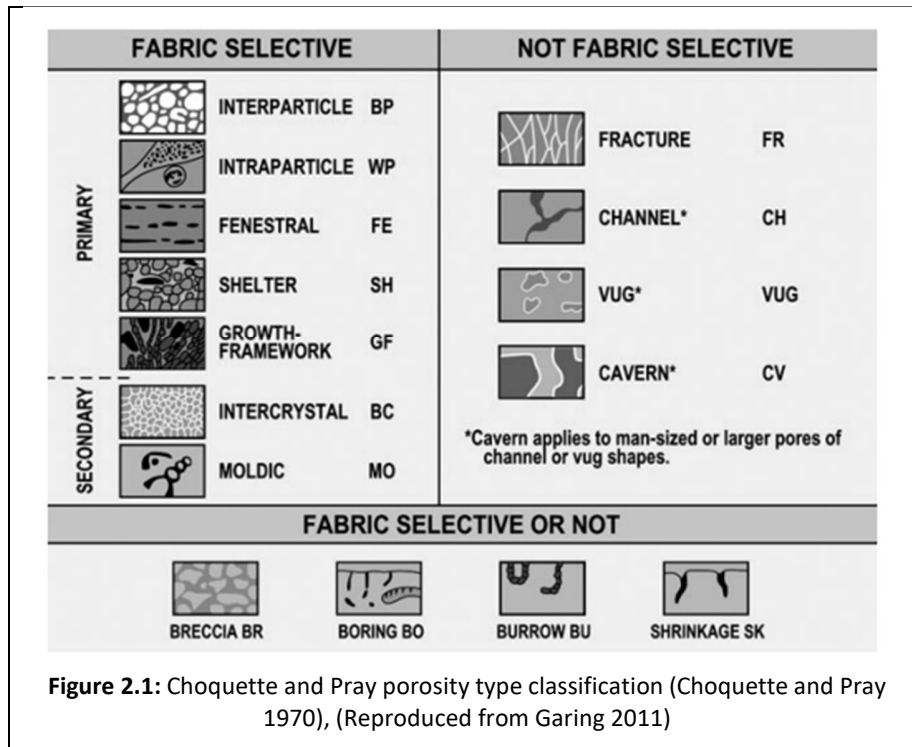
The importance of correctly identifying the characteristics of the carbonates pore space is a crucial step on the reservoir characterization. Not only it will improve the knowledge about sedimentation environments and diagenesis evolution, it also will provide a better understanding of petrophysical parameters that are highly relevant for reservoir simulation. The interaction between the pore space fabric and the present fluids affects the porosity-permeability relationship, therefore, they are crucial to be characterized. Several authors have proposed different carbonate porosity classification through the years, in the following we report the most relevant one for this thesis.

2.1.1 Choquette & Pray Carbonate Porosity Classification

One of the most widely used is the Choquette and Pray classification (Choquette and Pray 1970) in which the carbonates are classified according to pore system genesis. These authors proposed a classification (Figure 2.1) with the intention to clarify the definitions and connotations, once historically, some terms used to have more than one definition (Choquette and Pray 1970). They distinct the types using attributes as pore size, pore shape, genesis and position or association with constituents parts of rock fabric.

An important concept that was introduced was the Fabric selectivity criteria. In Fabric selected pore types, pore positions and pore boundary configurations are determined by the fabric elements. Pores that occur at random positions are considered as non-fabric selective. Although they suggested 15 different porosity types, seven types (interparticle, intraparticle, intercrystal, moldic, fenestral, vug and fracture) are dominant forms in sedimentary carbonates (Figure 2.1). Besides describing a new

classification criterion these authors also discuss that the modification in porosity is a predominant diagenetic process, therefore, the simple sedimentary classification of the rock may well not be sufficient to characterize the porous system.



2.1.2 Lucia Carbonate Porosity Classification

A petrophysical approach to carbonate porosity types was developed by Lucia (Lucia 1983) whose work attempted to understand the relationships between porosity-permeability and the pore system. The foundation of Lucia classification is the concept that pore size distribution controls permeability and saturation (Lucia 2007), and the pore distribution and size are related to rock fabric. The author suggested that the porosity system could be divided into two basic pore networks.

The first, Interparticle porosity, was defined as the pore space located between the particles of the rock (Lucia 1983). The term particle is a general term that can refer to crystals and grains (or any depositional element). The second, vuggy porosity, was defined as the pore space larger or within the particles of the rock, normally presented as irregular cavities (Lucia 1983). Furthermore, the vuggy porosity was separated in two different groups based on how the vugs interconnect (separated vugs or touching vugs).

Differently from Choquette and Pray (1970), for Lucia (1983) the genesis of the pore was irrelevant for the classification (Table 2.1). Lucia (1983) also analyzed the relationship between permeability and these different rocks texture and concluded that the amount of interparticle porosity, vuggy porosity and particle size are necessary to a precise estimation. Other relevant distinction between the two classifications is that Lucia (1983) demonstrated that moldic and intraparticle pores have a different behavior when compared with interparticle and intercrystal pores, consequently they should be grouped separately.

Pore Types		
Intergrain	Moldic	Cavernous
Intercrystal	Intrafossil	Fracture
	Shelter	Solution-Enlarged
Lucia (1983,1995)		
Interparticle	Vuggy	
	Separate	Touching
Choquette and Pray (1970)		
Fabric Selective		Non Fabric Selective

Table 2.1: Petrophysical carbonate porosity type classification comparison (modified from Lucia 2007)

The Interparticle porosity (Lucia 1983) may be better described in geologic terms if sorting and particle size are considered. This approach has similarities with the principles of Dunham's classification (Dunham 1962) which depositional textures (grain or mud support) is used. Lucia however is focused on contemporary rock fabric that includes depositional and diagenetic textures. Therefore, fabrics are divided into grain-dominated, which the most relevant characteristics is the presence of open intergrain porosity, and mud-dominated, that is characterized by the presence of mud in pore space (Lucia 2007) (Figure 2.2).

The addition of vuggy pore space to interparticle pore space alter the petrophysical characteristics by altering the pore space connection (Lucia 2007). Lucia defined Separate-vugs when the vuggy pore space is interconnected only through interparticle pore space. Touching-vugs, in the other hand, occur when vuggy pore space forms an interconnected pore system, independent of interparticle pore space (Figure 2.3).

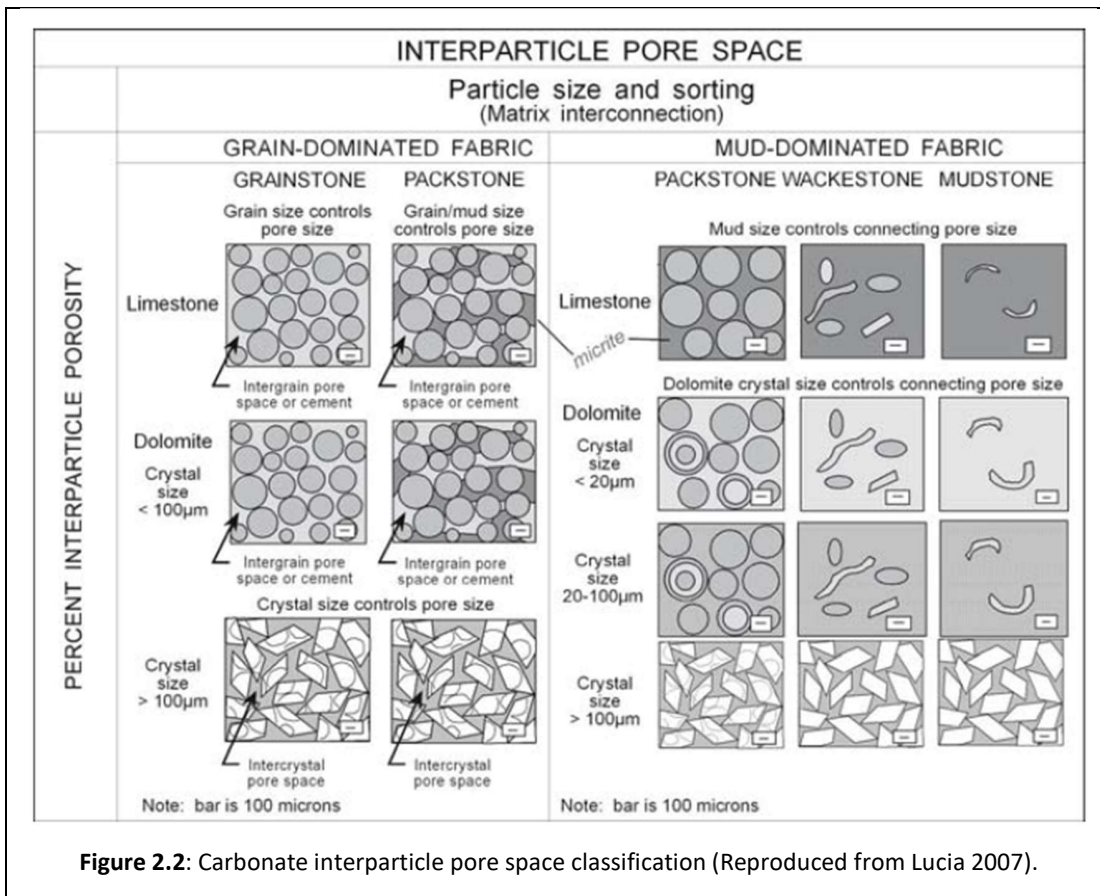


Figure 2.2: Carbonate interparticle pore space classification (Reproduced from Lucia 2007).

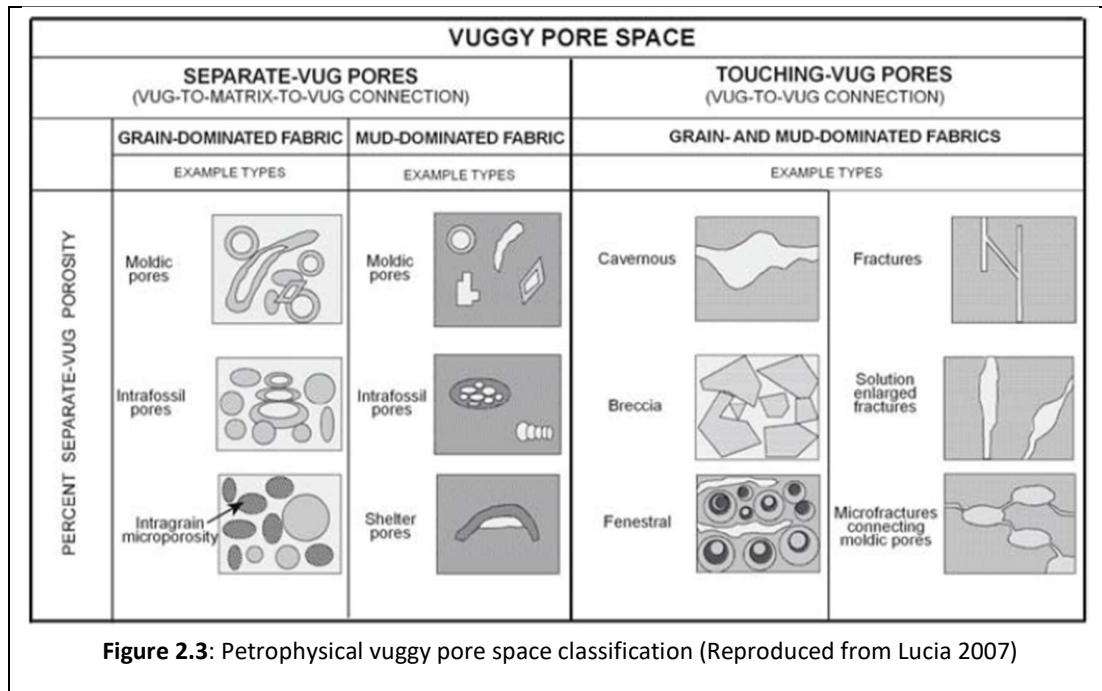
Separate-vug pore space is typically fabric-selective on their origin (Lucia 2007), occurring for example at intrafossil pore space, such as dissolved bivalve or gastropod shells. Shelter porosity, occurring in mud dominated fabrics, is typically larger than the particle size and is also classified as separated-vug pores space. Others examples of separate-vug pore space are intragrain porosity and intragrain microporosity.

Touching –vug pore space are defined as pore is space that is significantly larger than the particle size and has an interconnection creating a pore system with significant extension (Lucia 2007). This pore space is usually non fabric selective in origin. Typical touching-vug pore space are cavernous, collapse breccia, fracture, solution-enlarged fracture and fenestral pore types. Fracture porosity is included in this category because it is normally an important provider to permeability in carbonate rocks.

2.1.3 Porosity Permeability Relationship

Understand the relationship between pore type and permeability is a challenge in carbonate reservoir evaluation (Lonoy 2006). Usually the permeability and porosity data is derived from routine core analysis and related with thin-section description and wireline logs analysis. Porosity-permeability cross plots can be used to predict

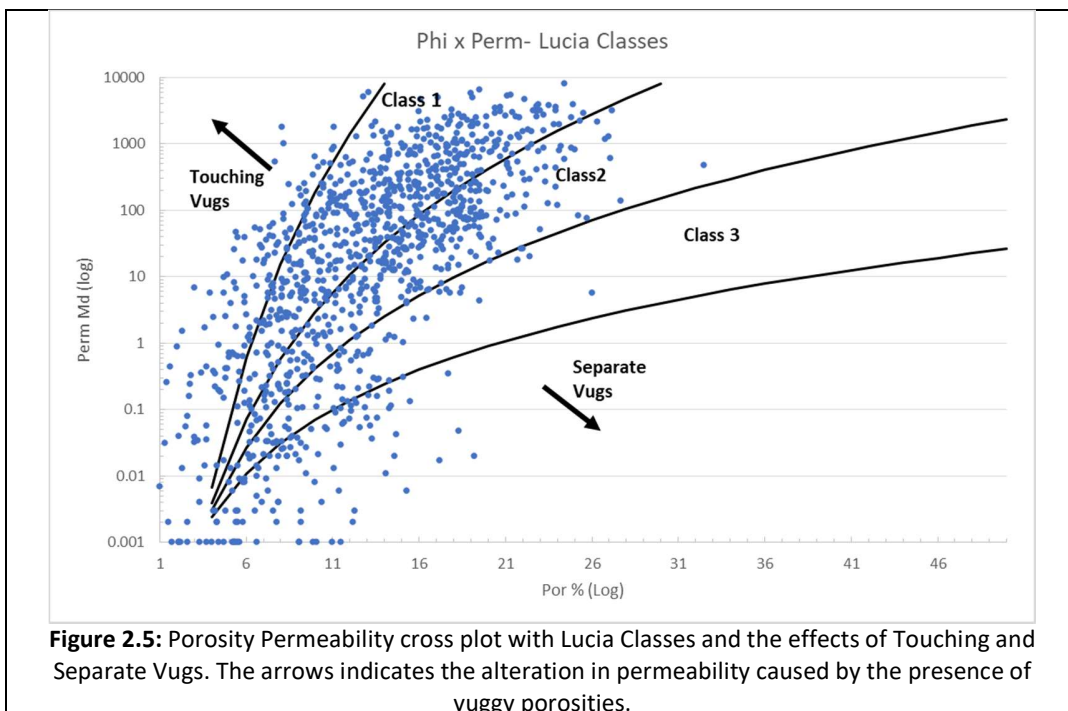
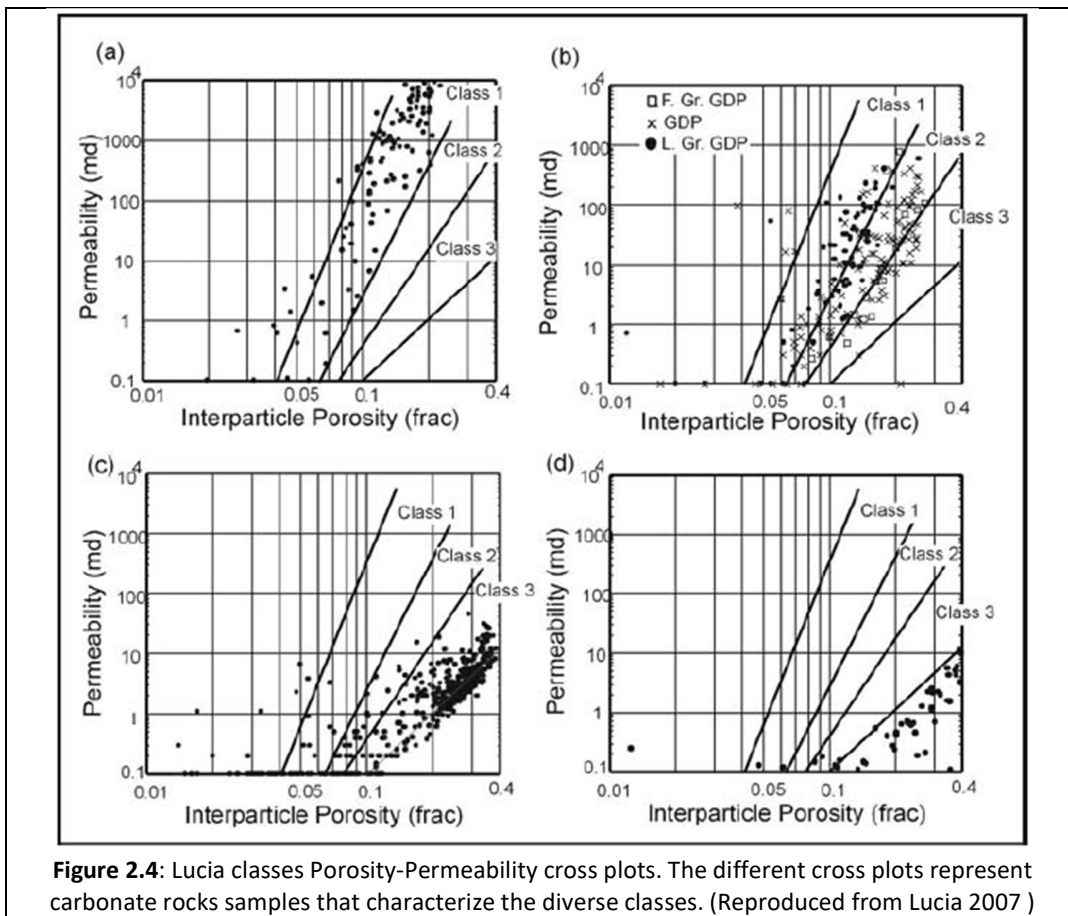
permeability from porosity by establishing mathematical relationships. These relationships can be used after to predict permeability where core analysis are not present by using porosity from logs for example.



Lucia summarized that in the absence of vuggy porosity, pore size distribution in carbonate rocks can be described by particle size, sorting and interparticle porosity (Lucia 1995). The author suggested that for non vuggy rocks examining texture (particle size) and geometry (pore type) should be the basic factor controlling the permeability (Lucia 1983). The effects of adding separate-vugs is to increase porosity with no or little increase on permeability (Lucia 1983). In the other hand, the effect of touching vugs on the rock permeability is to create a higher permeability than expected.

Lucia (1983) demonstrated that three porosity-permeability classes could be defined after analyzing hundreds of core data (Figure 2.4). The author analyzed a great variety of carbonates, from grainstones to mudstones.

Moreover, the position of the sample on the porosity-permeability cross plot could work as a prediction of porosity fabric characteristics. Figure 2.5 illustrates the presence of separate and touching vugs influencing the porosity-permeability relationship. Touching vugs create higher permeability trends, while separate vugs tends to decrease permeability.



2.2. Petroelastic Models

To fully understand and developed a petroelastic model for the studied rocks, it is necessary to cover the basis of the Theory of Elasticity, that will present the most important elastic moduli. The rocks elastic response, in terms of compressional and shear velocity, are proportional to the rock components moduli and density. In addition, the detailing of the velocity models will provide information about effective moduli and the pore space stiffness.

With the intention to compare and validate the theoretical velocity models, empirical and simpler models, such as Wyllie's (Wyllie at al. 1956), will also be considered in this chapter.

2.2.1. Rock Elastic moduli and velocity

The Theory of Elasticity detailed by Timoshenko and Goodier (1934) gives the basis for the description of elastic wave propagation. To proceed with the investigation of the calculations and interpretations on changes on velocity of the carbonates rocks we assume that we are in an isotropic, linear elastic material were the stress and strain are related by Hooke's Law. The following moduli can be used for the description of the elastic properties of a material:

- Young's modulus E , defined as ratio of stress to strain in a uniaxial stress state;
- Compressional wave modulus M , defined as ratio of stress to strain in a uniaxial strain state;
- Bulk compressional modulus K , defined as the ratio of the hydrostatic stress to the volumetric strain,
- Shear modulus μ , defined as ratio of shear stress to shear strain;
- Poisson's ratio ν , defined as the (negative) ratio of lateral strain to axial strain in a uniaxial stress state.

Only two of these moduli are sufficient to define the other ones. Their relations are summarize by diverse authors (Mavko 2009, Schon 2011). The compressional and shear velocities of seismic waves are given by:

$$Vp = \sqrt{\frac{K + \left(\frac{4}{3}\right)\mu}{\rho}} \quad \text{Eq.1}$$

$$V_s = \sqrt{\frac{\mu}{\rho}} \quad \text{Eq.2}$$

Where ρ is the bulk density.

A useful equation relates the Poisson's ratio ν with the ratio of the two wave velocities:

$$\nu = \frac{\left(\frac{V_P}{V_S}\right)^2 - 2}{2\left(\frac{V_P}{V_S}\right)^2 - 1} \quad \text{Eq.3}$$

When we consider the sedimentary rocks velocities two groups can be described. The first are dense rocks, without porosity, such as evaporites (Halite, Anhydrite) with a defined velocity that depends by the mineral properties. The second group are the porous sedimentary rocks, in which the velocities ranges varies due to porosity pore fluid and mineral composition (Schon, 2011). Hydrocarbons reservoir rocks belong on the second group.

The mineralogical influence in velocity is determined by the matrix velocity, that corresponds by the extrapolation of a velocity for porosity equal to zero. Normally in sedimentary porous rocks, with the increase of the porosity the velocity decreases.

Particularly, the velocity-porosity relationships for carbonate reservoirs are complicated due to the diversity of pore types (Schon, 2011).

2.2.2. Empirical Willie Velocity Model

Many authors have tried to identify a relationship between porosity and velocity. One of the most famous work is the Wyllie time-average equation (Wyllie 1965):

$$\frac{1}{V_p} = \frac{1-\Phi}{V_{pma}} + \frac{\Phi}{V_{fl}} \quad \text{Eq.4}$$

Where:

V_p is the compressional velocity of the porous rock;

V_{pma} is the compressional velocity of the matrix mineral;

V_{fl} is the compressional velocity of the pore fluid;

Φ is the total porosity.

This equation has been successfully applied in several different sedimentary environments especially when the rocks have relatively uniform mineralogy, when

they are fluid saturated and at high effective pressure (Mavko et al. 2009). The interpretation of this equation suggests that the total transit time is the sum of the transit time in the mineral matrix plus the transit time in pore fluid (Mavko et al. 2009). Thus, Wyllie's equation is typically used to estimate seismic velocities of rocks and calculate porosity from seismic velocity measurements (sonic logs for example) (Mavko et al. 2009).

However, Wyllie's time-average equation does not have a theoretical meaning, therefore it's application must be made carefully and in controlled situations. It can be applied considering isotropic rocks, fully fluid saturated and with only primary porosity. Particularly for carbonate reservoir rocks, with the presence of secondary porosity as vugs, molds and fractures, the equation tend to miss predict the rock velocities (Mavko et al. 2009).

2.2.3. Velocity Models

For a theoretical description of the rock system, we have to consider that the result of the interaction between minerals, pore geometry and fluid saturation are complex and heterogeneous. In consequence, all theories for elastic rock properties are an idealization with assumptions to simplify the complexity of natural material and make the calculations possible (Schon 2011). Several authors have developed models in the last century and their studies are summarized on the figure 2.6.


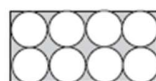

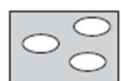
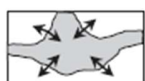
Real rock				
Bound models	Sphere pack models	Inclusion models (Spherical and nonspherical inclusions)		Pore fluid effect models
				
<p>Layer model: Voigt (1910) and Reuss (1926) bounds</p> <p>Hashin–Shtrikman (1962, 1963) bounds</p>	<p>Hertz (1882) and Mindlin (1949) theory</p> <p>Gassmann (1951) White (1983) Digby (1981) Dvorkin and Nur (1996)</p>	<p>Random orientation</p> <p>Kuster and Toksöz (1974)</p> <p>Budiansky and O'Connell (1974)</p>	<p>Aligned orientation</p> <p>Hudson (1980)</p>	<p>Gassmann (1951) Biot (1956)</p> <p>Murphy (1982) Mavko and Jizba (1991)</p>
Delivers upper and lower boundary for a given composition	Describes granular materials, gives nonlinear pressure dependence of velocities	Describes fractured and (low) porous rocks, implements inclusion shape (aspect ratio) and orientation: random orientation (isotropic) or aligned orientation (anisotropic)		Describes influence of changing pore fluid, basic for "fluid replacement techniques".

Figure 2.6: Description of the most important models of elastic properties. (Reproduced from Schon 2011)

Figure 2.6: Description of the most important models of elastic properties. (Reproduced from Schon 2011)

Gassmann (1951) develop a model for porous rocks that allow the prediction of velocities if we consider rocks saturated with one fluid and its substitution for a second fluid (or predict saturated rock velocities from dry-rock velocities) . This model assumes that the rocks are homogeneous, isotropic, with interconnected pores saturated with fluids in a closed system (undrained) condition and that the wavelength of the propagating wave field is larger with respect to the pore scale.

Gassmann-Biot theory (Gassmann 1951; Biot 1956) relates the effective saturated bulk modulus K_{sat} using the equation:

$$\frac{K_{sat}}{K_m - K_{sa}} = \frac{K_{dry}}{K_m - K_{dry}} + \frac{K_{fl}}{\phi(K_m - K_{fl})} \quad \mu_{sat} = \mu_{dry} \quad \text{Eq.5}$$

Where K_{dry} is effective dry rock bulk modulus, K_{fl} is the effective pore fluid bulk modulus, K_m is the mineral material bulk modulus, μ_{sat} is the effective saturated shear modulus and μ_{dry} is the effective dry rock shear modulus.

When we consider fluid replacement techniques (Gassmann 1951), we could assume that the P-velocity (Compressional velocity for saturated rock $V_{p_{sat}}$) and S-velocity (Shear velocity for saturated rock $V_{s_{sat}}$) are:

$$V_{p_{sat}} = \sqrt{\frac{K_{sat} + \left(\frac{4}{3}\right)\mu_{sat}}{\rho_{sat}}} \quad \text{Eq.6}$$

$$V_{s_{sat}} = \sqrt{\frac{\mu_{sat}}{\rho_{sat}}} \quad \text{Eq.7}$$

If we have measured or calculate saturated density and S-velocity values, we can retrieve μ_{sat} :

$$\mu_{sat} = \rho_{sat} (V_{s_{sat}})^2 \quad \text{Eq.8}$$

The value of K_{sat} can be derived from the previous equations, if we have the measured P-velocity:

$$K_{sat} = \rho_{sat} (V_{p_{sat}})^2 - \left(\frac{4}{3}\right)\mu_{sat} \quad \text{Eq.9}$$

The dry rock bulk modulus K_{dry} (Zimmerman 1991) is the reciprocal of the effective dry compressibility, and it is possible to retrieve it from (Mavko et al 2009):

$$K_{dry} = \frac{K_{sat} \left(\phi \frac{K_m}{K_{fl}} + 1 - \phi \right) - K_m}{\phi \frac{K_m}{K_{fl}} + \frac{K_{sat}}{K_m} - 1 - \phi} \quad \text{Eq.10}$$

In addition, the porous rock compressibility is related to the intrinsic mineral compressibility plus and additional compressibility caused by the pore space (Mavko and Mukerji 1995). Assuming K_{phi} as dry-pore space stiffness:

$$\frac{1}{K_{dry}} = \frac{1}{K_m} + \frac{\phi}{K_{phi}} \quad \text{Eq.11}$$

According Biot-Gassmann (Gassmann 1951, Biot 1956) to estimate the effective moduli for porous rocks we must consider the properties of the individual components (minerals), the volume fractions of the components and the geometric details and spatial distributions of the components. A modern discussion and procedures are well developed by Mavko (2009). Bounding methods like Voigt-Reuss establish upper and lower bounds for elastic moduli with no geometrical details (Mavko et al. 2009). A second approach is to assume or investigate the geometry of the inclusion (pores), as initially developed by Zimmerman (1984). These are mathematically convenient shapes and allow quantitative estimates of for example K_{phi} (Mavko et al. 2009).

Therefore, pores, vugs and cracks are modeled as ellipsoidal inclusions in a solid material, with a variation of shape inclusions, from spheres to needles (Schon 2011). These shapes are characterized by the aspect ratio α there is the ratio of a/c , being a , b and c , semi axes of the spheroid (usually $b=c$).

Zimmerman (1984 & 1991) developed and presented the following models and retrieve the equations for K_{phi} :

Spherical cavity (a=b=c):

$$\frac{1}{K_{phi}} = \frac{3(1-\nu)}{Km(1-2\nu)} \quad \text{Eq.12}$$

Penny-Shaped/Oblate Spheroid (a<b=c):

$$\frac{1}{K_{phi}} = \frac{4\left(\frac{c}{a}\right)(1-\nu^2)}{3\pi Km(1-2\nu)} \quad \text{Eq.13}$$

Needle-shaped/prolate spheroid (a>>b=c):

$$\frac{1}{K_{phi}} = \frac{(5-4\nu)}{3Km(1-2\nu)} \quad \text{Eq.14}$$

Two-dimensional tubes:

$$\frac{1}{K_{phi}} = \frac{(13-4\nu-8\nu^2)}{3Km(1-2\nu)} \quad \text{Eq.15}$$

With the indication of the pore geometry, using the pore-space stiffness assessment, it is possible to correlate K_{phi} with the porosity types. According Russel and Smith (2007), for a given pressure, K_{phi} should stay constant over a range of porosities, which also allows the different porosity types to be separated.

3. Methods and Results

The methodology applied in this thesis is divided in three parts (Figure 3.1). The first will, through a basic petrophysical formation evaluation, identify the mineral matrix composition, the porosities values and the porosity types identification, using the laboratory analysis and the electric logs. The mineral composition identification will be the basis for various interpretations that will be performed.

The second part will develop a petroelastic model, by the calculation of the rock moduli, exploring the application of existing petrophysical models. In addition, to investigate the pore geometries, there will be performed a pore space stiffness assessment, using modern techniques that distinct the different pore space shapes.

Finally, the integration of the pore type identification and the pore space geometries, will allow us to identify diverse petroelastic facies. This facies will serve as the basis for an individualization of permeability equations for each rock class.

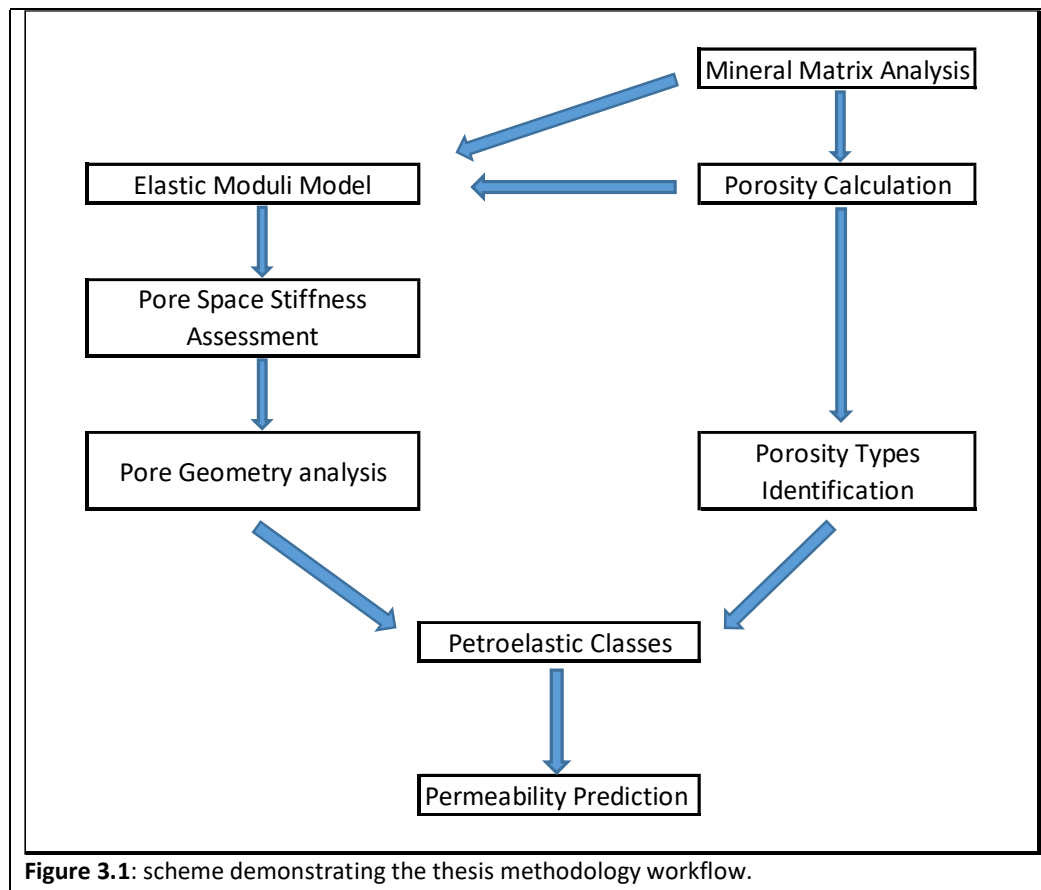


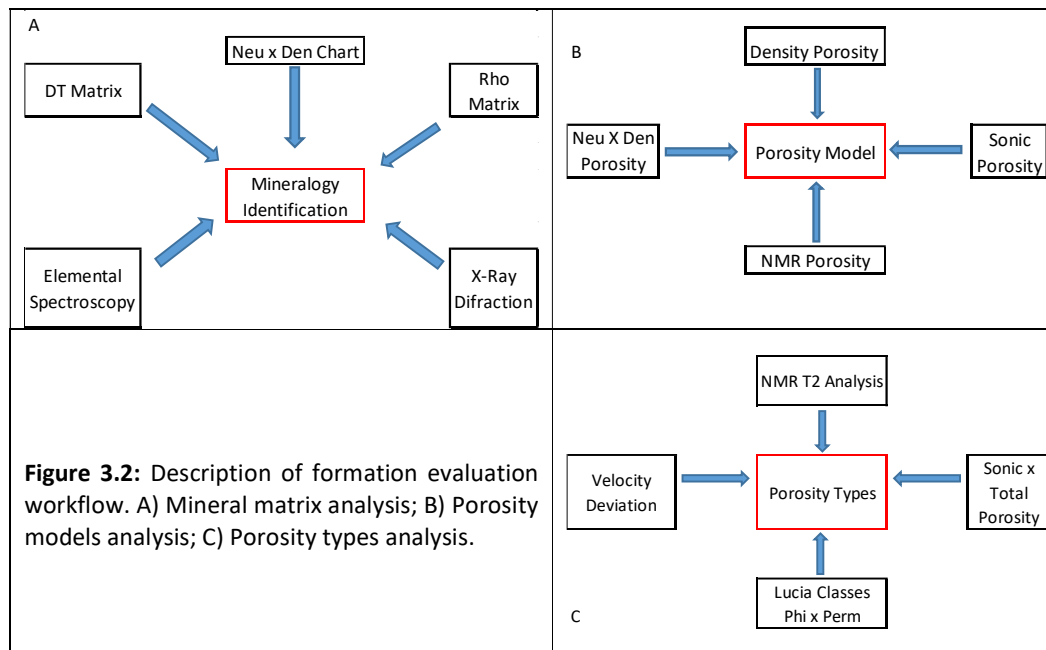
Figure 3.1: scheme demonstrating the thesis methodology workflow.

3.1. Petrophysical Formation Evaluation

The well logs were uploaded at the software Interactive Petrophysics™ and were submitted to a quality control analysis and depth correction were applied where it was necessary. The composite with the well logs can be visualize on the figures 3.3, 3.4 and 3.5.

Our reservoir was divided in three different zones (BVE100, BVE200 and BVE300), that represent a common zonation applied on the production of the reservoir. In wells 1-BRSA-594-SPS and 9-BRSA-928-SPS the three zones are classified as reservoir due to their characteristics of porosity. For the well 9-BRSA-1037-SPS, only the top zone (BVE100) is considered as reservoir, in consequence only this interval is taken into account in the evaluations and analysis.

The petrophysical formation evaluation was divided into three different steps. Firstly the mineral matrix composition was analyzed (Figure 3.2a) with the intention to characterize the proportional of the reservoir minerals. Secondly, the porosity curves were created considering the different composition and the physical principle of each log curve (figure 3.2b). Finally, techniques of pore type identification were implemented to attempt to separate the diverse pore systems (Figure 3.2c). The description of these techniques are described in the following sections.



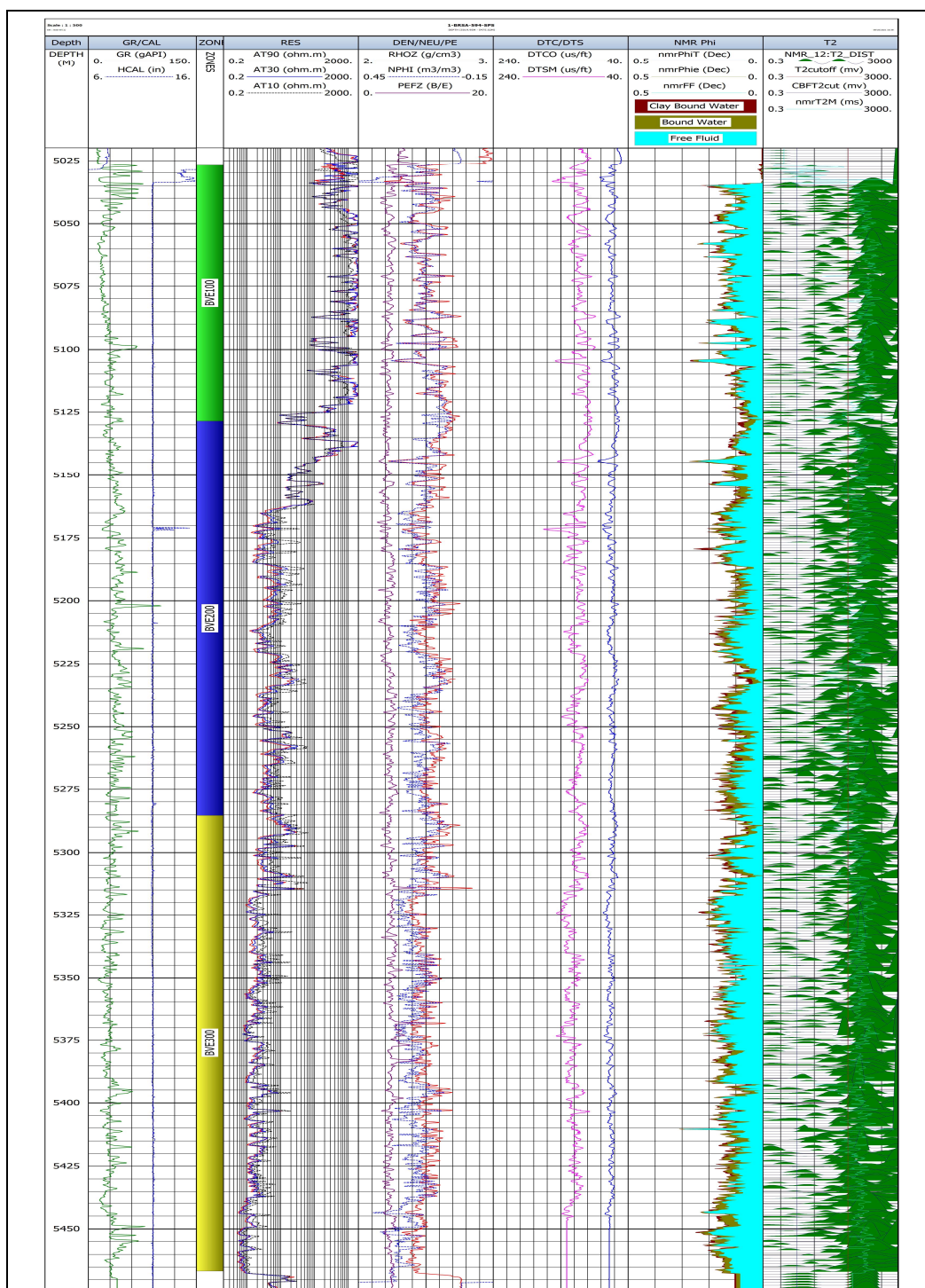


Figure 3.3: Log data composite of well 1-BRSA-594-SPS. Track 1: well depth. Track 2: Gamma-Ray (GR) and caliper (HCAL). Track 3: Zonation of well, zone BVE100 in green, BVE200 in blue and BVE300 in yellow. Track 4: Induction electric resistivity, investigation depths of 10, 30 and 90 inches. Track 5: Density (RHOZ), Neutrons (NPHI) and photoelectric factor (PEFZ). Track 6: Compressional wave slowness (DTCO) and Shear wave slowness (DTS). Track 7: Nuclear Magnetic Resonance porosity curves, Total porosity (nmrPHIT), Effective porosity (nmrPHIE) and Free Fluid (nmrFF). Track 8: NMR T2 distribution and NMR T2 logarithmic mean.

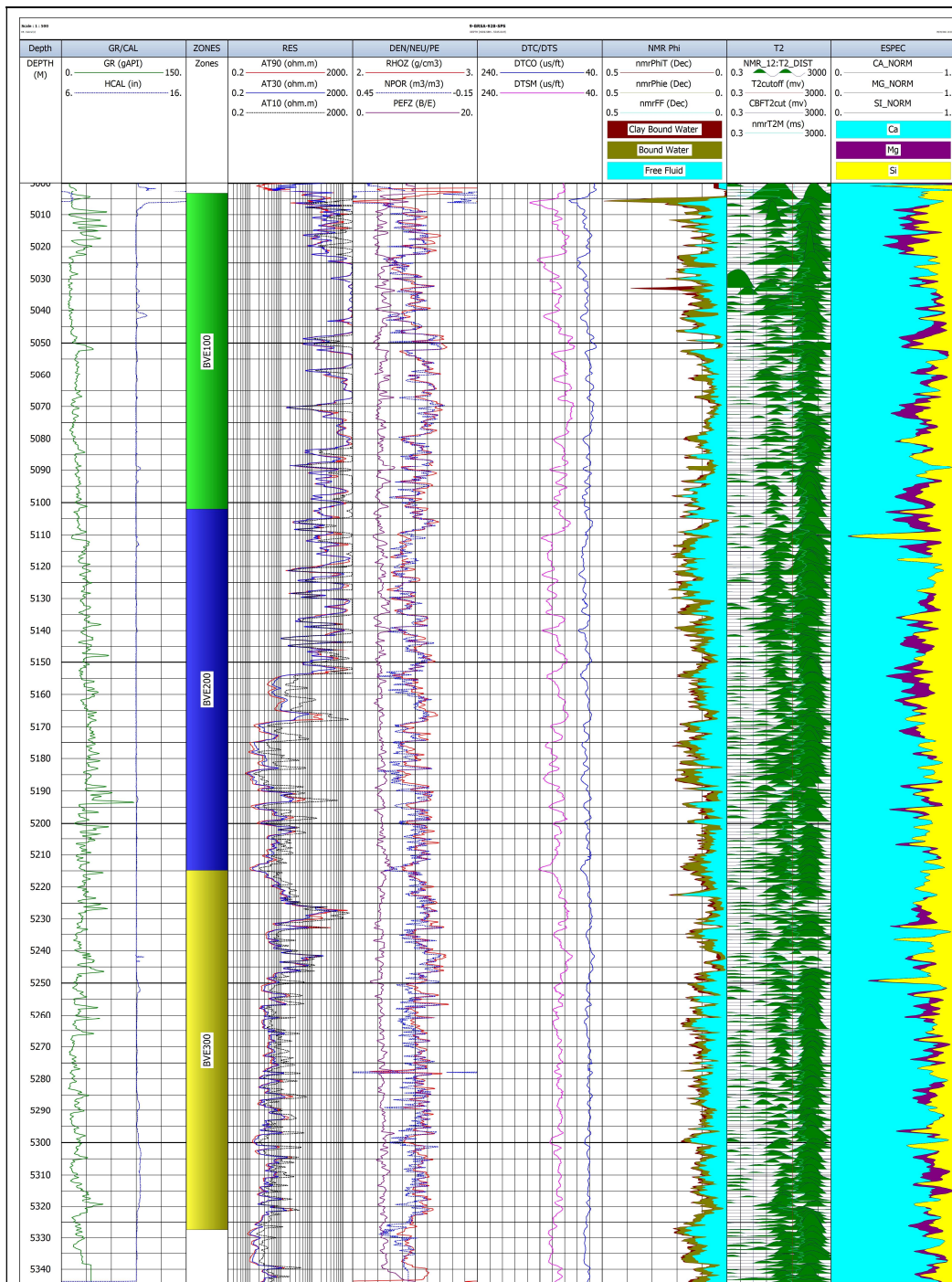


Figure 3.4: Log data composite of well 9-BRSA-928-SPS. Track 1: well depth. Track 2: Gamma-Ray (GR) and caliper (HCAL). Track 3: Zonation of well, zone BVE100 in green, BVE200 in blue and BVE300 in yellow. Track 4: Induction electric resistivity, investigation depths of 10, 30 and 90 inches. Track 5: Density (RHOZ), Neutrons (NPHI) and photoelectric factor (PEFZ). Track 6: Compressional wave slowness (DTCO) and Shear wave slowness (DTS). Track 7: Nuclear Magnetic Resonance porosity curves, Total porosity (nmrPHIT), Effective porosity (nmrPHIE) and Free Fluid (nmrFF). Track 8: NMR T2 distribution and NMR T2 logarithmic mean. Track 9: Elemental spectroscopy curves, Normalized Calcium (Ca_Norm), normalized Magnesium (Mg_Norm) and normalized Silicon (Si_Norm).

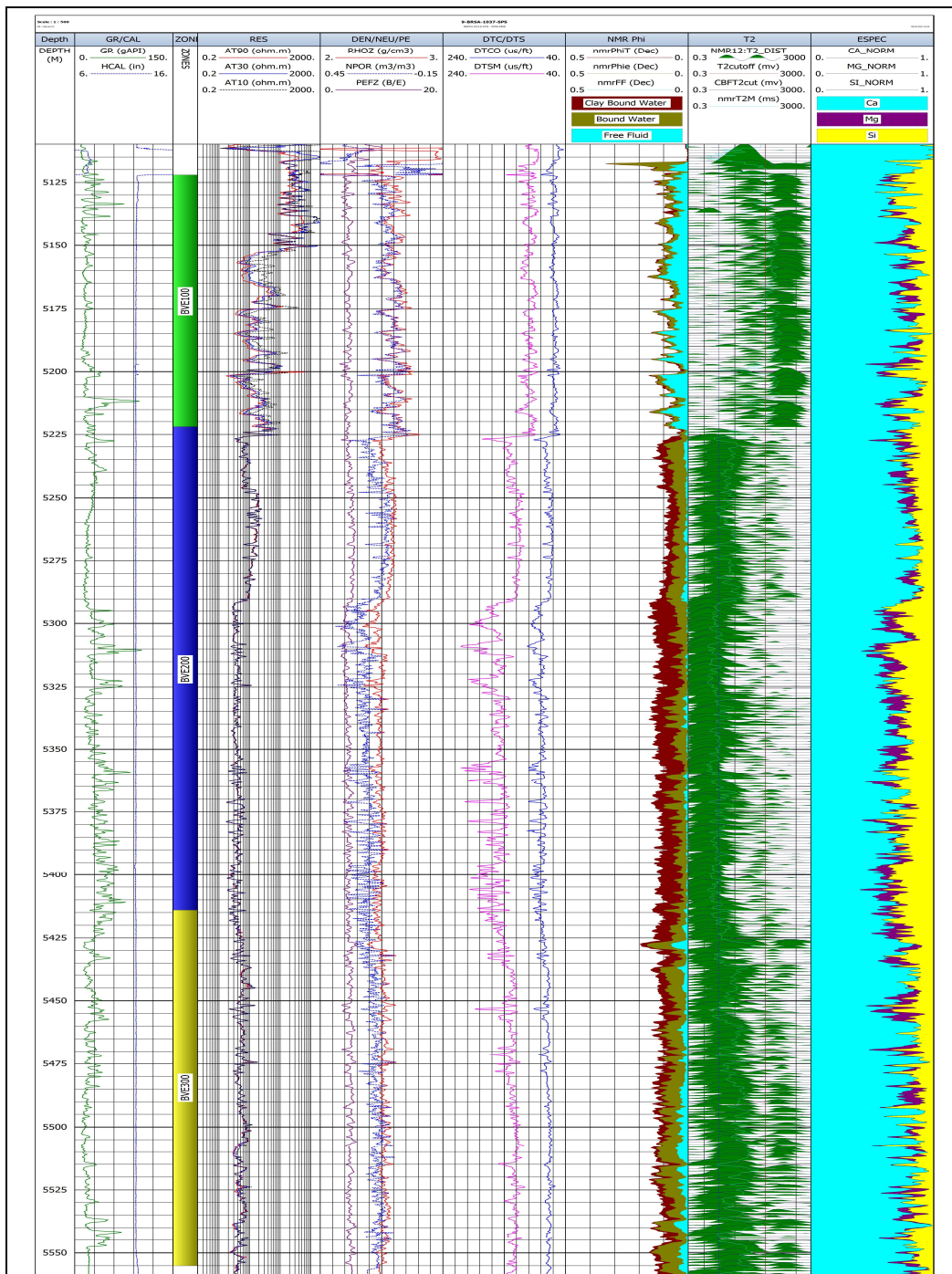


Figure 3.5: Log data composite of well 9-BRSA-1037-SPS. Track 1: well depth. Track 2: Gamma-Ray (GR) and caliper (HCAL). Track 3: Zonation of well, zone BVE100 in green, BVE200 in blue and BVE300 in yellow. Track 4: Induction electric resistivity, investigation depths of 10, 30 and 90 inches. Track 5: Density (RHOZ), Neutrons (NPHI) and photoelectric factor (PEFZ). Track 6: Compressional wave slowness (DTCO) and Shear wave slowness (DTSN). Track 7: Nuclear Magnetic Resonance porosity curves, Total porosity (nmrPHIT), Effective porosity (nmrPHIE) and Free Fluid (nmrFF). Track 8: NMR T2 distribution and NMR T2 logarithmic mean. Track 9: Elemental spectroscopy curves, Normalized Calcium (Ca_Norm), normalized Magnesium (Mg_Norm) and normalize Silicon (Si_Norm).

3.1.1. Mineral Matrix Analysis

3.1.1.1. Methods

The mineral matrix examination was performed by the application of well log evaluation techniques for the three different wells. The Neutrons versus Density log chart was created, within the presence of the different mineral matrix lines (Sandstones, Limestones and Dolostones). In addition, the calculation of the apparent matrix density (RhoMatapp) and slowness (DtMatApp) were performed and a cross plots were created.

To refine the data analysis histograms of apparent matrix density and slowness were produced to retrieve the mean and mode values and the statistic distribution of the calculated values.

To complete the mineral matrix analysis, the X-ray diffraction results for mineral compositions were normalized for Calcite, Dolomite and Quartz. The results were plotted in a composition ternary diagrams. In addition, a mineral composition ternary diagram was produced using the elemental spectroscopy log curves, again normalized for Calcite, Dolomite and Quartz. The analysis was performed individually for each well, as can be see below.

3.1.1.2. Results

- **9-BRSA-928-SPS**

By analyzing the mineral matrix charts for the well 9-BRSA-928-SPS (Figure 3.6), it can be observed that the mineral matrix has a composition between limestones and dolostones. The different zones present similar composition.

The histogram of RhoMatApp (Figure 3.7) shows an average of 2,8g/cm³ of density, indicating an average value between the calcite and dolomite values. The DTMatApp histogram (Figure 3.8) shows a mean value (47,9 μSec/Ft) that represents, again, a mixture of dolomite and calcite.

The ternary plot of X-ray diffraction (Figure 3.9) analysis shows a relevant variety of mineral composition. Particularly, when compared with the ternary plot of the elemental spectroscopy curve (Figure 3.10), it can be observed the presence of samples with a high content of quartz. The ternary plot of normalized elemental spectroscopy log (Figure 3.10) indicates a higher content of calcite and lower presence of quartz. This can be explained by the lower vertical resolution of the logging tool and a possible a weak ability of the technology in identifying the silicon element.

By this comparison, we can observe that all the different techniques presents consistent results, indicating the rock matrix is predominantly a mixture of calcite and dolomite, with local influence of quartz. The elemental spectroscopy log curve is understood as good compositional curve and will be used as a mineralogy indicator.

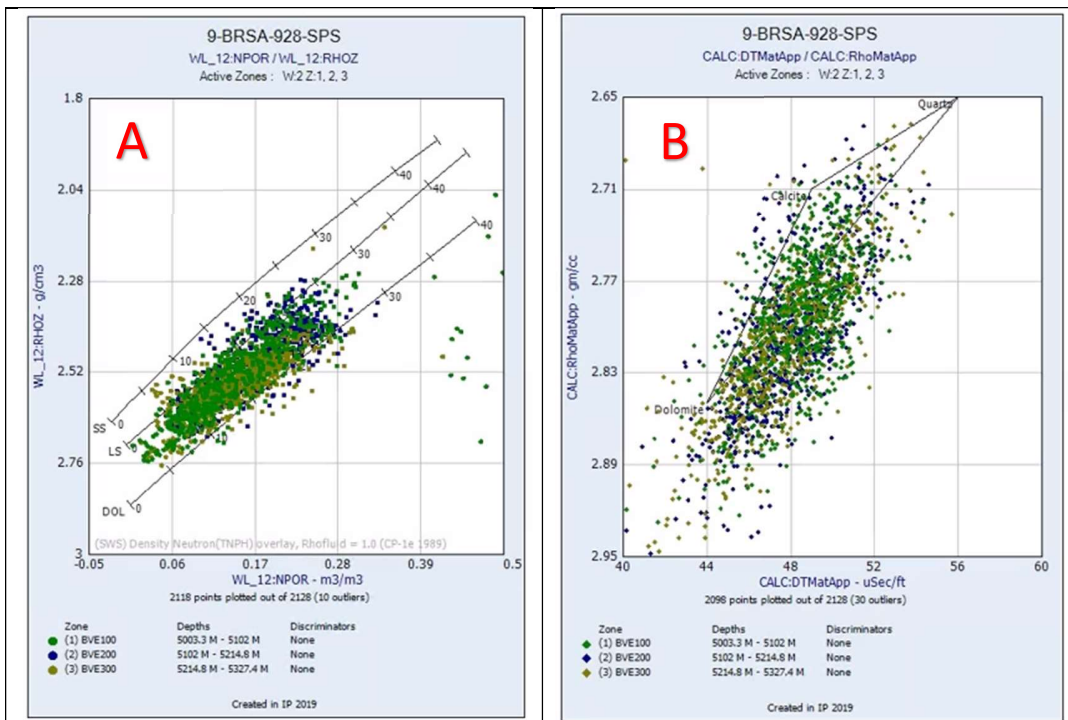


Figure 3.6: Charts NPOR X RHOZ and DTMatApp x RhoMatApp for well 9-BRSA-928-SPS. **A:** Vertical axis is RHOZ and horizontal axis is NPOR. The overlay lines represents the mineral matrix lines. The points different colors represent the different well zones BVE100, BVE200 and BVE300. **B:** Vertical line is apparent matrix density (RhoMatApp). Horizontal axis is apparent matrix slowness (DTMatApp). The vertices of overlay triangle are the minerals calcite, quartz and dolomite. The points different colors represent the different well zones BVE100, BVE200 and BVE300.

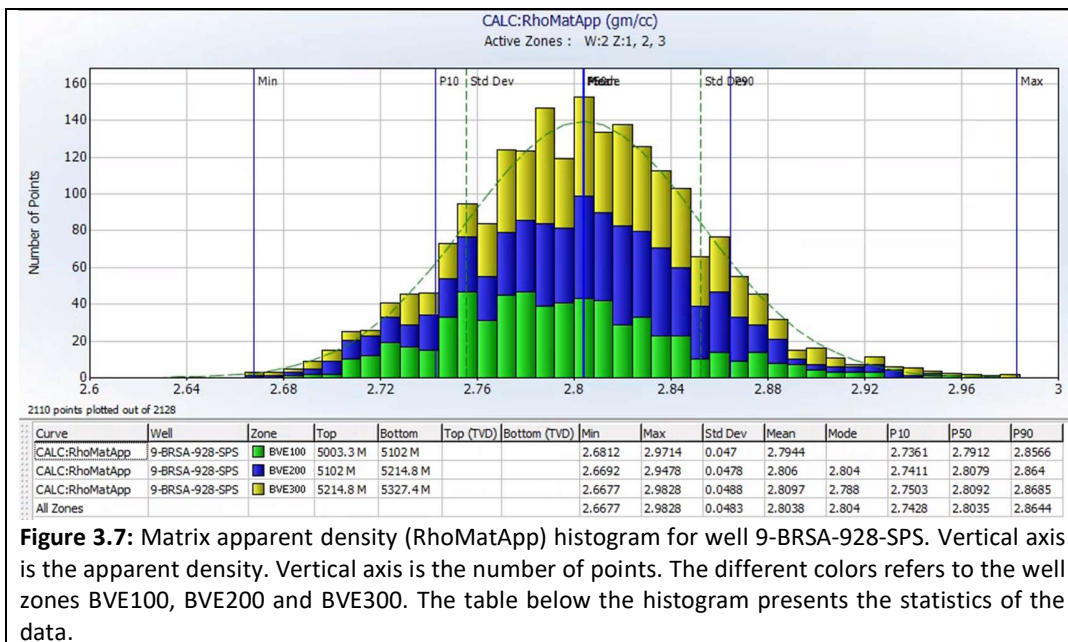


Figure 3.7: Matrix apparent density (RhoMatApp) histogram for well 9-BRSA-928-SPS. Vertical axis is the apparent density. Vertical axis is the number of points. The different colors refers to the well zones BVE100, BVE200 and BVE300. The table below the histogram presents the statistics of the data.

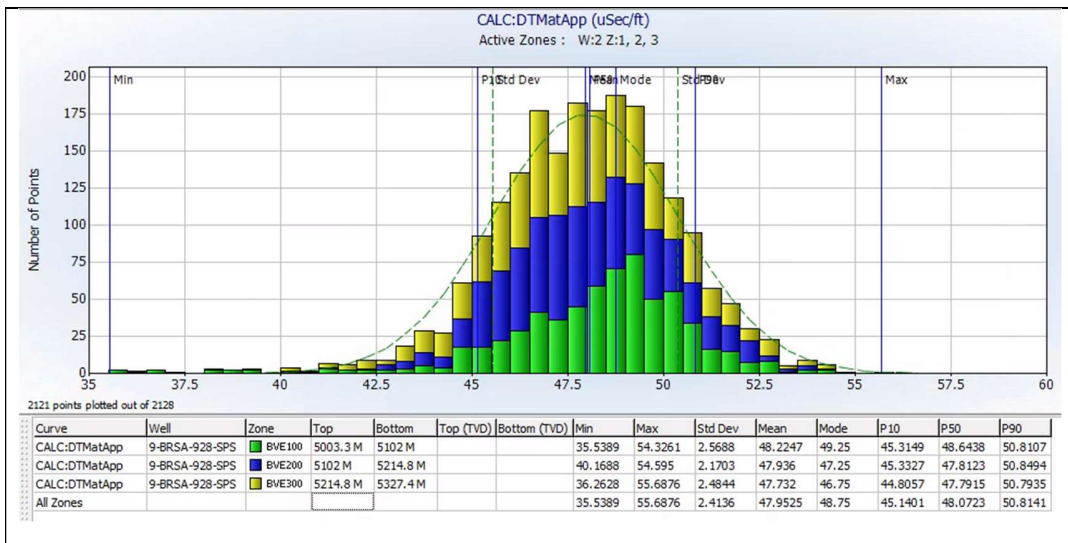


Figure 3.8: Matrix apparent slowness (DTMatApp) histogram for well 9-BRSA-928-SPS. Vertical axis is the apparent slowness. Vertical axis is the number of points. The different colors refers to the well zones BVE100, BVE200 and BVE300. The table below the histogram presents the statistics of the data.

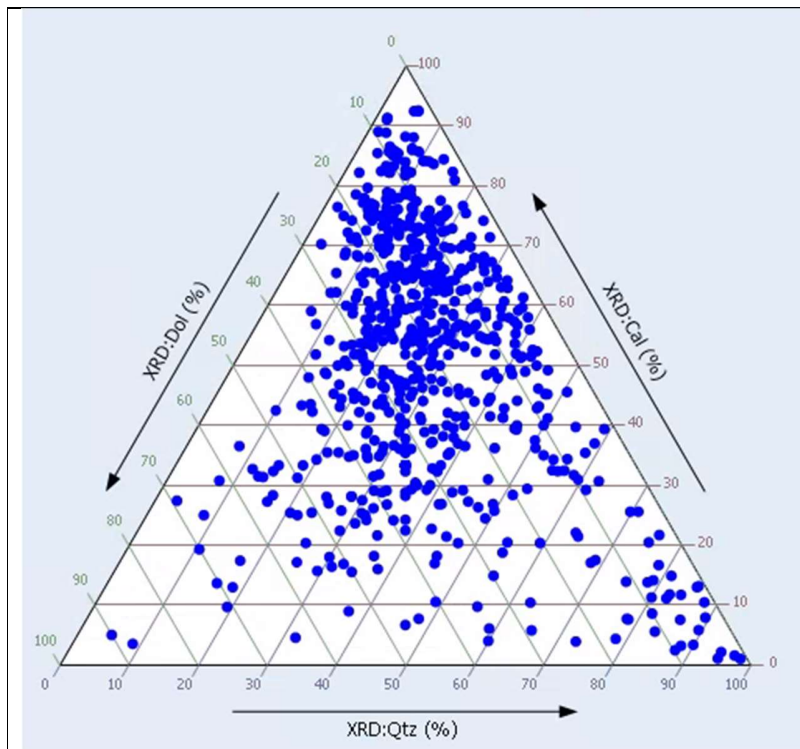
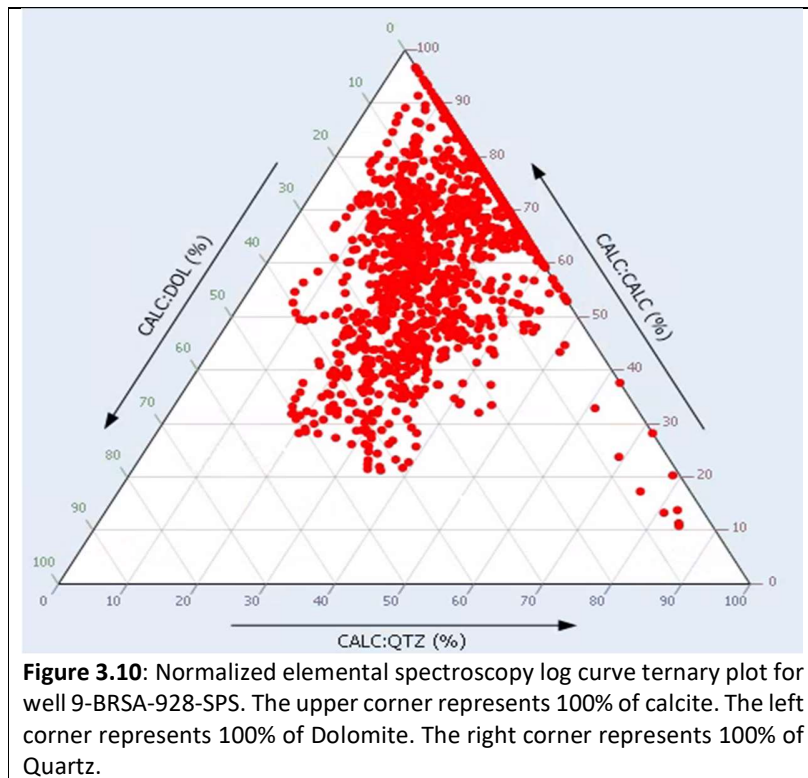


Figure 3.9: X-ray diffraction ternary plot for well 9-BRSA-928-SPS. The Upper corner represents 100% of calcite. The left corner represents 100% of Dolomite. The right corner represents 100% of Quartz.



- **9-BRSA-1037-SPS**

For the well 9-BRSA-1037-SPS charts (Figure 3.11 and 3.12), for the BVE100 zone, it can be observed that the mineral matrix has a composition between limestones and dolostones, as the previous well.

The histogram of RhoMatApp (figure 3.12) shows an average of 2,80g/cm³ of density, indicating an average value between the calcite and dolomite. The DTMatApp (Figure 3.13) histogram presents a mean value of 47,3 μSec/Ft, that signifies, once more, a mixture of dolomite and calcite.

The ternary plot of X-ray diffraction (Figure 3.14) analysis shows, again, a relevant variety of mineral composition, with a relevant dolomite and calcite content. The ternary plot of spectroscopy log (Figure 3.15) indicates a higher content of calcite and lower presence of quartz and dolomite when compared with X-ray diffraction data.

We can summarized once more that the different methods shows similar results, indicating a coherent analysis. The composition is majority of calcite and dolomite, with a minor contribution of quartz. The elemental spectroscopy log curves is considered as a mineral indicator curve.

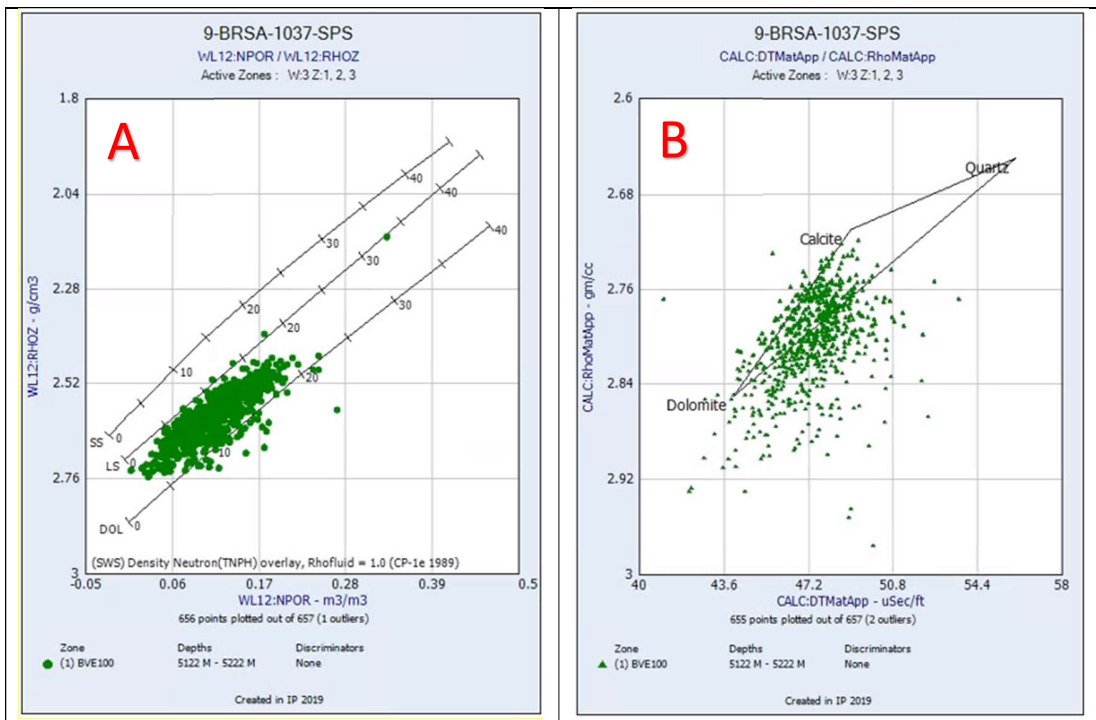


Figure 3.11: Charts NPOR X RHOZ and DTMatApp x RhoMatApp for well 9-BRSA-1037-SPS. **A:** Vertical axis is RHOZ and horizontal axis is NPOR. The overlay lines represent the mineral matrix lines. The green color points represent the well zone BVE100. **B:** Vertical axis is apparent matrix density (RhoMatApp). Horizontal axis is apparent matrix slowness (DTMatApp). The vertices of overlay triangle are the minerals calcite, quartz and dolomite. The green color points represent the well zone BVE100.

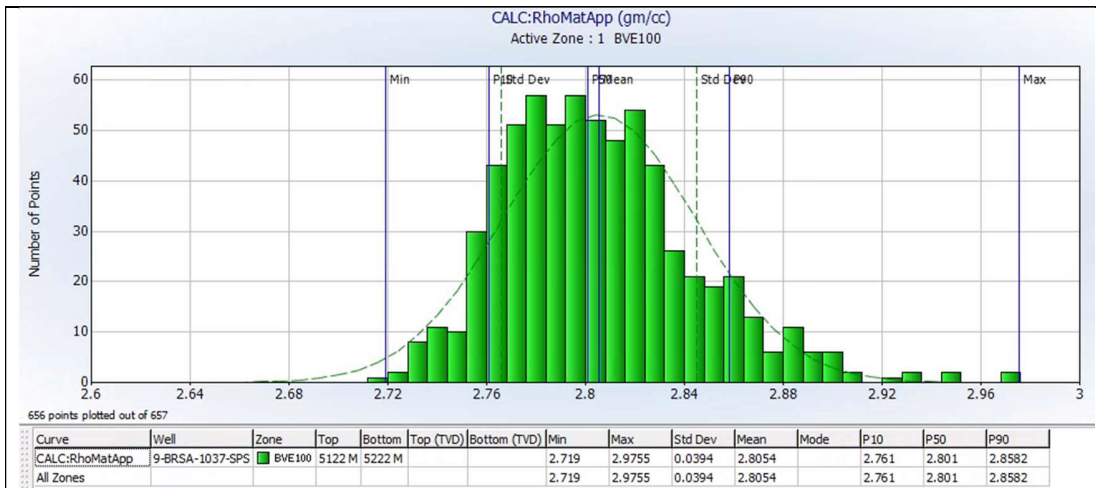


Figure 3.12: Matrix apparent density (RhoMatApp) histogram for well 9-BRSA-1037-SPS, zone BVE100. Vertical axis is the apparent density. Vertical axis is the number of points. The table below the histogram presents the statistics of the data.

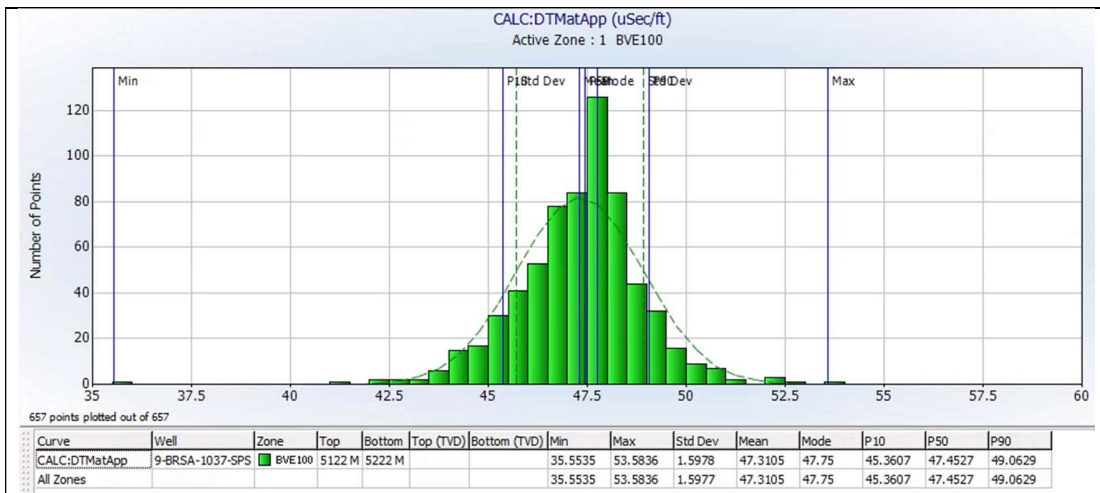


Figure 3.13: Matrix apparent slowness (DTMatApp) histogram for well 9-BRSA-1037-SPS, zone BVE100. Vertical axis is the apparent slowness. Vertical axis is the number of points. The table below the histogram presents the statistics of the data.

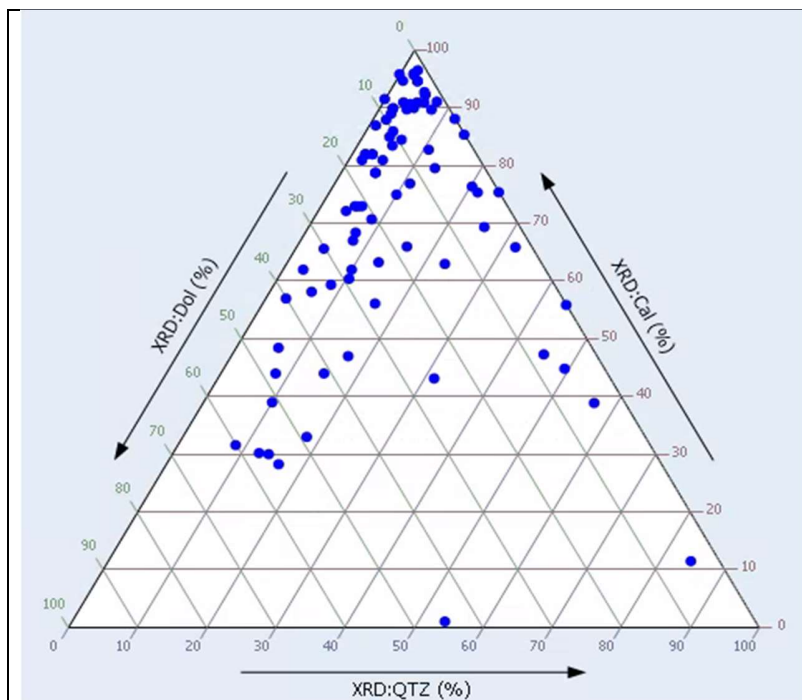
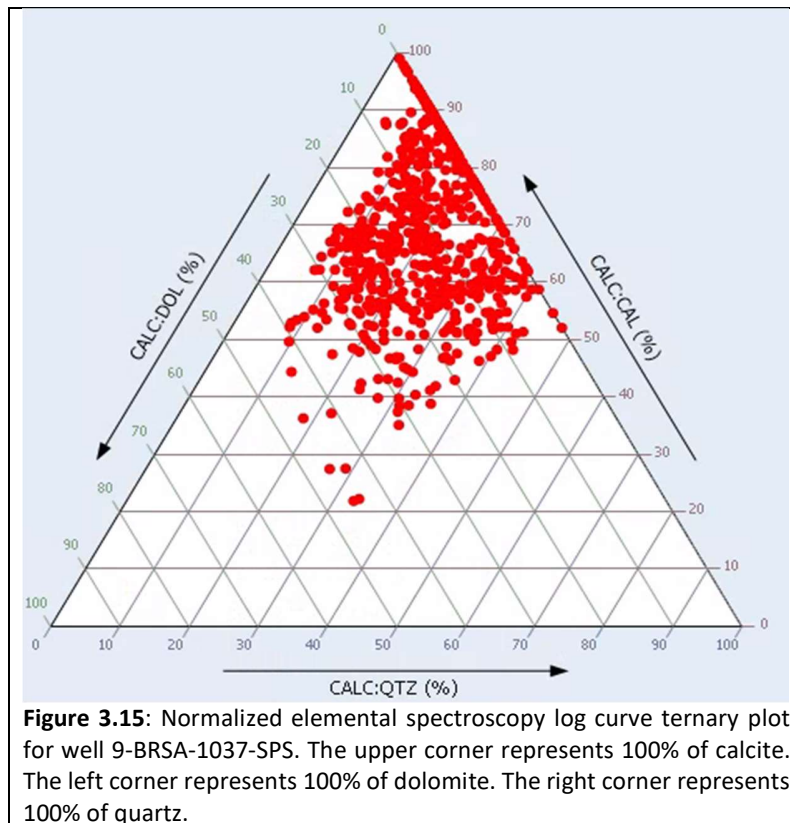


Figure 3.14: X-ray diffraction ternary plot for well 9-BRSA-1037-SPS. The Upper corner represents 100% of calcite. The left corner represents 100% of dolomite. The right corner represents 100% of quartz.



- **1-BRSA-594-SPS**

For the matrix analysis charts (figure 3.16) of the 1-BRSA-594-SPS once again it can be observed a mixture mineral composition. Particularly, from the histogram of RhoMatApp (Figure 3.17), it can be observed again a slight dislocation of the mineral density on the zones BVE300 (mean value of 2.83g/cm^3) to elevated values, indicating the possibility of the drilling mud invasion (with the influence of dense material as barite). In contrast, for the zone BVE100, the mean value is around $2,8\text{g/cm}^3$. The DTMatApp (Figure 3.18) in contrast, does not present the influence of the drilling mud invasion, showing a mean value of $47,0\ \mu\text{Sec/Ft}$.

For the 1-BRSA-594-SPS it was not possible to create the ternary plot was with elemental spectroscopy log, once the logging toll did not acquired the magnesium element curve. However, the X-ray diffraction samples were plotted (Figure 3.19) and once again, it can be observed mineral mixtures composition, including samples with a high content of quartz. Once more, the diverse techniques presents similar values, indicating consistent in the analysis. As the elemental spectroscopy log did not acquired the magnesium element, it was not used as mineralogy indication.

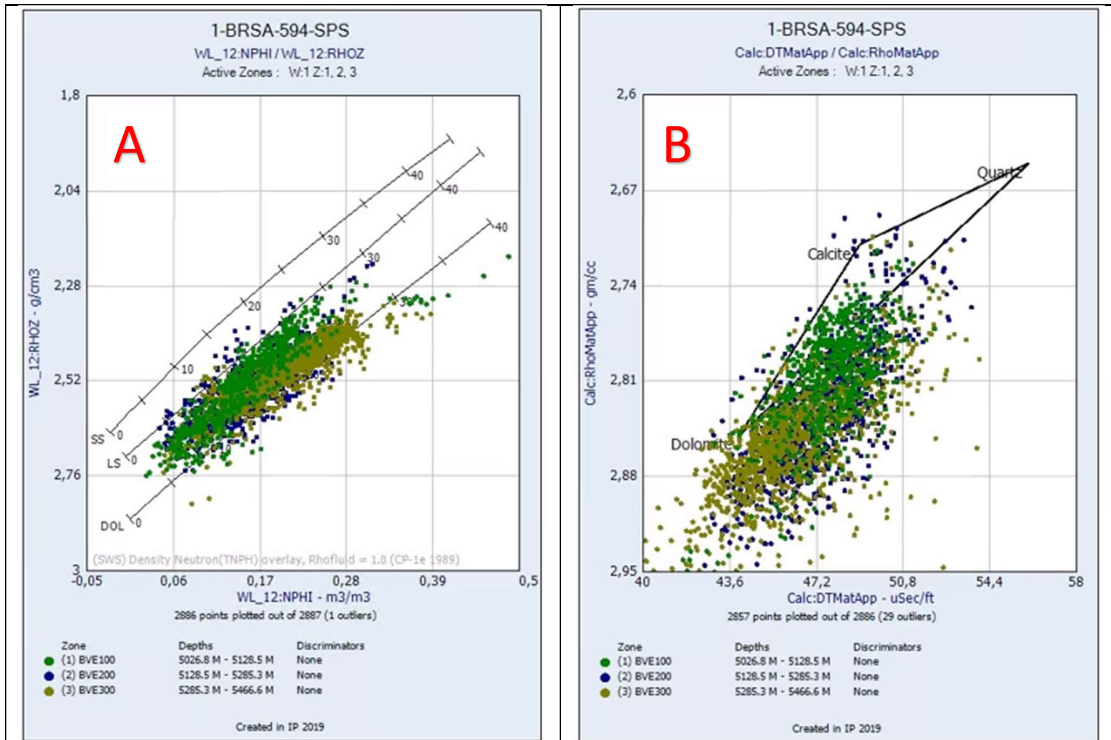


Figure 3.16: Charts NPHI X RHOZ and DTMatApp x RhoMatApp for well 9-BRSA-594-SPS. **A:** Vertical axis is RHOZ and horizontal axis is NPHI. The overlay lines represents the mineral matrix lines. The points different colors represent the different well zones BVE100, BVE200 and BVE300. **B:** Vertical line is apparent matrix density (RhoMatApp). Horizontal axis is apparent matrix slowness (DTMatApp). The vertices of overlay triangle are the minerals calcite, quartz and dolomite. The points different colors represent the different well zones BVE100, BVE200 and BVE300.

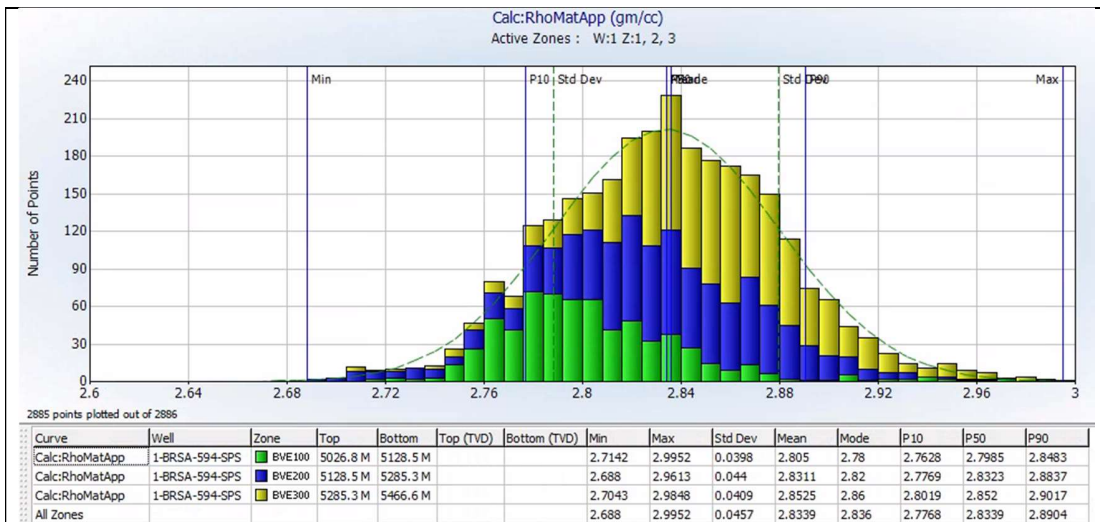


Figure 3.17: Matrix apparent density (RhoMatApp) histogram for well 1-BRSA-594-SPS. Vertical axis is the apparent density. Vertical axis is the number of points. The different colors refers to the well zones BVE100, BVE200 and BVE300. The table below the histogram presents the statistics of the data.

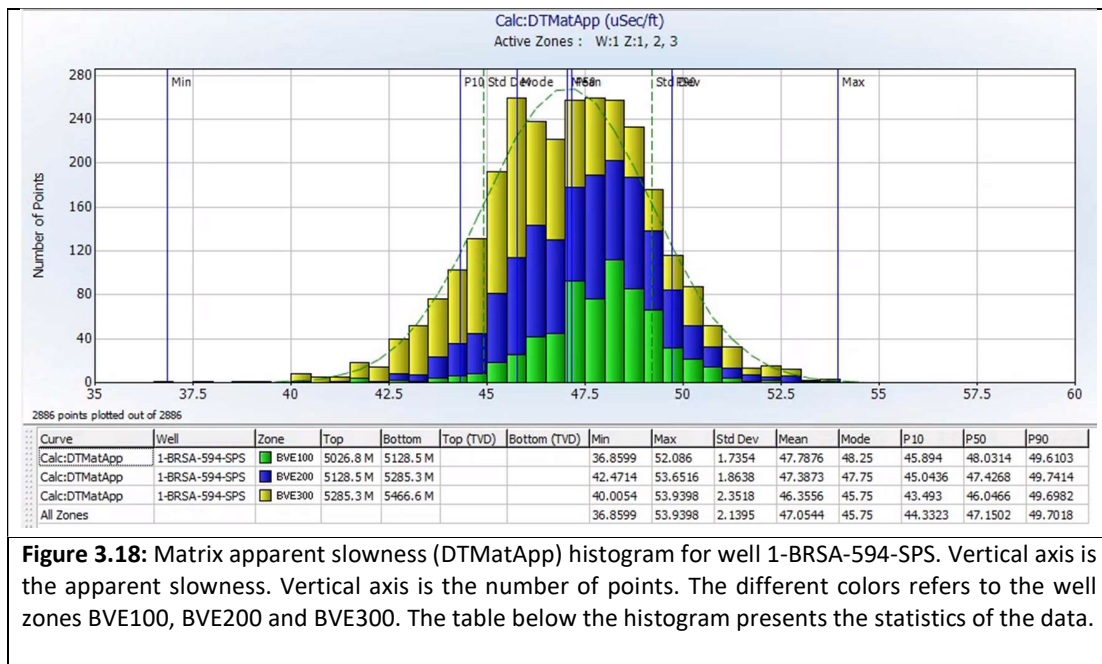
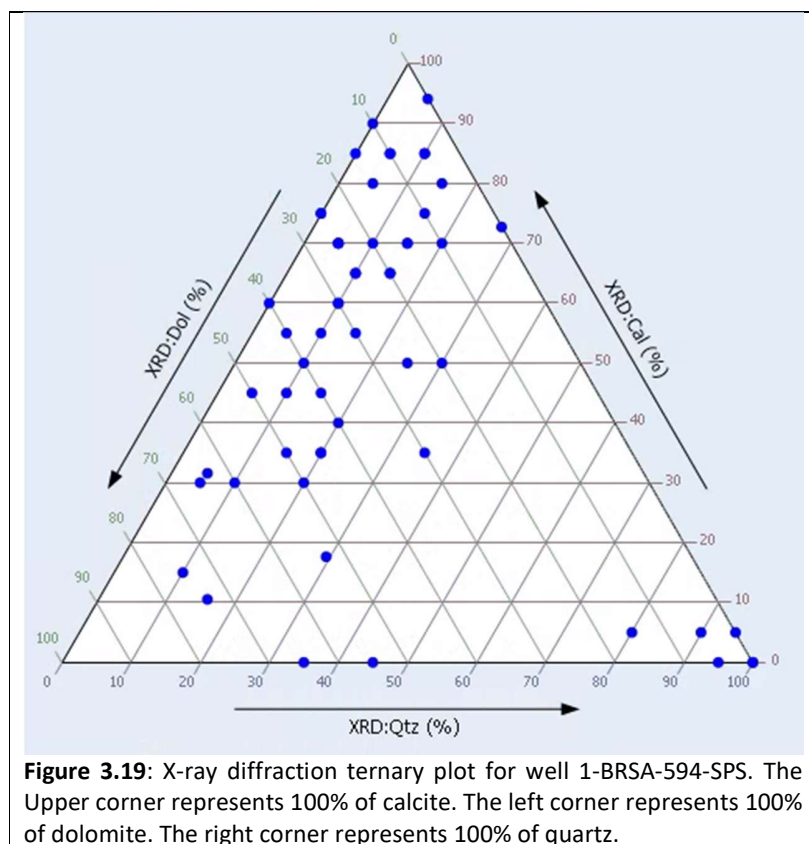


Figure 3.18: Matrix apparent slowness (DTMatApp) histogram for well 1-BRSA-594-SPS. Vertical axis is the apparent slowness. Vertical axis is the number of points. The different colors refers to the well zones BVE100, BVE200 and BVE300. The table below the histogram presents the statistics of the data.



3.1.2. Porosity Calculation

3.1.2.1. Methods

The porosity analysis was performed by comparisons of different porosity curves. From the density log, the porosity (ϕ_{den}) was calculate by the equation:

$$\phi_{den} = \frac{\rho_{mat} - \rho_b}{\rho_{ma} - \rho} \quad \text{Eq.16}$$

Where: ρ_{mat} is the matrix apparent density;
 ρ_b is the density value from the log;
 ρ_{fl} is the fluid density (for density logs we consider the drilling mud fluid);

Another curve that was calculate was the sonic porosity (ϕ_{son}) by manipulating the Wyllie equation (Eq.4):

$$\phi_{son} = \frac{DT - DT_m}{DT_{fl} - DT_m} \times C_p \quad \text{Eq.17}$$

Where: DT is the sonic log value;
 DT_m is the apparent Dt matrix;
 DT_{fl} is the fluid density (for sonic log we consider the drilling fluid slowness);
 C_p is the compaction factor (considered equal to unity);

In addition, the curve ϕ_{INDxp} , generated by the density-neutrons cross plot, and the effective porosity curve (ϕ_{nmr}), that is the result of the processing of the T2 decay from the NMR log using the cutoff of 3ms, were also compared.

3.1.2.2. Results

We can observe by the porosity curves histograms, summarized on table 3, that there is a significant variation on the porosities mean and mode, for the three wells. In addition, the standard deviation values shows an important variation. This can be

attributed to, as was observed on the previous section, there is an important variation on the mineral matrix composition, between Calcite, Dolomite and Quartz. Considering this, it can be assumed that the NMR effective porosity curve must be the most trustful since this porosity curve is matrix independent.

Well name	Phi_den (dec)	Phi_Son (dec)	PhiNDxp (dec)	nmrPhie (dec)
9-BRSA-928-SPS	0.13	0.09	0.13	0.12
9-BRSA-1037-SPS	0.09	0.06	0.1	0.08
1-BRSA-594-SPS	0.14	0.1	0.15	0.12

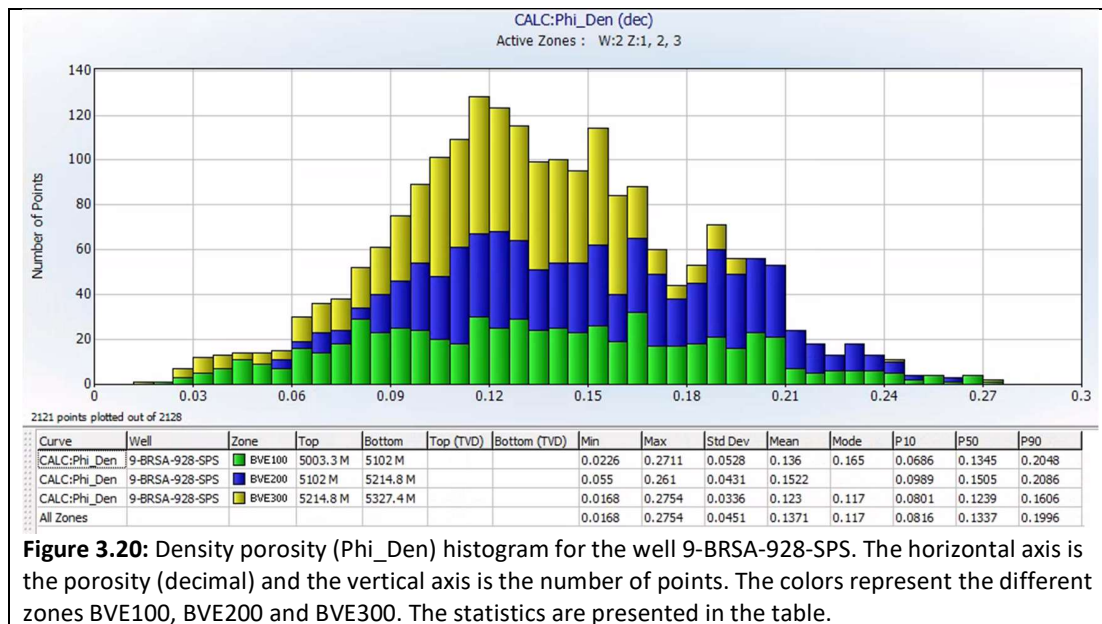
Table 3.1: Summary of mean values of porosity (dec) curves for the different three wells.

- **9-BRSA-928-SPS**

For the calculations of Phi_Den it was assumed the mean value of RhoMatApp histogram equal to 2,8g/cm³. For the Phi_Son it was used 47,9μs/ft, also acquired from the DTMatApp histogram and 220 μs/ft for the fluid slowness (*DTfl*).

Analyzing the histograms of different porosity histograms (Figure 3.20, 3.21, 3.22 and 3.23) for the well 9-BRSA-928-SPS, we can observe that the mean values of porosity varies from 8,3% to 13,8%.

It can be observed that the zone BVE200 presents higher porosity values than the other zones, by analyzing the nmrPhie histogram (Figure 3.23).



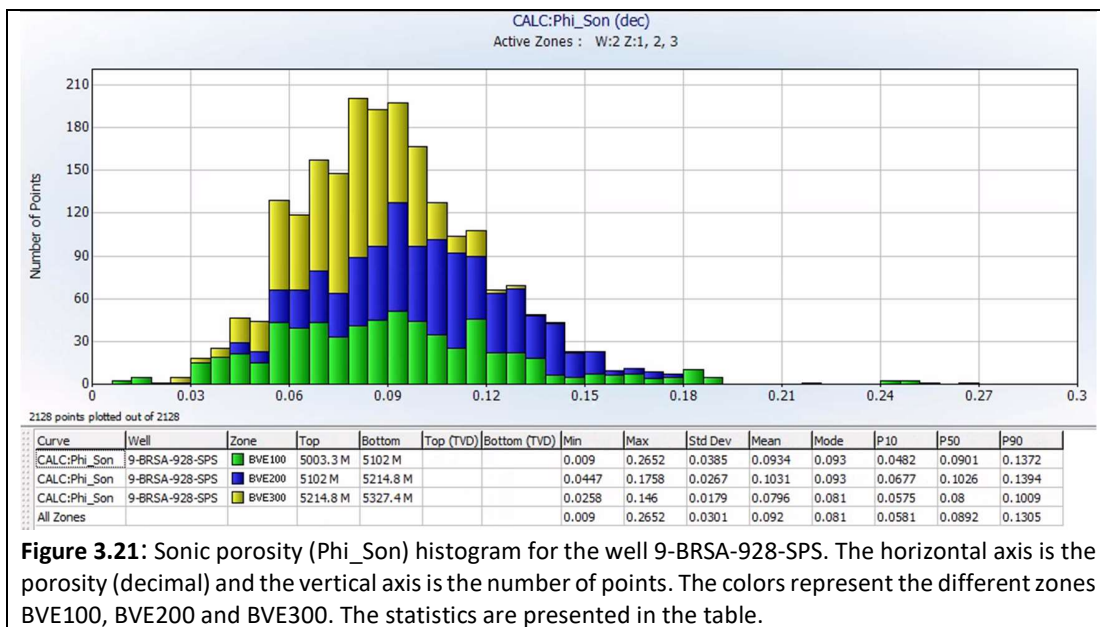


Figure 3.21: Sonic porosity (Phi_Son) histogram for the well 9-BRSA-928-SPS. The horizontal axis is the porosity (decimal) and the vertical axis is the number of points. The colors represent the different zones BVE100, BVE200 and BVE300. The statistics are presented in the table.

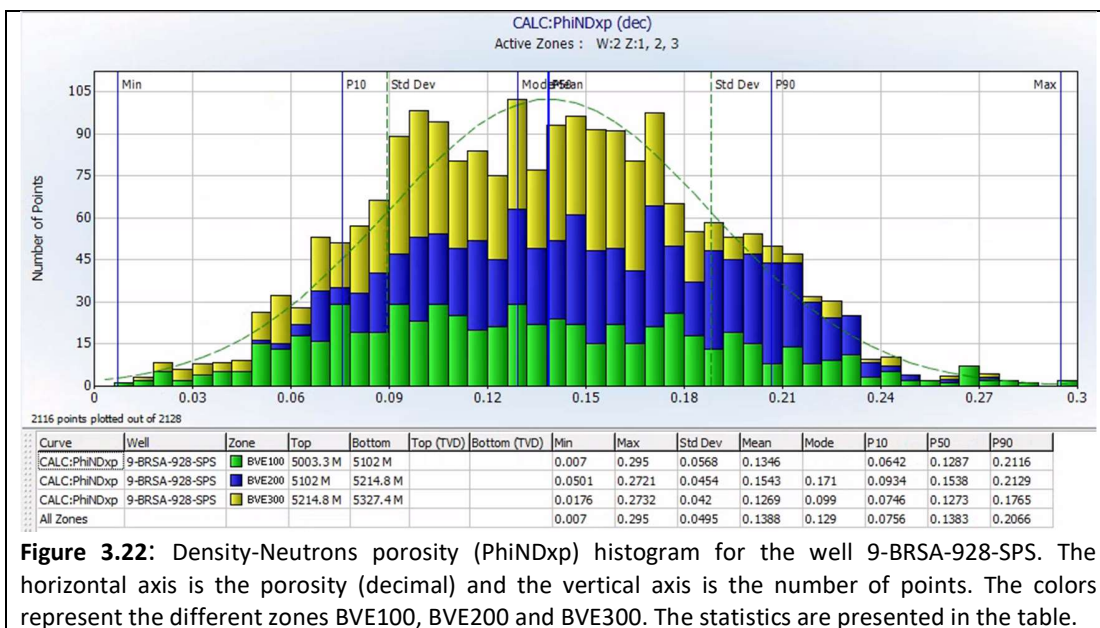
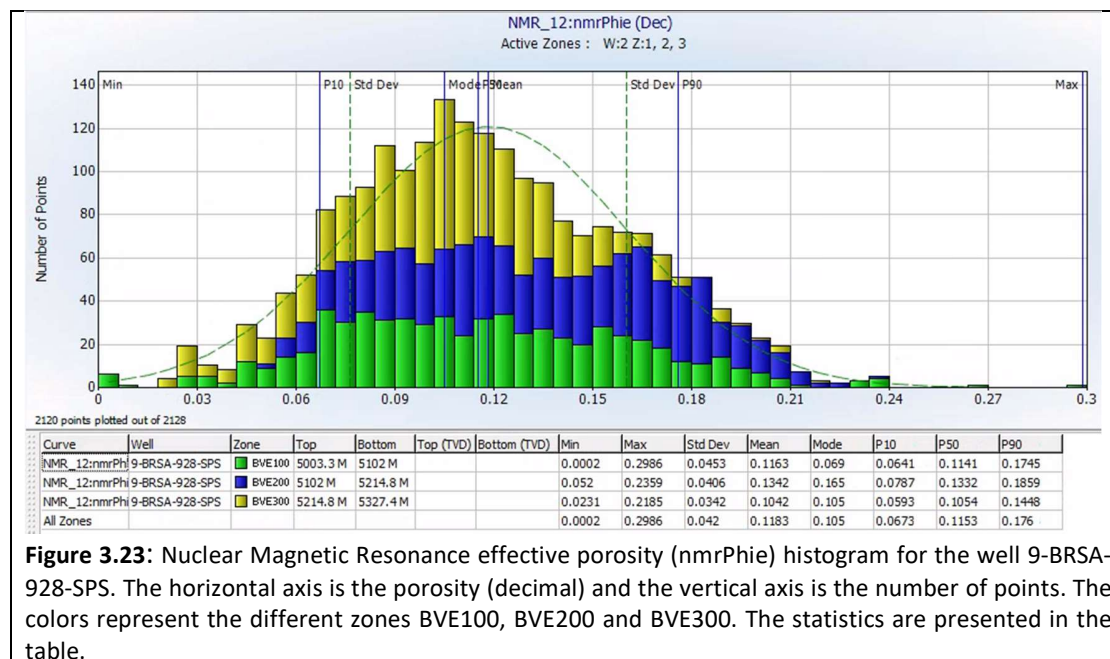


Figure 3.22: Density-Neutrons porosity (PhiNDxp) histogram for the well 9-BRSA-928-SPS. The horizontal axis is the porosity (decimal) and the vertical axis is the number of points. The colors represent the different zones BVE100, BVE200 and BVE300. The statistics are presented in the table.

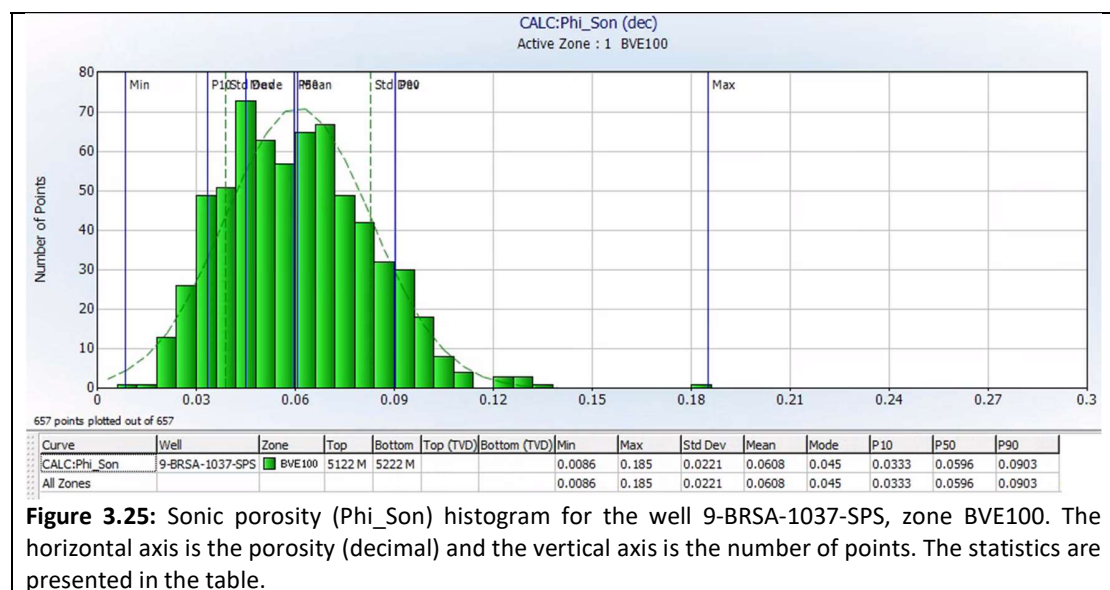
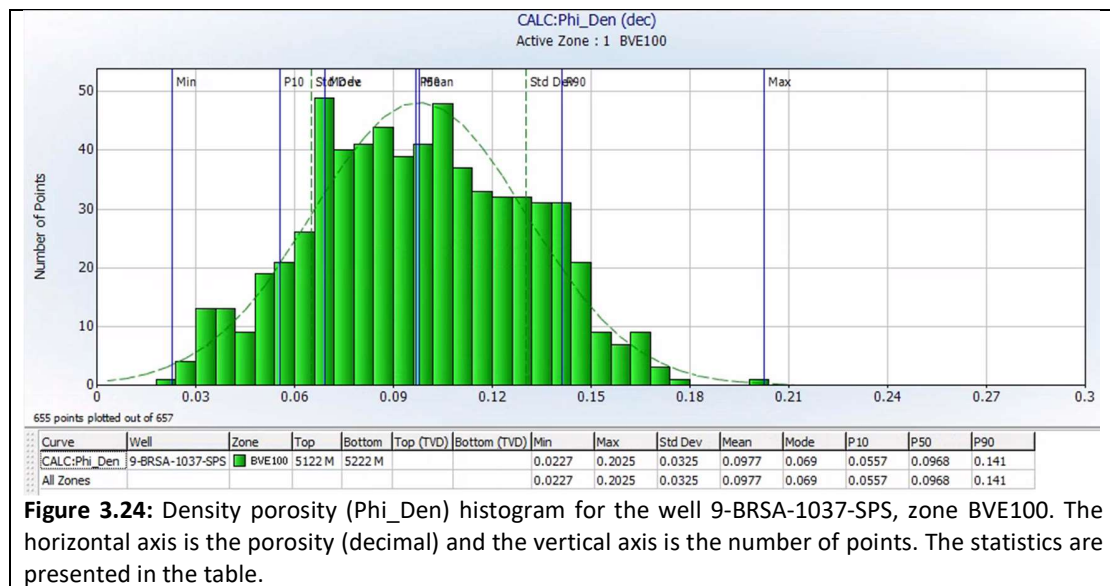


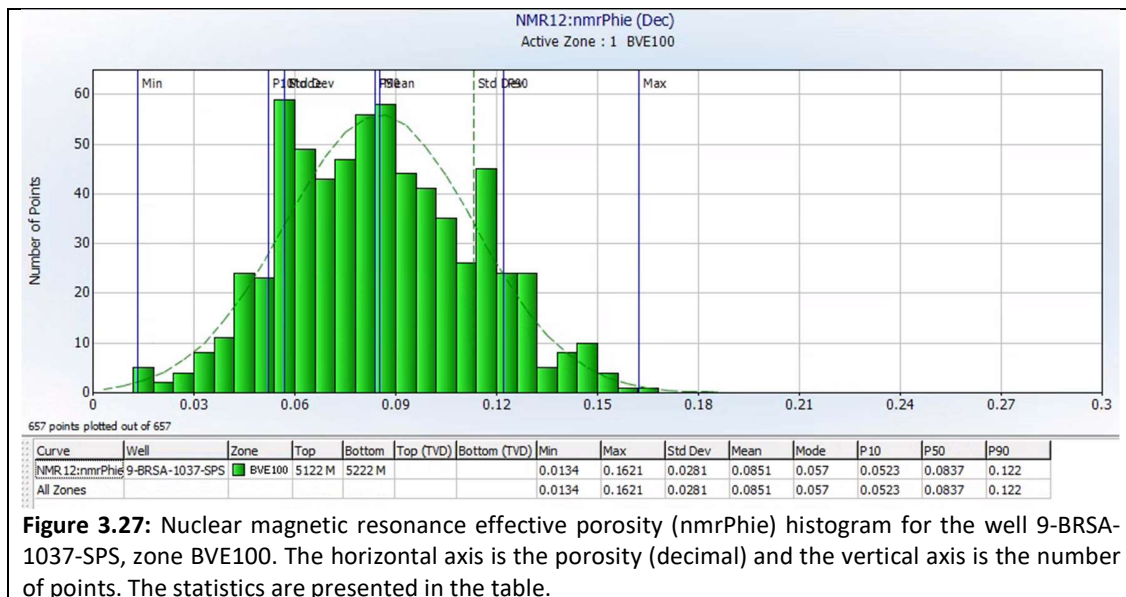
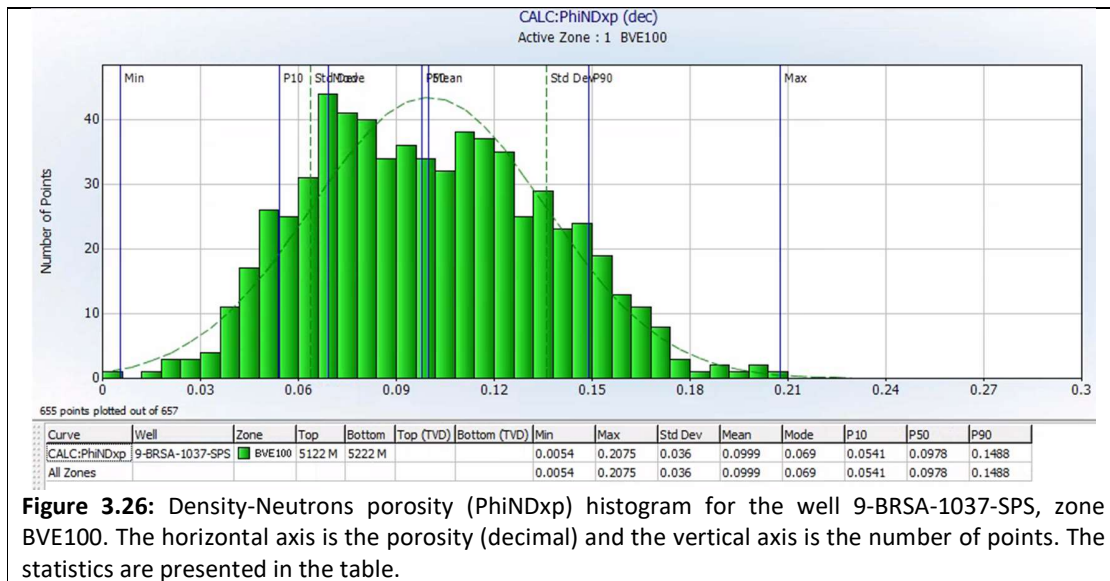
- **9-BRSA-1037-SPS**

For the calculations of Phi_Den it was assumed the mean value of RhoMatApp histogram equal to 2,8g/cm³. For the Phi_Son it was used 47,3 μs/ft, also acquired from the DTMatApp histogram and 220 μs/ft for the fluid slowness (*DTfl*).

By the analysis of the histograms of different porosity curves (Figure 3.24, 3.25, 3.26 and 3.27) for the well 9-BRSA-1037-SPS, we can notice that the mean values varies from 6,0% to 9,9%.

When comparing the nmrPhie values for the zone BVE100 with the others wells, it can be observed that the well 9-BRSA-1037-SPS, the values are considerably lower. It can be explained by the rocks being deposited in a lower energy environment, with presence of smaller particles, as well by the occurrence of more intense diagenetic process that obliterated the primary porosities.





- **1-BRSA-594-SPS**

For the calculations of Φ_{Den} it was assumed the mean value of ρ_{MatApp} histogram equal to $2,83\text{g/cm}^3$. For the Φ_{Son} it was used $47,0\text{ }\mu\text{s/ft}$, also acquired from the DT_{MatApp} histogram and $220\text{ }\mu\text{s/ft}$ for the fluid slowness (DT_f).

The histograms of different porosity curves (Figure 3.28, 3.29, 3.30 and 3.31) for the well 1-BRSA-594-SPS shows mean values varies from 9,8% to 15,4%.

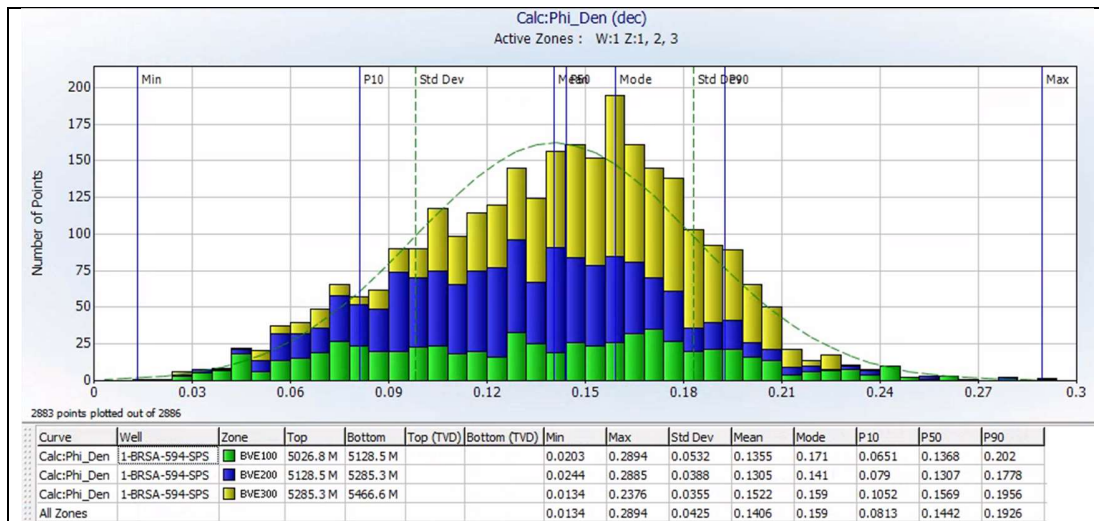


Figure 3.28: Density porosity (Phi_Den) histogram for the well 1-BRSA-594-SPS. The horizontal axis is the porosity (decimal) and the vertical axis is the number of points. The colors represent the different zones BVE100, BVE200 and BVE300. The statistics are presented in the table.

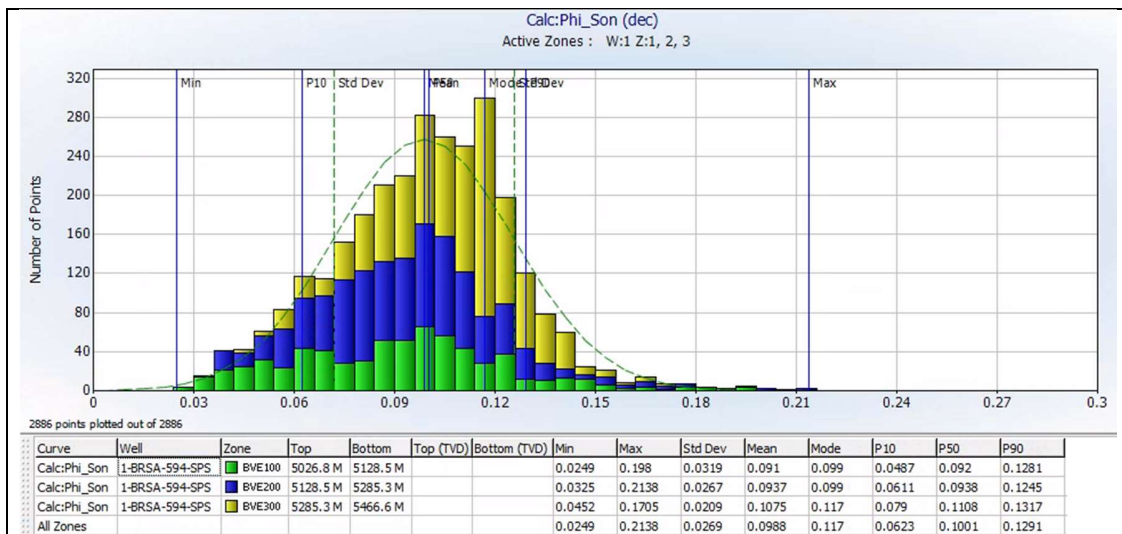


Figure 3.29: Sonic porosity (Phi_Son) histogram for the well 1-BRSA-594-SPS. The horizontal axis is the porosity (decimal) and the vertical axis is the number of points. The colors represent the different zones BVE100, BVE200 and BVE300. The statistics are presented in the table.

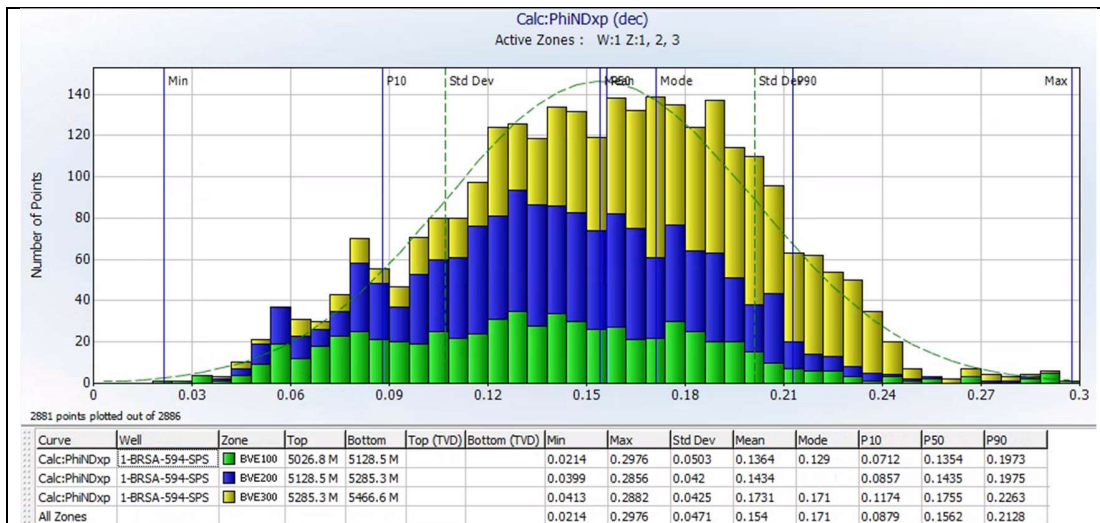


Figure 3.30: Density-Neutrons porosity (PhiNDxp) histogram for the well 1-BRSA-594-SPS. The horizontal axis is the porosity (decimal) and the vertical axis is the number of points. The colors represent the different zones BVE100, BVE200 and BVE300. The statistics are presented in the table.

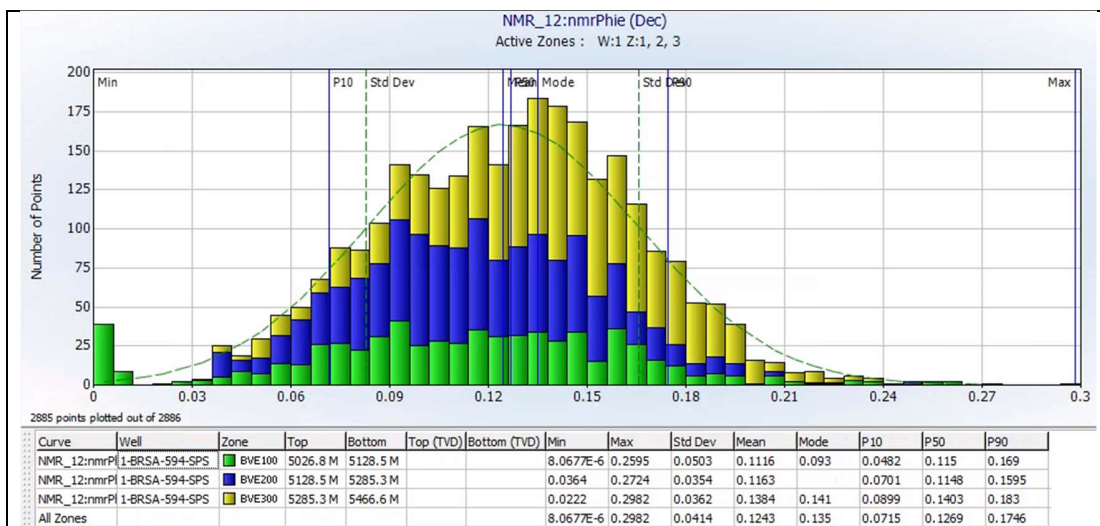


Figure 3.31: Nuclear Magnetic Resonance effective porosity (nmrPhie) histogram for the well 1-BRSA-594-SPS. The horizontal axis is the porosity (decimal) and the vertical axis is the number of points. The colors represent the different zones BVE100, BVE200 and BVE300. The statistics are presented in the table.

3.1.3. Porosity Types Identification

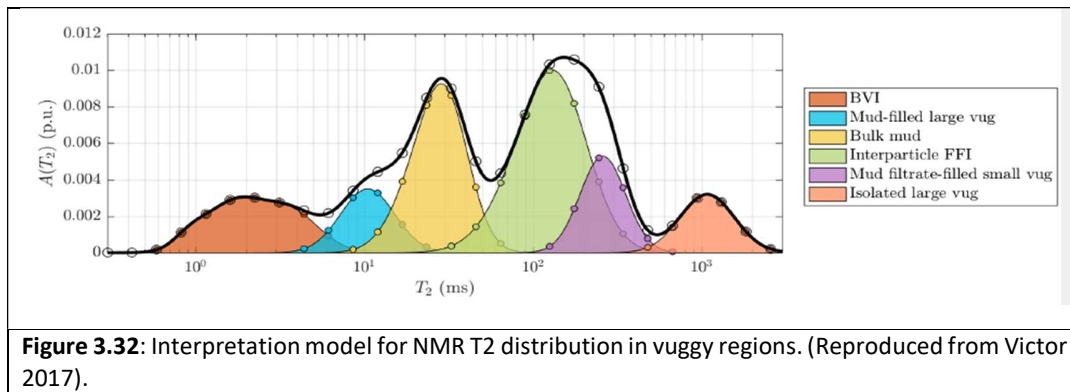
3.1.3.1. Methods

As it was already discussed on the previous chapter, carbonate rocks have a great variety of porosity types that are the result of the sedimentation environment and the diagenesis processes. Many authors have discussed techniques to identify the porosity types on carbonate reservoirs. One of the most common methods is to compare the sonic porosity with other porosity curves, in which the differences are related to the presence of secondary porosity (vugs and fractures). The acoustic wave energy finds a faster path around these inclusions (Ellis & Singer 2007), noticing only the primary porosity.

Anselmetti and Eberli (1999) revealed that the acoustic velocity in carbonate rocks is a function of porosity and porosity types. These authors developed a technique where the velocity measured by the sonic log is compared with a calculated velocity (using a different porosity log) and the differences were interpreted as the result of the presence of diverse porosity types. The authors defined the term “velocity deviation” as this measured difference. The zones with positive deviations (more than +500m/s) were interpreted as intrafossil or moldic porosity. The deviations close to zero (between -500m/s and +500m/s) the dominant porosity types are interparticle, intercrystalline or microporosity. Moreover, negative deviations (less than -500m/s) interpreted as possible fractures (Anselmetti and Eberli 1999).

Victor (Victor 2017), in his dissertation, integrated a variety of analysis from well logs to computed tomography images, and suggested an improved interpretation technique for NMR T₂ logs. The author demonstrated that carbonate vuggy regions are associated with little mudcake, high PEFZ responses and low NMR T₂ logarithmic mean. Therefore a T₂ distribution could be decomposed into a finite set of log-normal components (Victor 2017), where different effects on T₂ could be interpreted as different components. From this, seven T₂ cutoffs were defined (Figure 3.32): 0 ms to 3ms, for clay bound water; 3ms to 10ms as capillary bound water; 10ms to 60ms as drilling fluid filled large vugs or bulk drilling fluid; 60ms to 100ms as capillary bound water; 100ms to 590ms as interparticle free fluid; 590 to 1000ms as small connected vugs; and higher than 1000ms as isolated vugs.

In addition, another practical way to identify the porosity types from carbonate rocks, is to plot porosity versus permeability values, derived from routine core analysis, in a cross plot and observe where the points are located at the Lucia Classes (Lucia 1983).



3.1.3.2. Results

The well 9-BRSA-928-SPS shows an intense presence of secondary porosity along the well, according to the difference in the sonic and NMR effective porosity log (Figure 3.33). Taken into account the deviation log, the top interval of the zone BVE200 presents an important deviation, indicating the presence of vuggy porosity. In addition, the NMR pore type curves, demonstrates that different types of pores are mixed. The porosity seems to be a summation of interparticle, isolated vugs and connected vugs porosities. The chart porosity-permeability (figure 3.36) with Lucia Classes, derived from core analysis, presents intense points densities in the class1 and 2 regions, with an effect of touching vugs, increasing permeability and separate vugs, decreasing permeability.

The well 1-BRSA-594-SPS also presents an important presence of secondary porosity according to the secondary porosity log curve (Figure 3.34). In addition, the deviation log curve shows intervals with the occurrence of vuggy porosity. Particularly, the NMR pore type curve demonstrate again a presence of mixture porosity types (interparticle, isolated vugs and connected vugs). The top interval of the zone BVE100 especially exhibit an intense presence of isolated vuggy porosity, as can be seen in the highlighted are in figure 3.34. The chart porosity-permeability with Lucia Classes (Figure 3.37) for the core analysis shows a predominant of points in class 1, with strong influence of touching vugs .

Also the well 9-BRSA-1037-SPS (figure 3.35) exhibits similar interpretations when the secondary porosity, deviation log and NMR pore types curves are analyzed. However, the NMR pore types curves shows a lower proportion of vuggy porosity. Compared with the other wells, the cross plot porosity-permeability (Figure 3.38), presents a higher number of points in Lucia class 2 and 3.

The identification of the porosity types with different techniques is going to be integrated with the pore geometry analysis (Section 3.3), to develop petroelastic classes.

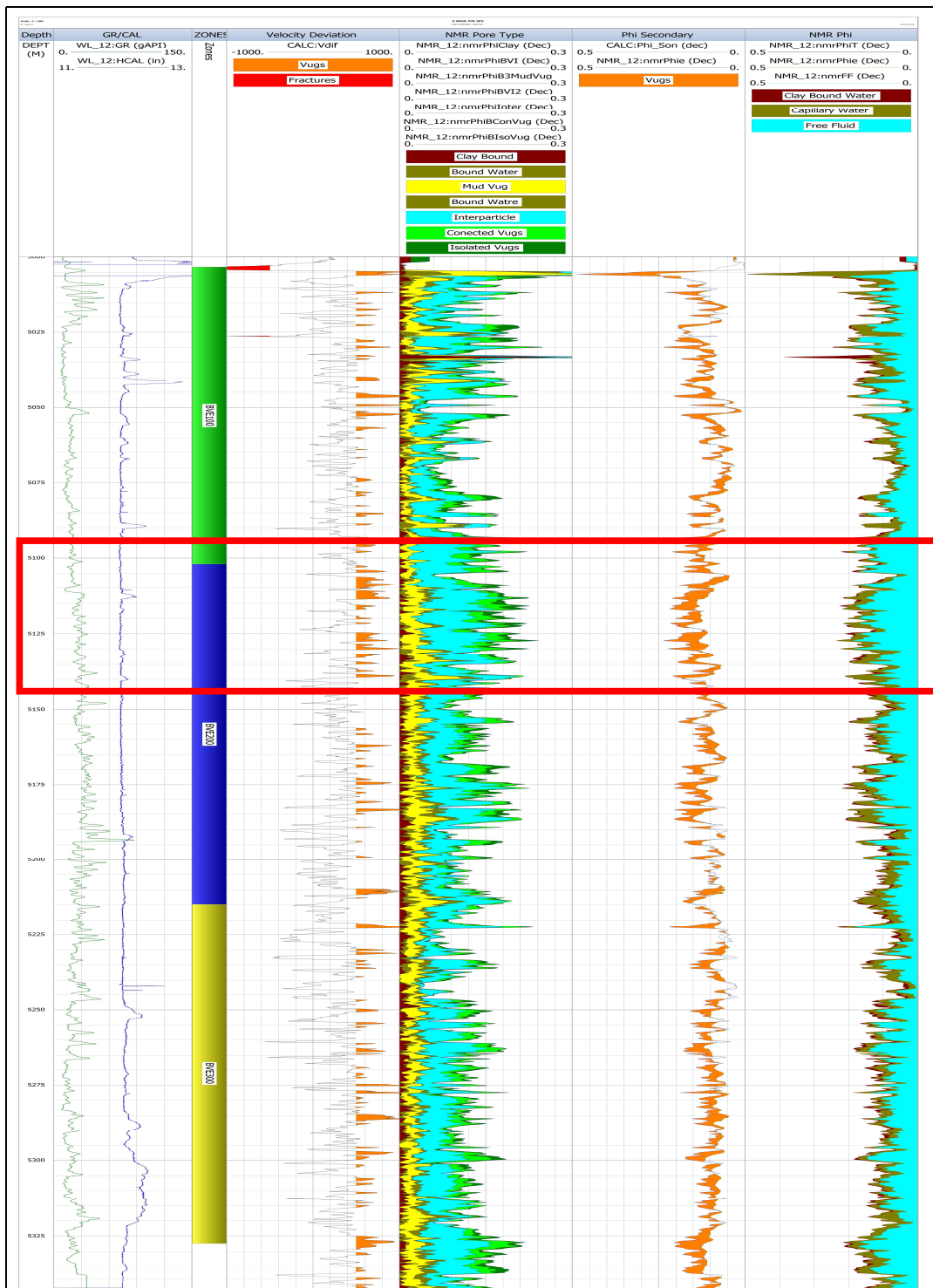


Figure 3.33: Porosity types logs composite for well 9-BRSA-928-SPS. Track 1: well depth. Track 2: Gamma-Ray (GR) and caliper (HCAL). Track 3: Zonation of well, zone BVE100 in green, BVE200 in blue and BVE300 in yellow. Track 4: Velocity deviation curve. Track 5: Nuclear Magnetic Resonance porosity type curves. Track 6: Secondary porosity curve. Track 7: Nuclear Magnetic Resonance porosity curves, Total porosity (nmrPHIT), Effective porosity (nmrPHIE) and Free Fluid (nmrFF). Red rectangle highlights vuggy interval.

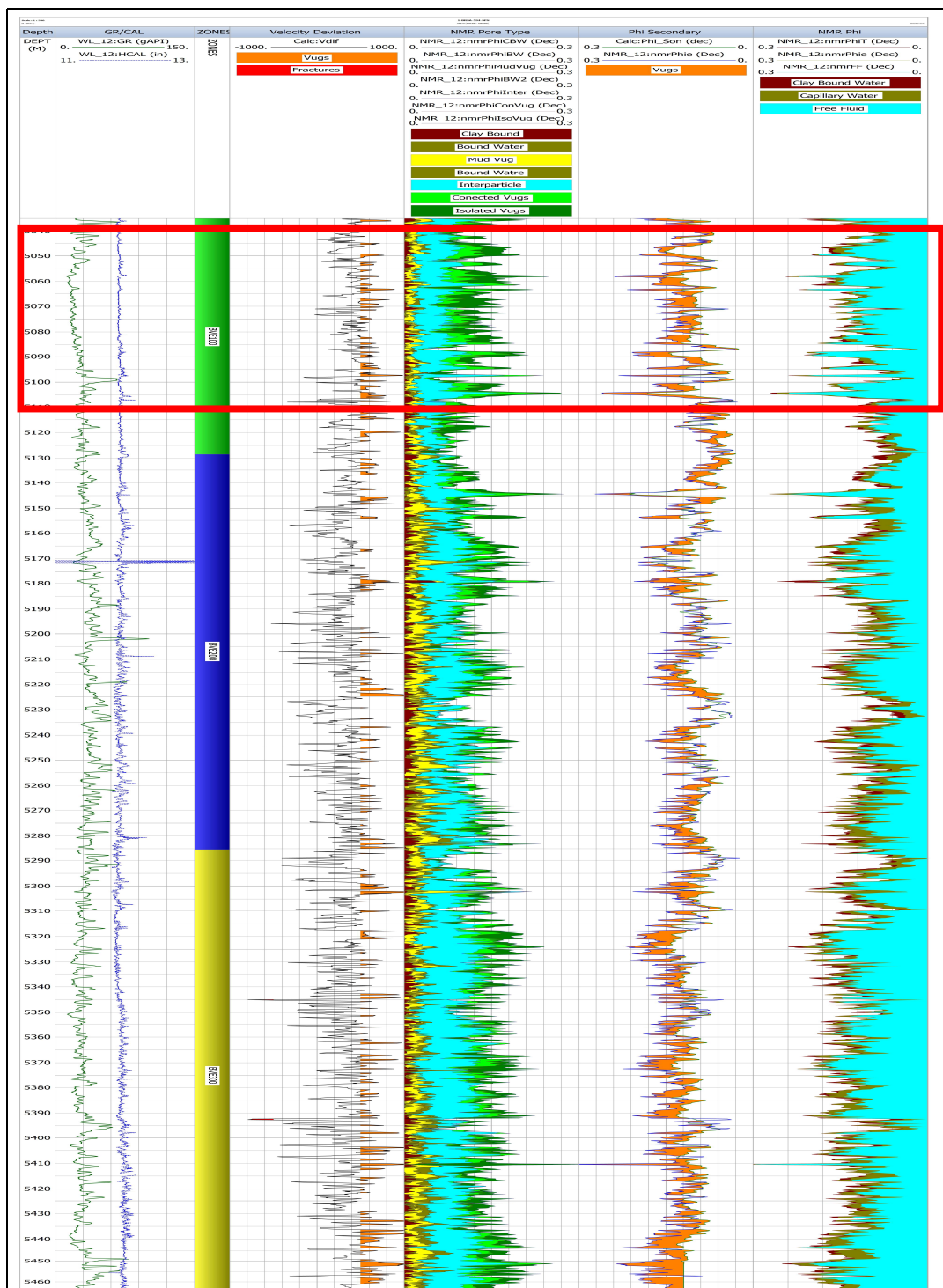


Figure 3.34: Porosity types logs composite for well 1-BRSA-594-SPS. Track 1: well depth. Track 2: Gamma-Ray (GR) and caliper (HCAL). Track 3: Zonation of well, zone BVE100 in green, BVE200 in blue and BVE300 in yellow. Track 4: Velocity deviation curve. Track 5: Nuclear Magnetic Resonance porosity type curves. Track 6: Secondary porosity curve. Track 7: Nuclear Magnetic Resonance porosity curves, Total porosity (nmrPHIT), Effective porosity (nmrPHIE) and Free Fluid (nmrFF). Red rectangle highlights vuggy interval.

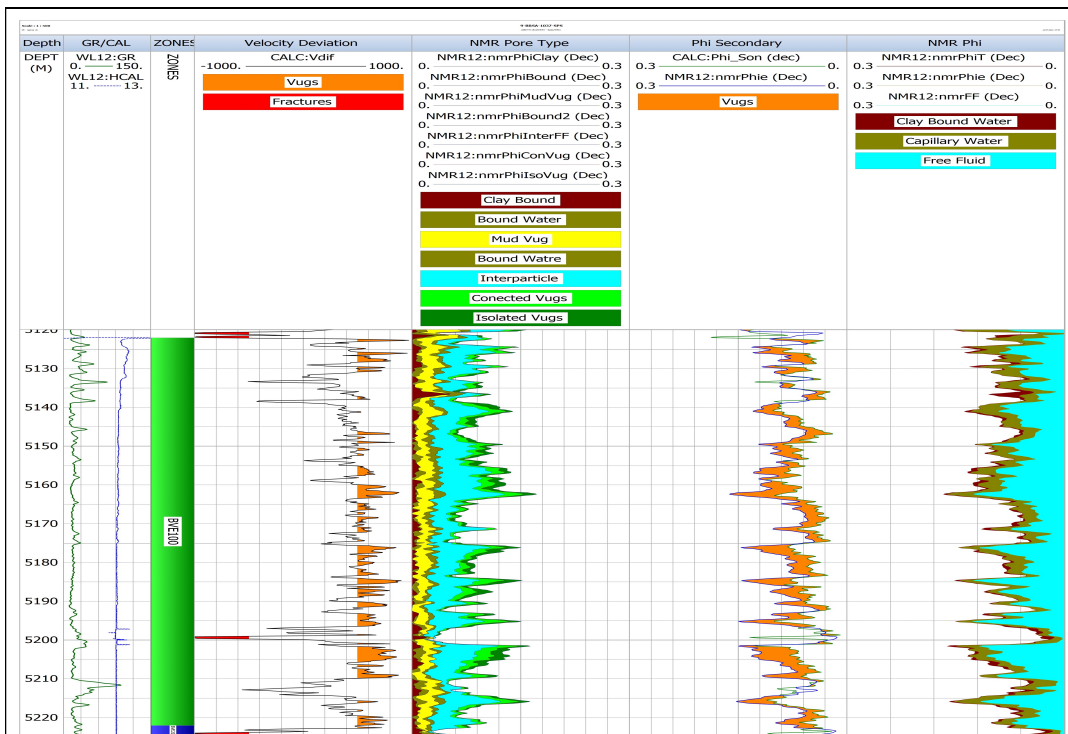


Figure 3.35: Porosity types logs composite for well 9-BRSA-1037-SPS. Track 1: well depth. Track 2: Gamma-Ray (GR) and caliper (HCAL). Track 3: Zonation of well, zone BVE100 in green. Track 4: Velocity deviation curve. Track 5: Nuclear Magnetic Resonance porosity type curves. Track 6: Secondary porosity curve. Track 7: Nuclear Magnetic Resonance porosity curves, Total porosity (nmrPHIT), Effective porosity (nmrPHIE) and Free Fluid (nmrFF).

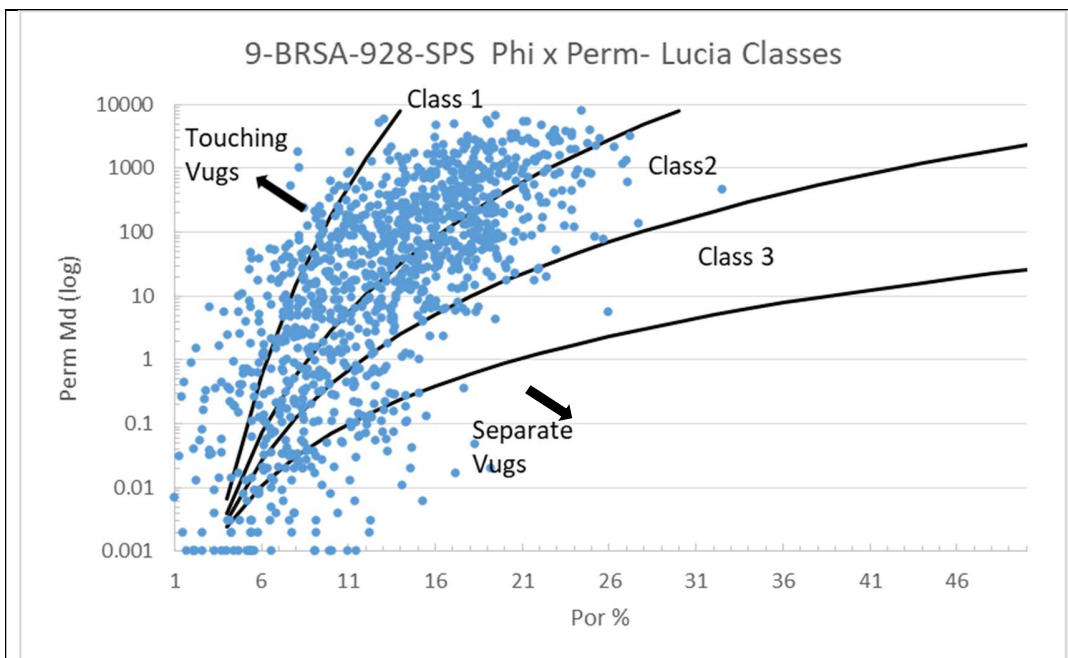


Figure 3.36: Porosity-Permeability cross plot for laboratory analysis for well 9-BRSA-928-SPS. The black lines divide the Lucia classes. The arrows indicate the effect of touching and isolate vugs.

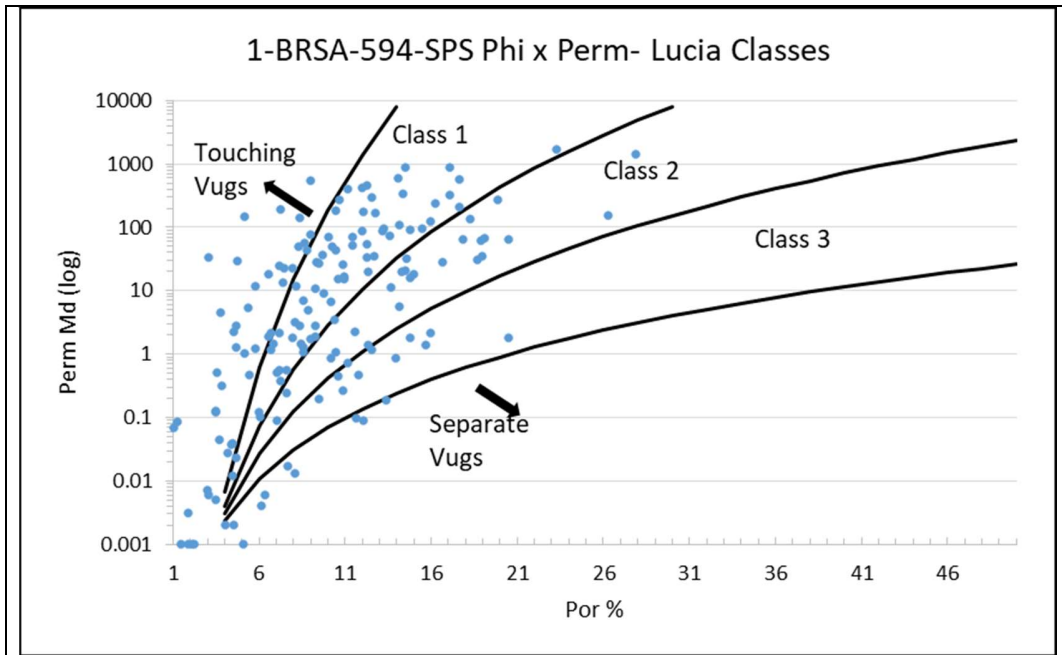


Figure 3.37: Porosity-Permeability cross plot for laboratory analysis for well 1-BRSA-1037-SPS. The black lines divide the Lucia classes. The arrows indicate the effect of touching and isolate vugs.

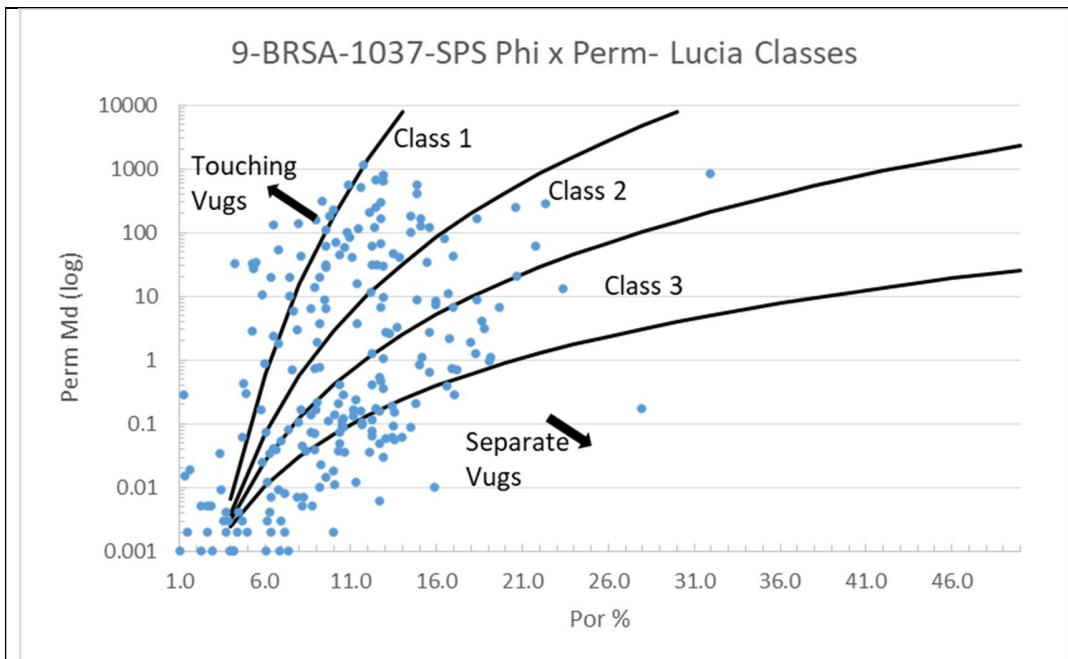


Figure 3.38: Porosity-Permeability cross plot for laboratory analysis for well 9-BRSA-1037-SPS. The black lines divide the Lucia classes. The arrows indicate the effect of touching and isolate vugs.

3.2. Petroelastic Model

To create the petroelastic model we assumed the pore space stiffness method; develop by Mavko & Mukerij (1995) and implemented by Babasafari (2020), to identify the pore space geometry and relate it with the porosity types.

To calculate the elastic moduli, our two different sets of data followed different methods. The calculations using core samples used the X-Ray diffractions, porosity, density and velocity measurements derived by laboratory analysis. For the well logs, the density, sonic and elemental spectroscopy logs were used.

The pore space stiffness assessment was performed by the use the Zimmerman (1984 & 1991) K_{phi} models. The different K_{phi} generated were compared with the pore space stiffness calculated, with the intention to identify the pore space geometries present in the wells.

Finally, to improve the interpretation of the petroelastic model and its relation with the porosity types, a pore geometry analysis was implemented, by the choosing of a specific geometry and analyzing the main pore geometries present in the wells.

3.2.1. Elastic moduli model

3.2.1.1. Methods

To develop the petroelastic model, one of the information necessary to proceed with the calculations is to obtain the effective mineral matrix bulk modulus. As was demonstrated in the previous section 3.1.1, the reservoir is composed mainly by three minerals, Calcite, Dolomite and Quartz, therefore, it was assumed for the model that only these three minerals are present.

To obtain the effective mineral bulk modulus K_m it was applied the Voigt (1910) and Reuss (1929) averaging techniques for a composed material, and obtain K_{mv} (mineral matrix bulk modulus Voigt average) and K_{mr} (mineral matrix bulk modulus Reuss average):

$$K_{mv} = \sum_{i=1}^n K_{mi} V_i \quad \text{Eq.18}$$

$$K_{mr} = \left[\sum_{i=1}^n \frac{V_i}{K_{mi}} \right]^{-1} \quad \text{Eq.19}$$

Where K_{mi} is the mineral bulk modulus and V_i is the mineral fraction. It was assumed that for Calcite the mineral matrix bulk modulus is 73 Gpa, for Dolomite is 94Gpa and for Quartz 38.2Gpa (Gebrande 1982).

To obtain the final value of K_m , a simple average between K_{mv} and K_{mr} was calculated (Hill 1952).

- **Well Logs**

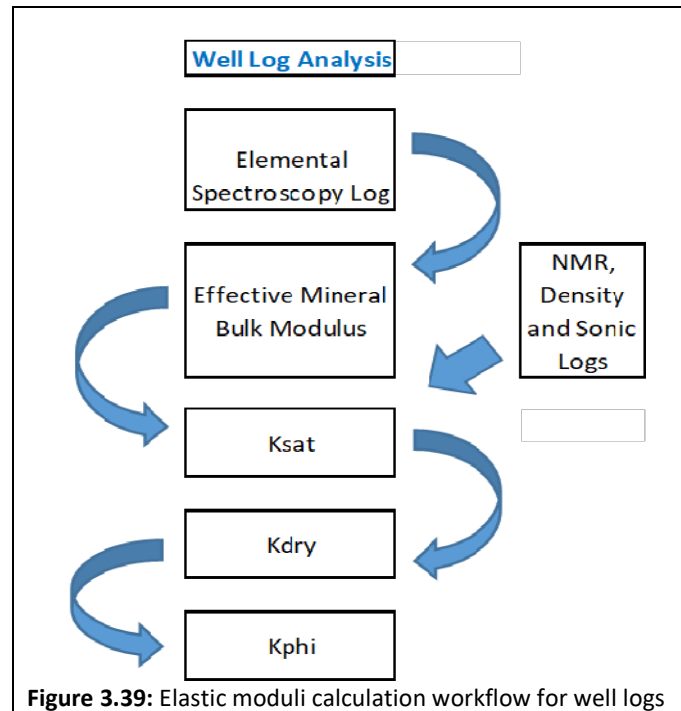
Regarding the log analysis (workflow can be seen on figure 3.39), it was assumed that the normalized mineral curves, generated by the elemental spectroscopy log, represents the mineral volume fraction values.

For the well 1-BRSA-594-SPS, as there was not acquired the Mg elemental curve in the logging operation, a separated approach was implemented. To obtain the K_m , it was develop a multilinear regression using the wells 9-BRSA-928-SPS and 9-BRSA-1037-SPS. As inputs it was used the GR, RhomatApp, DtMatApp, DWCA and DWSI curves, and the obtained K_m as curve to predict. The correlation coefficient was 0.98, showing a strong and consistent result. After that, the model was applied with the 1-BRSA-594-SPS curves and a K_m curve was obtained.

After that, it was necessary to transform the compressional and shear sonic log curves to compressional and shear velocities. The effective shear modulus μ_{sat} was calculated by equation 8 and the effective saturated bulk modulus K_{sat} , applying equation 9. It was assumed:

- the density log RHOZ as the effective density;
- the fluid effective bulk modulus K_{fl} as the synthetic fluid filtrate equal to 1,6Gpa,
- the porosity as the total porosity from the NMR log (nmrPhiT).

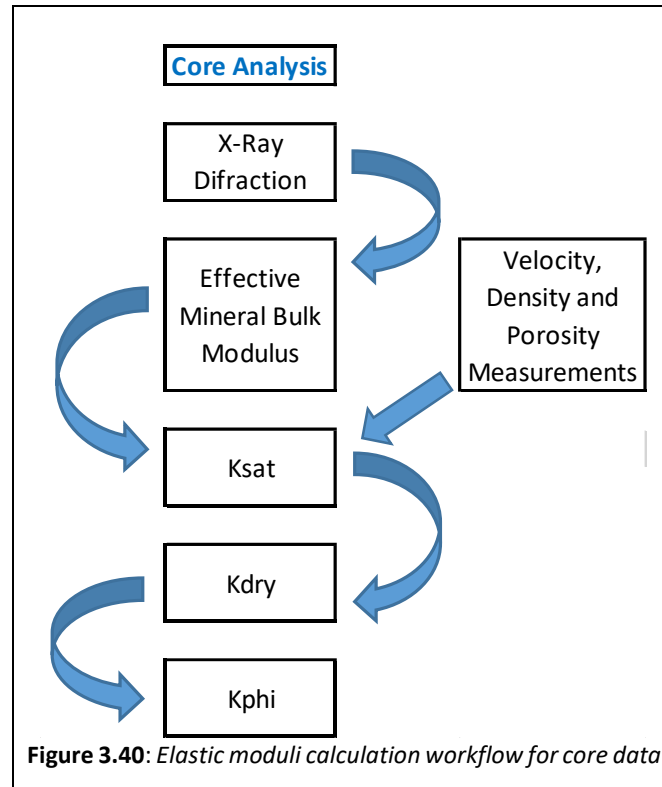
From that, it was retrieved the values of K_{dry} and K_{phi} , by equations 10 and 11.



- **Core Analysis**

In relation to the laboratory core samples (workflow description on figure 3.40), the x-ray diffraction (XRD) analysis was considered as the mineral fraction of the rock. The well 1-BRSA-594-SPS does not have XRD analysis and seismic measurements in the same samples, so this analysis was not performed.

Using the compressional velocity, density and porosity measurements obtained from the core analysis, it is possible to retrieve the effective saturated bulk modulus K_{sat} from equation 5. It can be assumed that, as the core analysis is implemented on dry rocks (air saturated pores), K_{sat} is equal to the dry rock bulk modulus K_{dry} . In possess of the K_{dry} , it can be calculated the pore space stiffness K_{phi} , by equation 11.



3.2.1.2. Results

Total porosity versus K_{phi} cross plots were generated using the log analysis for the three wells (Figures 3.41, 3.42 and 3.43). It can be observed that the K_{phi} values do not have a variation with porosity, which prove that the pore space stiffness is not a porosity function. However, K_{phi} presents a variation of values between 2Gpa and 30Gpa, indicating a relevant variation of pore space geometry. Next section will investigate and correlate the reasons behind these variations.

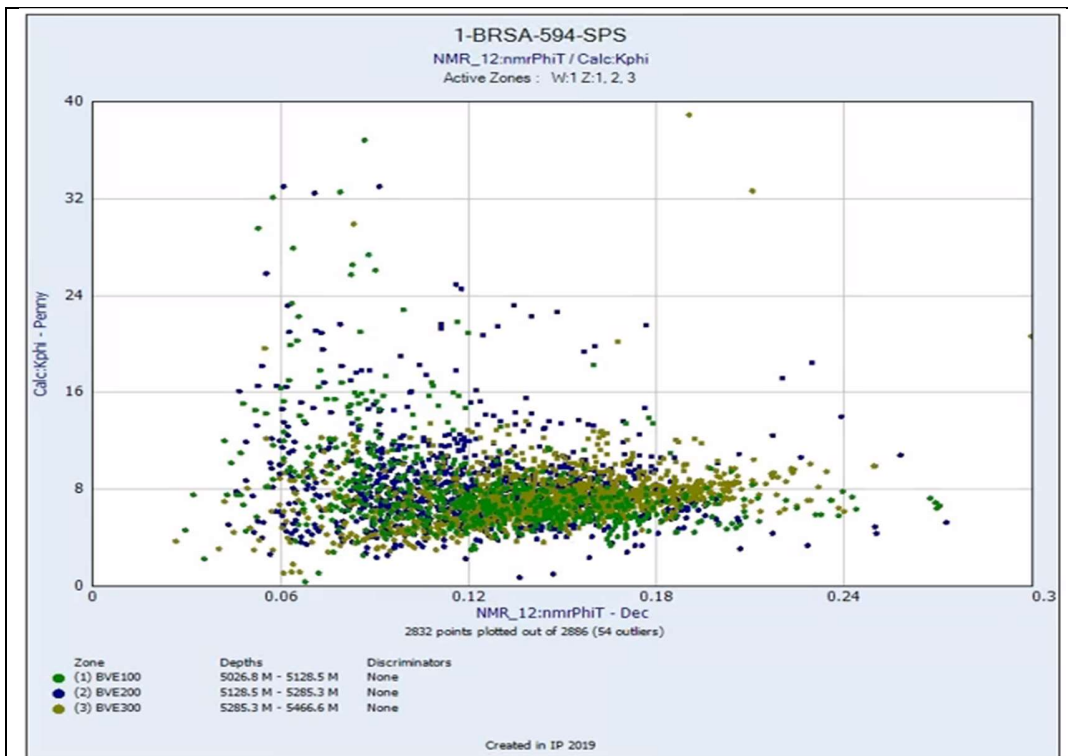


Figure 3.41: Porosity- *Kphi* cross plot for well log analysis for well 1-BRSA-594-SPS. The diverse point colors represent the well zones BVE100, BVE200 and BVE300.

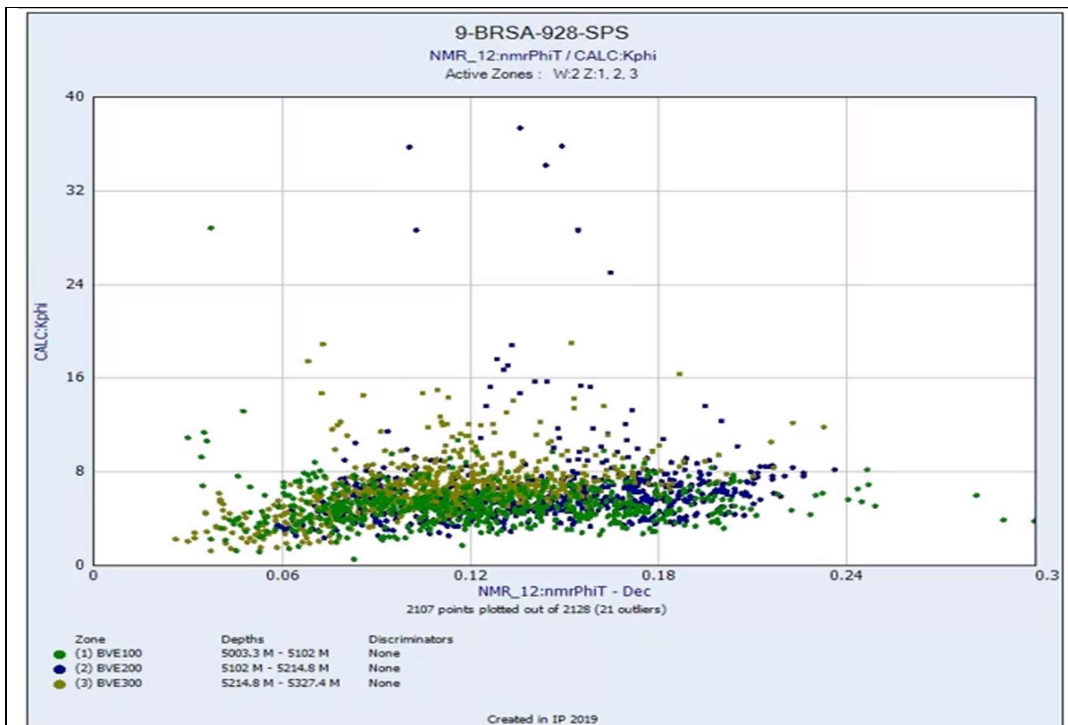


Figure 3.42: Porosity- *Kphi* cross plot for well log analysis for well 9-BRSA-928-SPS. The diverse point colors represent the well zones BVE100, BVE200 and BVE300.

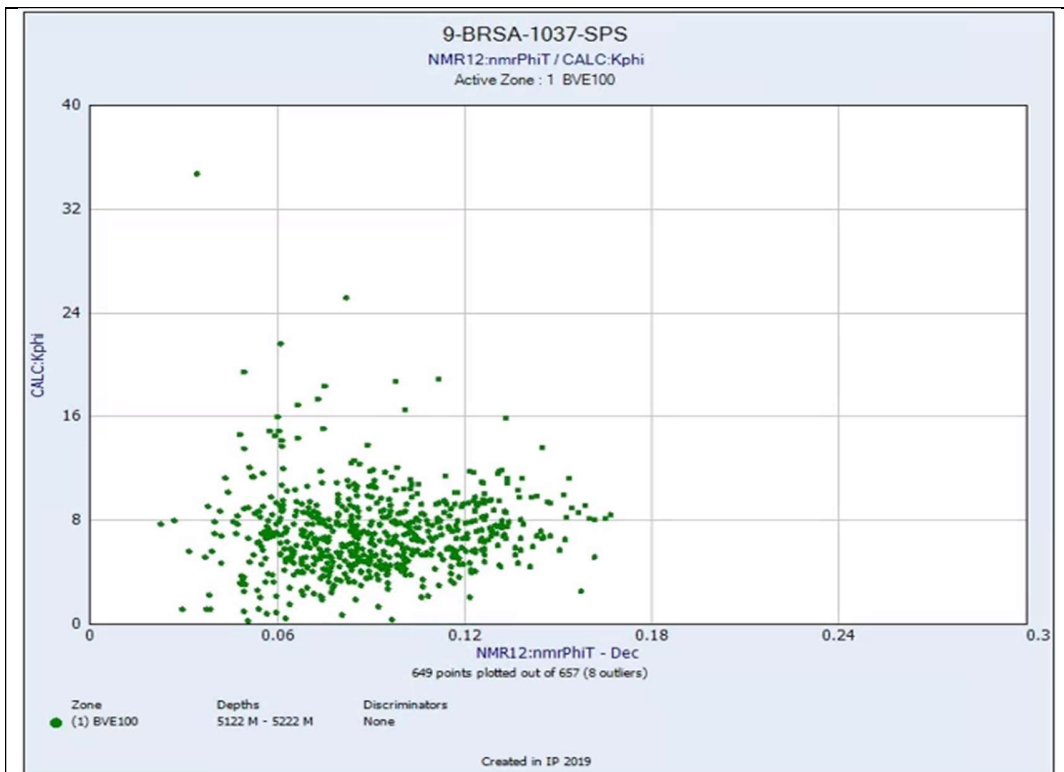


Figure 3.43: Porosity- K_{phi} cross plot for well log analysis for well 9-BRSA-1037-SPS, for zone BVE100

Regarding the core analysis we also produced the total porosity versus K_{phi} cross plots (Figures 3.44 and 3.45). We can observe again a distribution of K_{phi} between 2 GPa and 25 GPa, indicating a variation of pore space geometry. The values are distributed in a similar way that the well log calculations, which indicates consistency between the two methodologies.

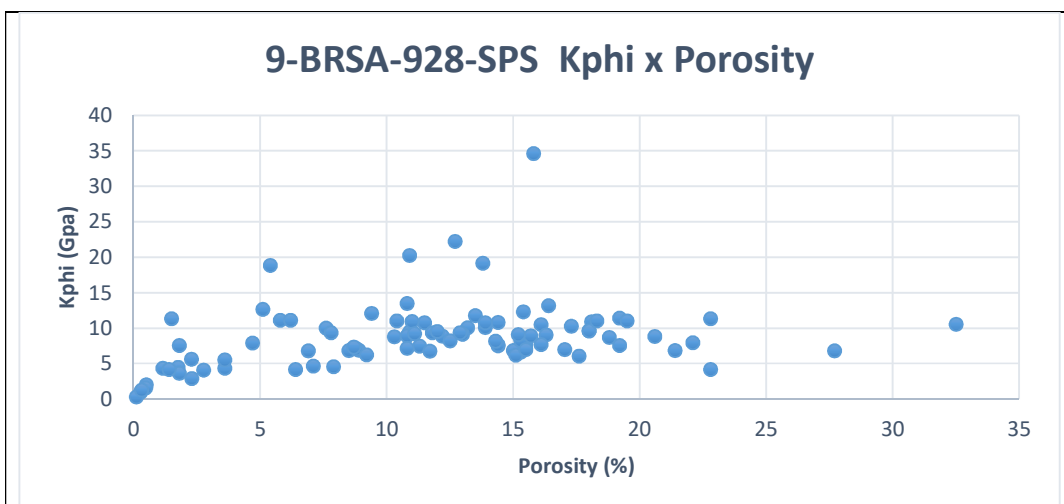


Figure 3.44: Porosity- K_{phi} cross plot for the laboratory analysis for well 9-BRSA-928-SPS.

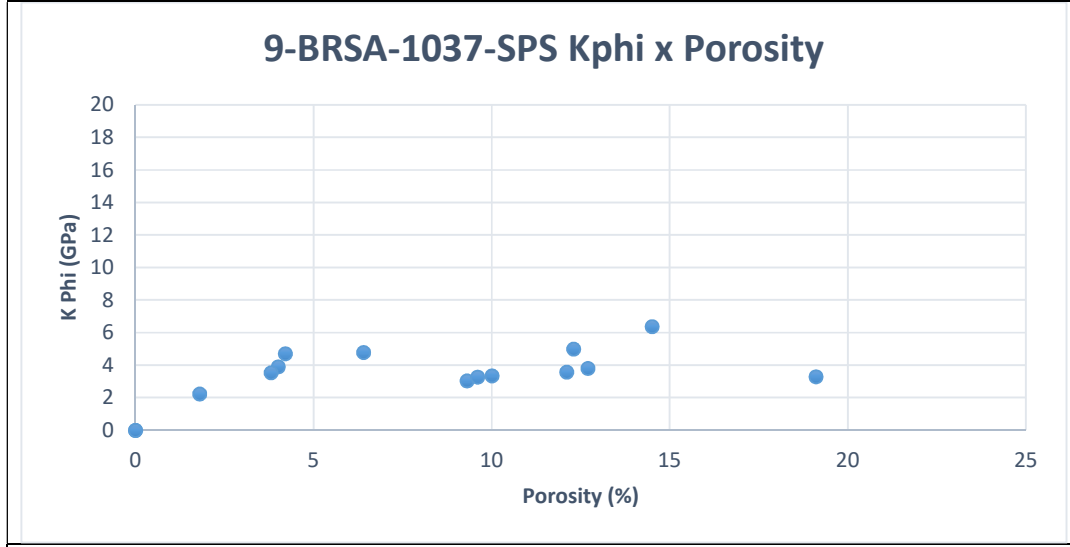


Figure 3.45: Porosity- K_{phi} cross plot for the laboratory analysis for well 9-BRSA-1037-SPS.

3.2.2. Pore stiffness Assessment

3.2.2.1. Methods

To compare the calculated K_{phi} by the core and the logs analysis, different pore geometries were assumed (Zimmerman 1984) and four diverse K_{phi} were calculated with the equations 12, 13, 14 and 15. For the core and log analysis, we calculate the formation poisson ratio ν using the equation 3 and the compressional and shear velocities from core analysis and well logs, respectively. It was obtained then, four outputs values (K_{phi_sphere} , K_{phi_Penny} , K_{phi_Needle} and K_{phi_Tubes}). For K_{phi_Penny} , at first it was assumed an aspect ratio equal to 0.05.

Russel and Smith (2009) developed a practical approach to compare the values of K_{phi} and K_{dry} by using the K_{dry}/K_m ratio. This method assumes that K_{phi} should stay constant over a range of porosities. Therefore, a variation of K_{dry}/K_m ratio for a given porosity would occur if K_{phi} varies, meaning that a different pore geometry is present. The four different K_{phi} calculated previously, were applied on the calculation of K_{dry}/K_m , to observe the presence of diverse pore geometries.

In addition, Babasafari (2020) in a recent paper, extended the pore-space stiffness assessment by incorporating the corresponding volume fraction of each-pore type in the pore-space stiffness equation:

$$\frac{1}{K_{dry}} = \frac{1}{K_m} + \sum_{i=1}^n \frac{V_i \phi}{K_{phi}} \quad \text{Eq.20}$$

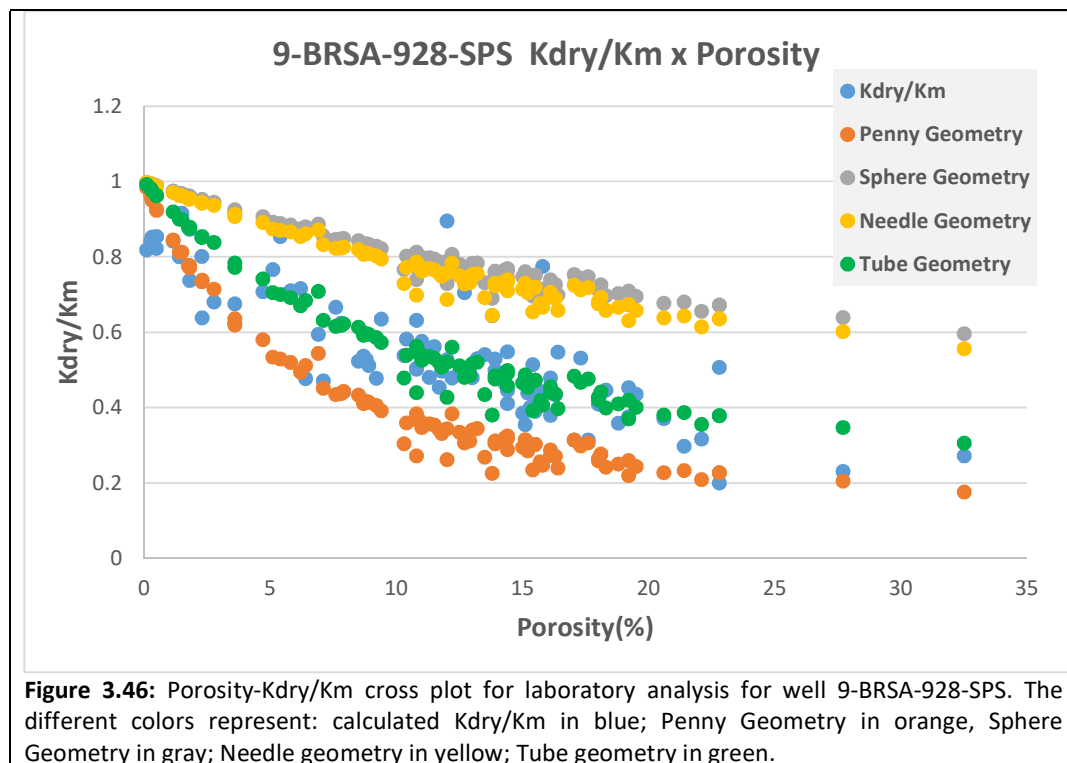
Where V_i is the volume fraction of each pore type.

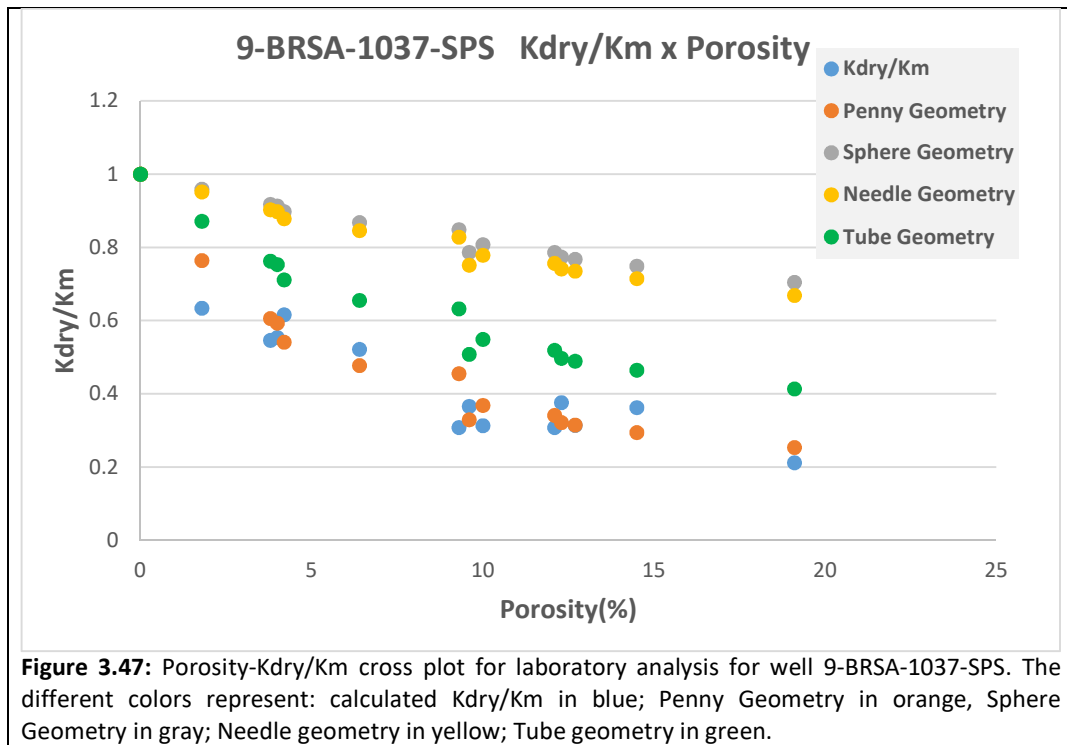
In others words, the authors conclude that the final value of K_{dry} will vary according the amount of each pore type present in the formation. This concept can help us to understand the reasons why K_{phi} values vary not following a particular pore geometry model.

3.2.2.2. Results

For the core analysis data, with the K_{phi} calculated for different pore space geometries, we create four diverse K_{dry}/K_m curves. As discussed, a variation of K_{dry}/K_m ratio for a given porosity would occur if K_{phi} varies, meaning that a different pore geometry is present. From that, we create K_{dry}/K_m versus porosity cross plots (Figures 3.46 and 3.47), with the intention to compare the theoretical geometries with the K_{dry}/K_m calculated with the core data.

It can be observed that K_{dry}/K_m values present different pore-space stiffness, in consequence different pore geometries. For the well 9-BRSA-928-SPS (Figure 3.46), part of point are adjacent to the penny (oblate spheroid) geometry and to sphere geometry, however the majority of the calculate K_{dry}/K_m values have good correlation with the tubes geometry. For the well 9-BRSA-1037-SPS (Figure 3.47), the points are predominantly adjacent to penny geometry.





The same analysis was made for the well logs data, with the calculation of K_{dry}/K_m , and the same geometries were applied with the intention to identify the possible pore geometries.

All the variation observed could also be the result of the presence of multiple pore type, as suggested by Babasafari (2020).

For all wells, it can be observed (Figures 3.48, 3.49 and 3.50) that the majority of the points are adjacent of the penny and tube geometries. Locally also are points plotted in the sphere and needle regions. Once again, this variation can be explained by the presence of more than one pore type simultaneously in the reservoir rocks.

The discussion regarding the variation of pore space geometries and its relation with the porosity types is developed in the section 3.3.

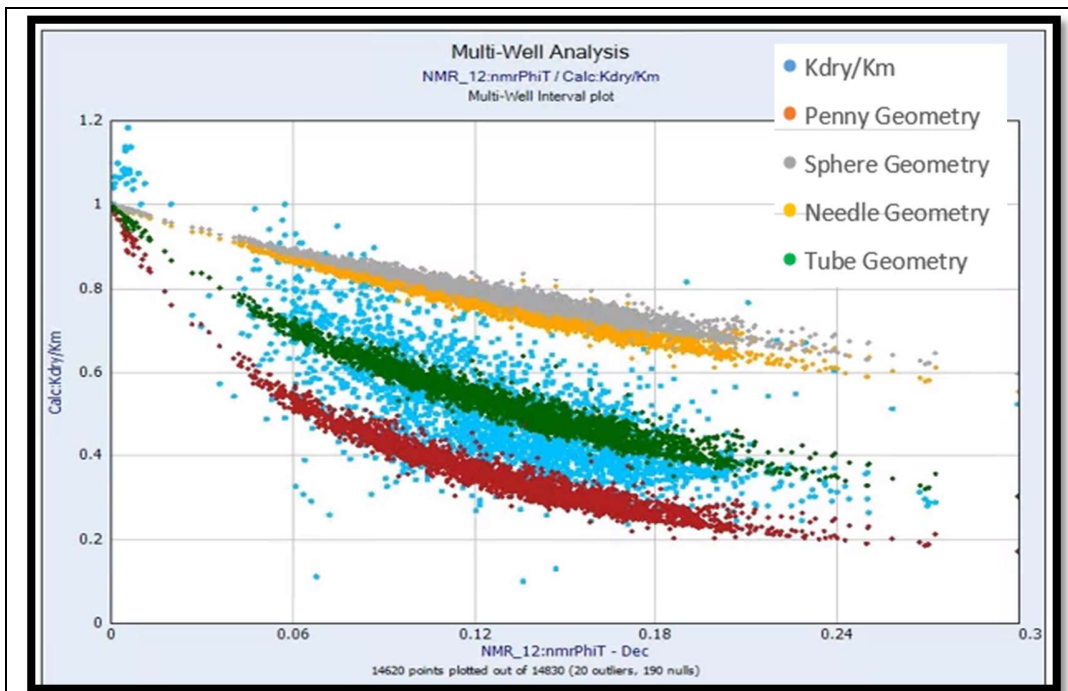


Figure 3.48: Porosity-Kdry/Km cross plot for well log analysis for well 1-BRSA-594-SPS. The different colors represent: calculated Kdry/Km in blue; Penny Geometry in orange; Sphere Geometry in gray; Needle geometry in yellow; Tube geometry in green.

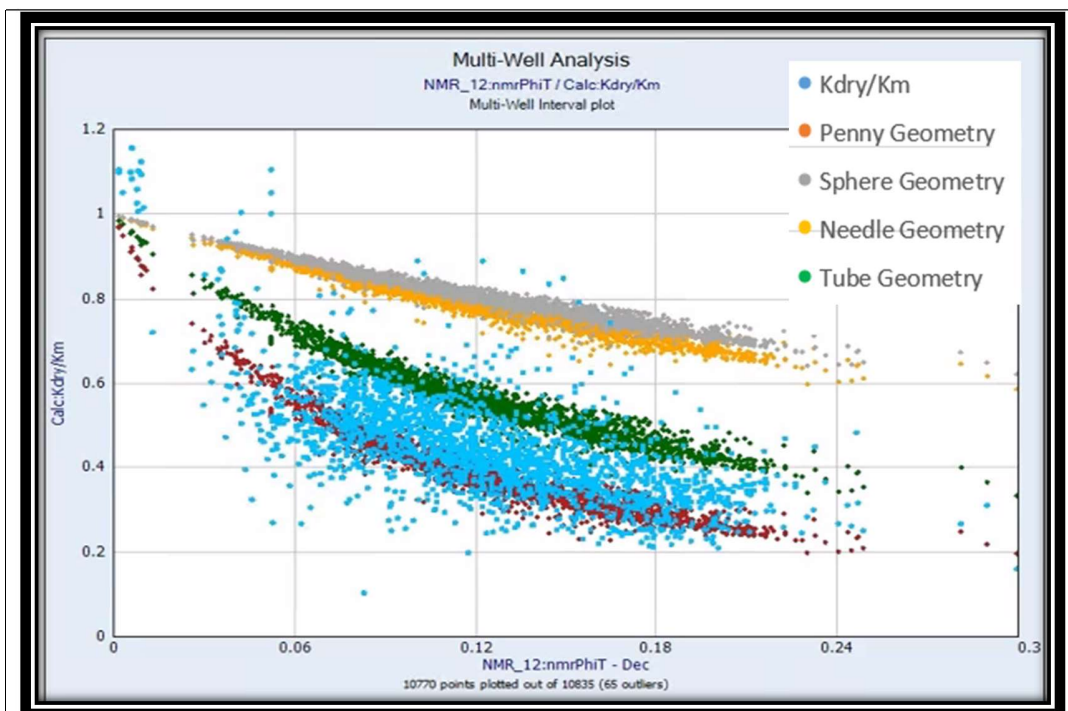


Figure 3.49: Porosity-Kdry/Km cross plot for well log analysis for well 9-BRSA-928-SPS. The different colors represent: calculated Kdry/Km in blue; Penny Geometry in orange; Sphere Geometry in gray; Needle geometry in yellow; Tube geometry in green.

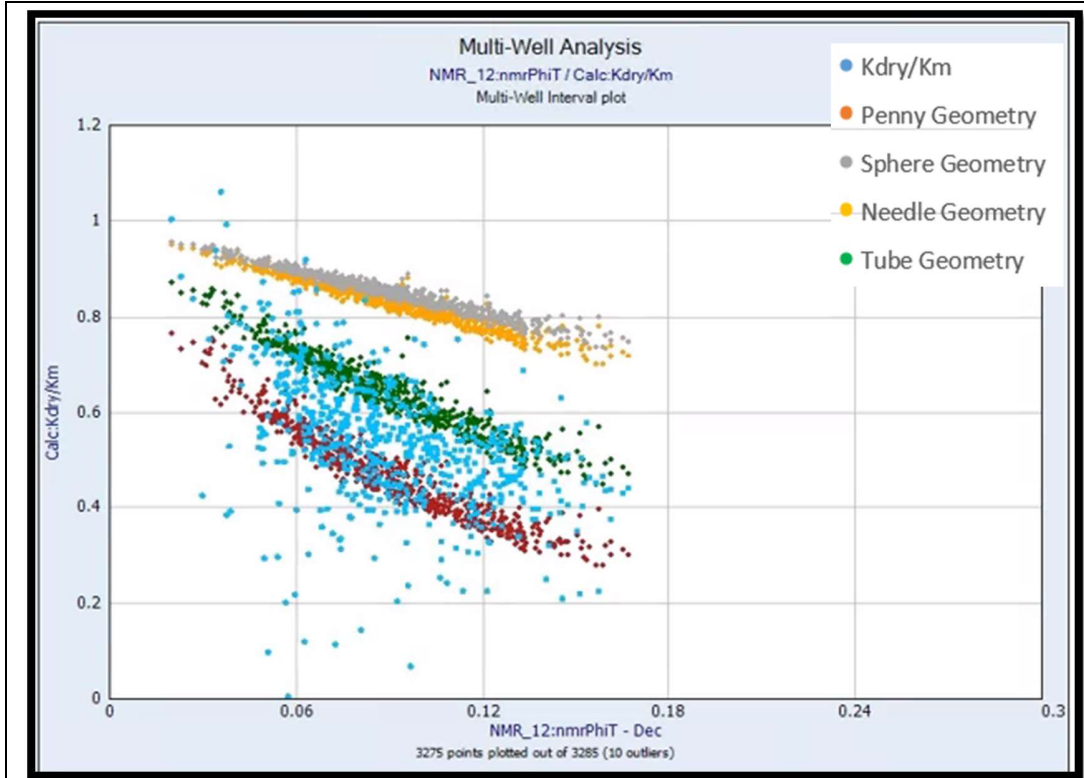


Figure 3.50: Porosity-Kdry/Km cross plot for well log analysis for well 9-BRSA-1037-SPS. The different colors represent: calculated Kdry/Km in blue; Penny Geometry in orange, Sphere Geometry in gray; Needle geometry in yellow; Tube geometry in green.

3.3. Pore Geometry Analysis

To improve the interpretation of the petroelastic model and its relation with the porosity types, the penny geometry was understood as the most representative pore space geometry present. In the previous section, it was calculate a K_{phi} with the penny geometry considering an aspect ratio α equal to 0.05. To improve this comparison between the curves and the wells, we assume that the pore geometry is approximated with the penny (oblate spheroid), and additional curves with aspect ratio α equal to 0.1 and 0.2 were created. As already demonstrated by different authors (Babasafari 2020, Xu and Payne 2009), the higher aspect ratio, the more spherical and stiffer the pores are.

To compare the different aspect ratio curves, we again used the K_{dry}/K_m versus porosity cross plots (Figure 3.51, 3.52 and 3.53), for the well log data. From that, we can verify that our pore system has a reference pore space stiffness that has the oblate spheroid geometry and an aspect ratio between 0.1 and 0.05, predominantly.

Correlating the pore space stiffness, the aspect ratio and the porosity types, we suggest the definition of three different groups, denominated petroelastic classes. The criteria and their features will be explained in section 3.3.1.

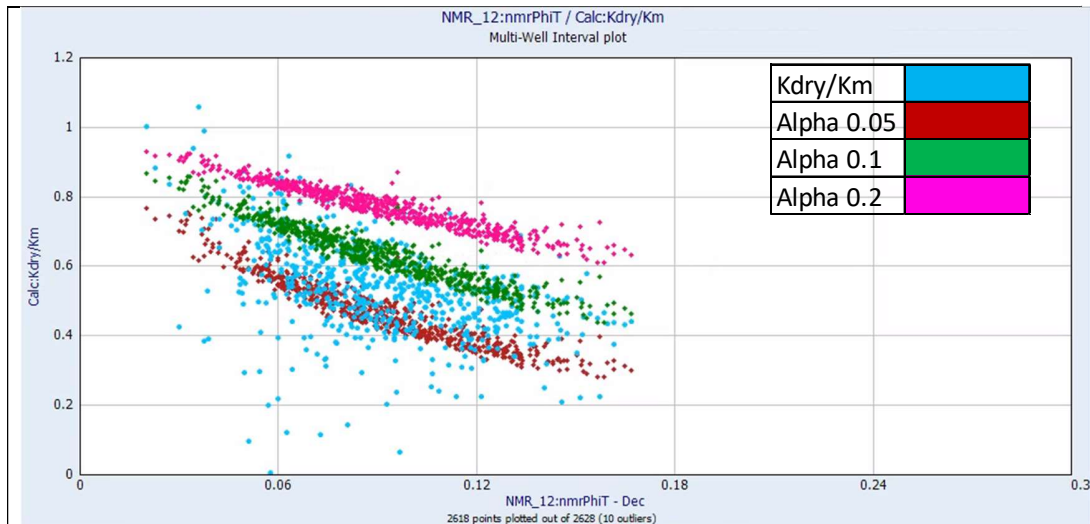


Figure 3.51: Porosity-Kdry/Km cross plot for well log analysis for well 9-BRSA-1037-SPS. The different colors represent: calculated Kdry/Km in blue; aspect ratio equal to 0.05 in red, aspect ratio equal to 0.1 in green and aspect ratio equal to 0.2 in pink.

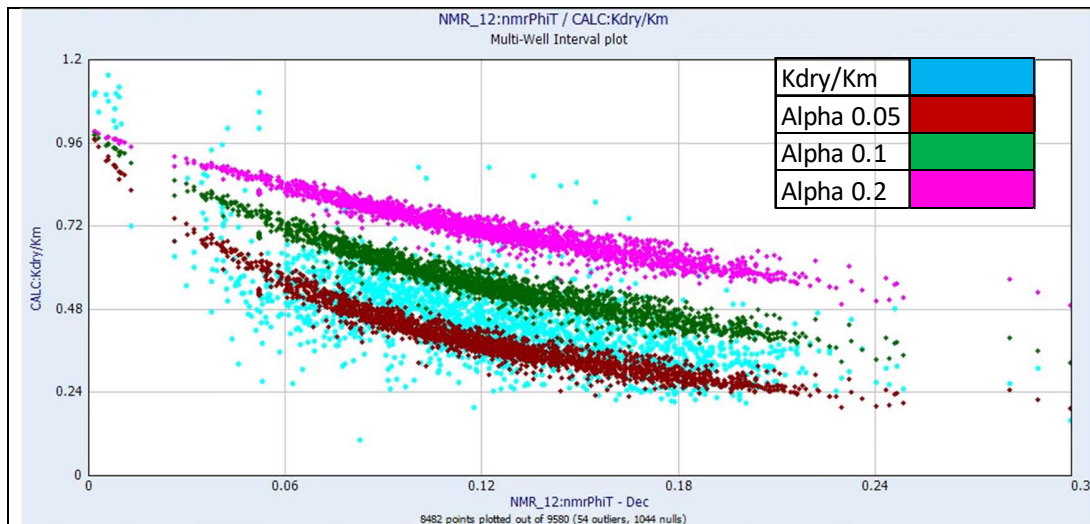


Figure 3.52: Porosity-Kdry/Km cross plot for well log analysis for well 9-BRSA-928-SPS. The different colors represent: calculated Kdry/Km in blue; aspect ratio equal to 0.05 in red, aspect ratio equal to 0.1 in green and aspect ratio equal to 0.2 in pink.

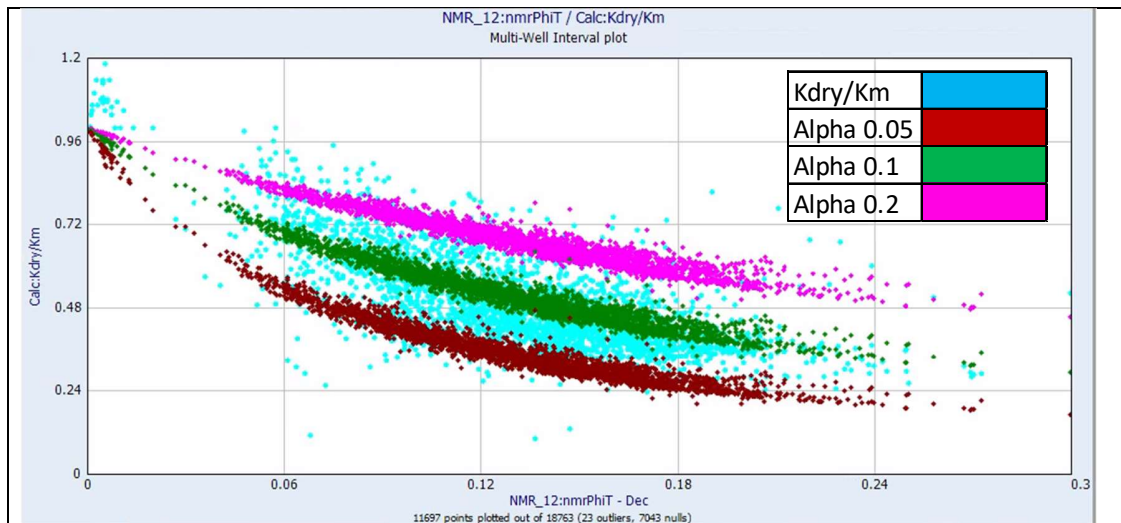


Figure 3.53: Porosity-Kdry/Km cross plot for well log analysis for well 1-BRSA-594-SPS. The different colors represent: calculated Kdry/Km in blue; aspect ratio equal to 0.05 in red, aspect ratio equal to 0.1 in green and aspect ratio equal to 0.2 in pink.

3.4. Petroelastic Classes

By the association of the pore geometry analysis and the pore type identification, it was possible to create groups with similar characteristics. These petroelastic classes are described below.

3.4.1. Petroelastic Class 1

This group is characterized by the K_{phi} aspect ratio between 0.05 and 0.1. We can observe that the pore space is represented by a mixture of different pore geometries and the K_{phi} values are proportional to the pore geometries fractions. It was demonstrated in section 3.1.3 that the pore system is characterized by the interaction of the different porosity types, mainly interparticle and vuggy (touching and separate) porosities. From the petrophysics log analysis, we can observe that this rock class is characterized by positive deviations from velocity deviation curve and presence of vuggy porosity from NMR porosity type curves (Figure 3.54). We can observe by the histogram of T2 logarithmic mean curve (Figure 3.55), that the mean value is 166 mS, indicating the dominance of interparticle porosity and an influence of vuggy porosity that moves the values to the higher values.

From the geology point of view, this class is represented mainly by stromatolites and grainstones facies, with intergranular and interelement porosity, plus a vuggy pore system (touching and/or separate vugs) formed by diagenetic dissolution (Figure 3.56).

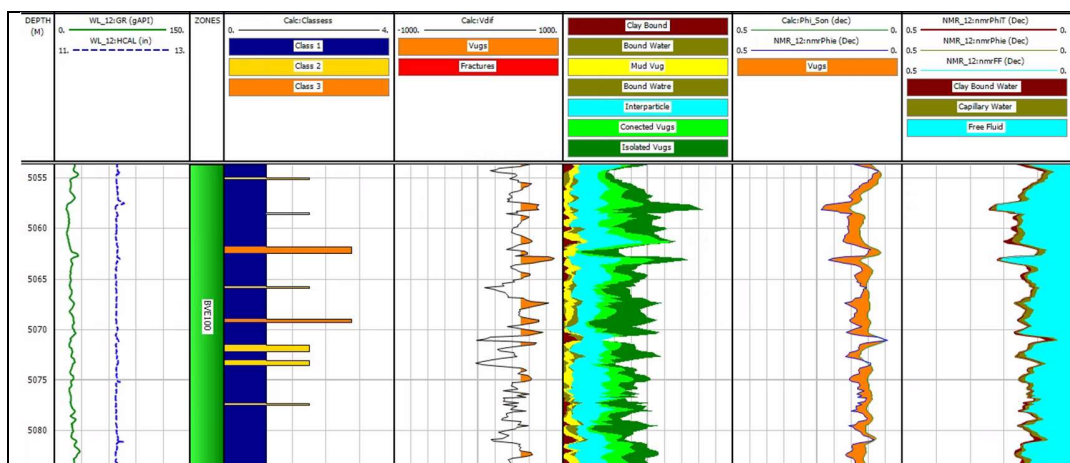


Figure 3.54: Petroelastic class 1 and porosity types logs composite for well 1-BRSA-594-SPS. Track 1: well depth. Track 2: Gamma-Ray (GR) and caliper (HCAL). Track 3: Zonation of well, zone BVE100 in green. Track 4: Petroelastic classes: Class 1 in blue, class 2 in yellow and class 3 in orange. Track 5: Velocity deviation curve. Track 6: Nuclear Magnetic Resonance porosity type curves. Track 7: Secondary porosity curve. Track 8: Nuclear Magnetic Resonance porosity curves, Total porosity (nmrPHIT), Effective porosity (nmrPHIE) and Free Fluid (nmrFF).

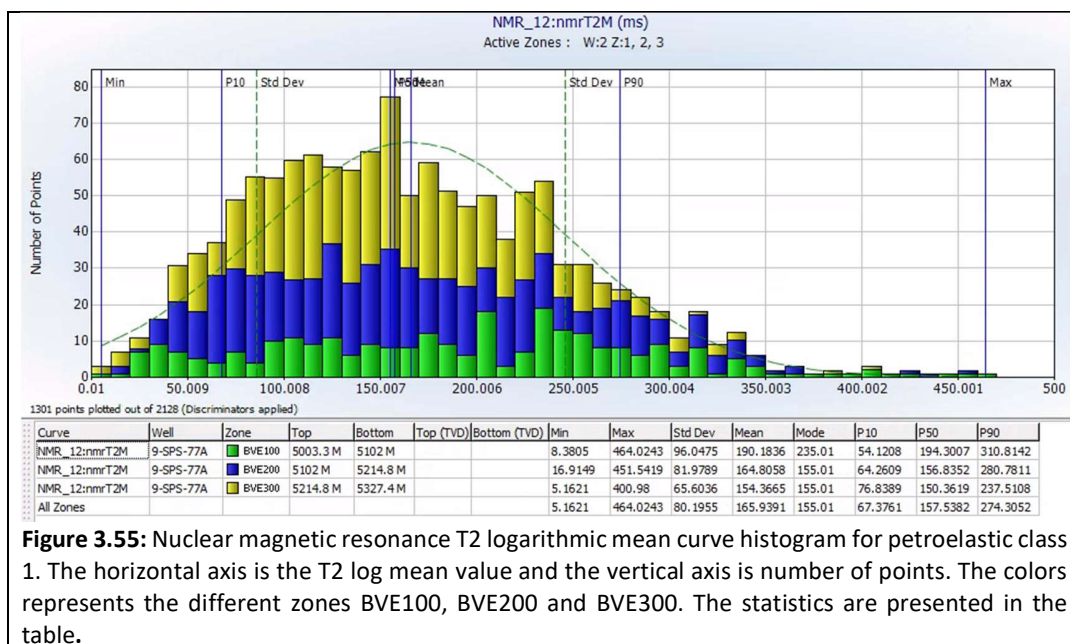
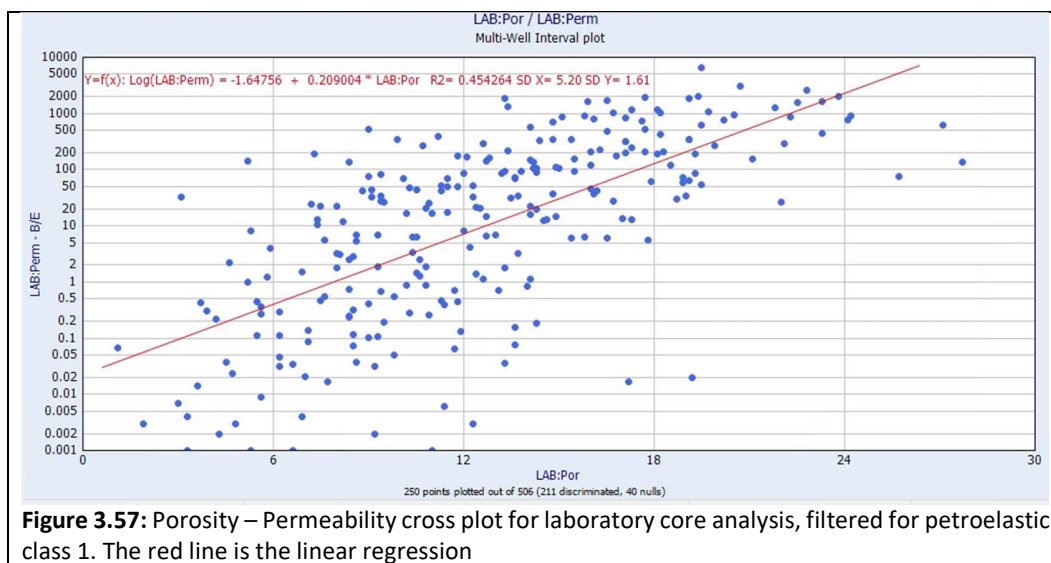
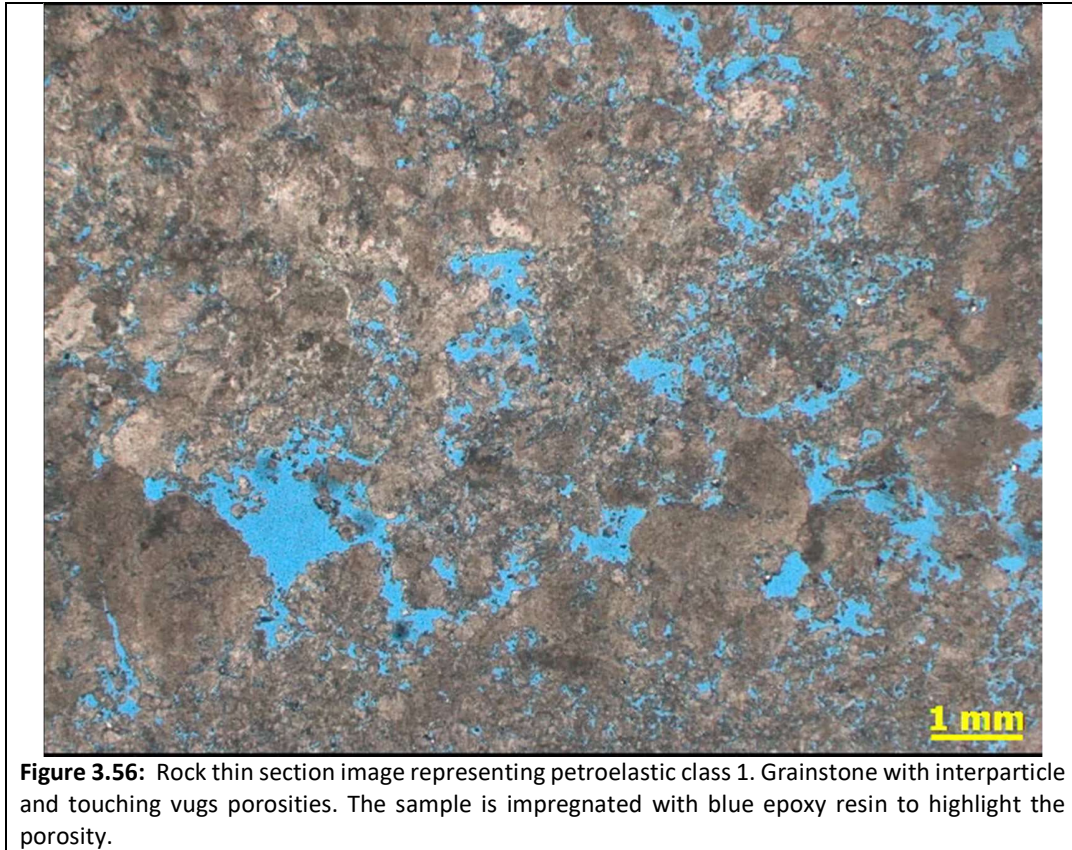


Figure 3.55: Nuclear magnetic resonance T2 logarithmic mean curve histogram for petroelastic class 1. The horizontal axis is the T2 log mean value and the vertical axis is number of points. The colors represents the different zones BVE100, BVE200 and BVE300. The statistics are presented in the table.

The crossplot Porosity x Permeability (Figure 3.57) for the laboratory analysis filtered for this class presents good correlation although it shows a significant scattering of the points. The scattering can be explained by the presence of touching vugs, that will increase the porosity permeability relation, and simultaneously separate vugs, that will decrease the relation. By implementing a linear regression we retrieve an equation of permeability:

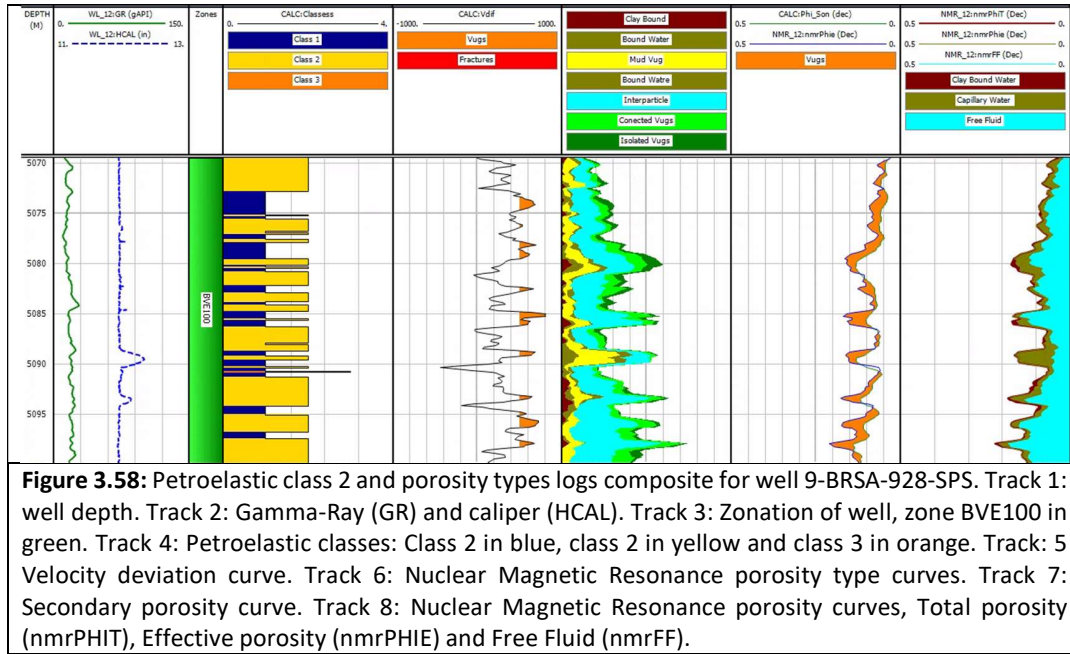
$$\log(\text{perm}) = -1.64756 + 0.209004 * \text{por}$$

Eq.21



3.3.2 Petroelastic Class 2

This class is characterized by a K_{phi} aspect ratio smaller than 0.05. A mixture of different pore geometries, though predominantly by the ellipsoidal geometry, represents this pore space. In contrast with the first, this class must present only a predominant porosity type, mainly the interparticle porosity, with low secondary porosity (Figure 3.58). This group is characterized by neutral deviation from velocity deviation curve and minor presence of vuggy porosity from NMR porosity type curves. The T2M (T2 mean) curve presents a mean value is 139 mS (Figure 3.59), indicating a dominant presence of interparticle porosity and smaller influence of vuggy porosity.



In terms of facies, this class represents stromatolites and grainstones (Figure 3.60), with interelement and intergranular porosities, with low diagenetic dissolution.

Porosity versus permeability (core analysis) cross plot filtered for Class 2 (Figure 3.61) indicates a stronger relationship (lower uncertainty) when compared with class 1, which can be explained by the predominance of one pore system. By applying a linear regression we retrieve:

$$\log(\text{perm}) = -2.50186 + 0.267907 * \text{por} \quad \text{Eq.22}$$

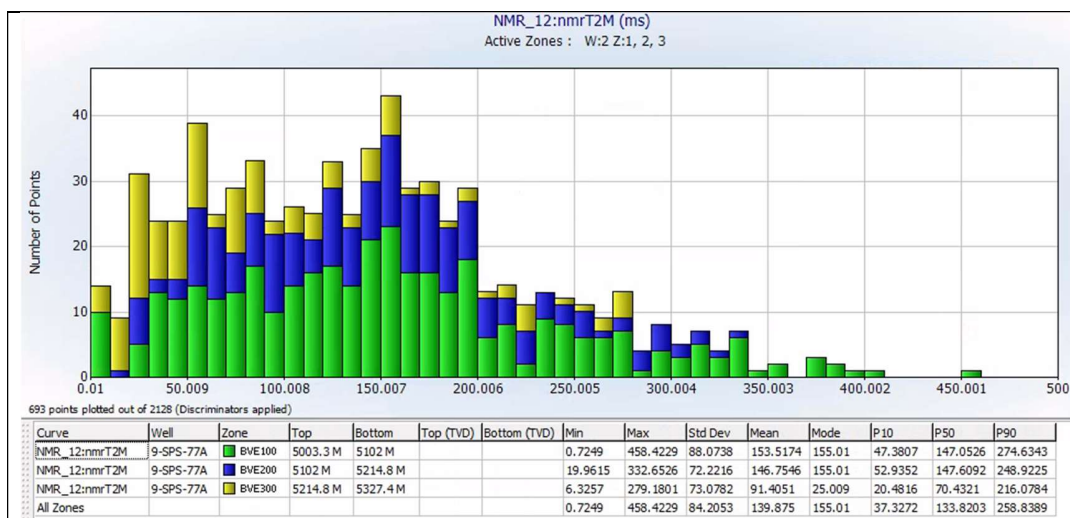


Figure 3.59: Nuclear magnetic resonance T2 logarithmic mean curve histogram for petroelastic class 2. The horizontal axis is the T2 log mean value and the vertical axis is number of points. The colors represents the different zones BVE100, BVE200 and BVE300. The statistics are presented in the table.

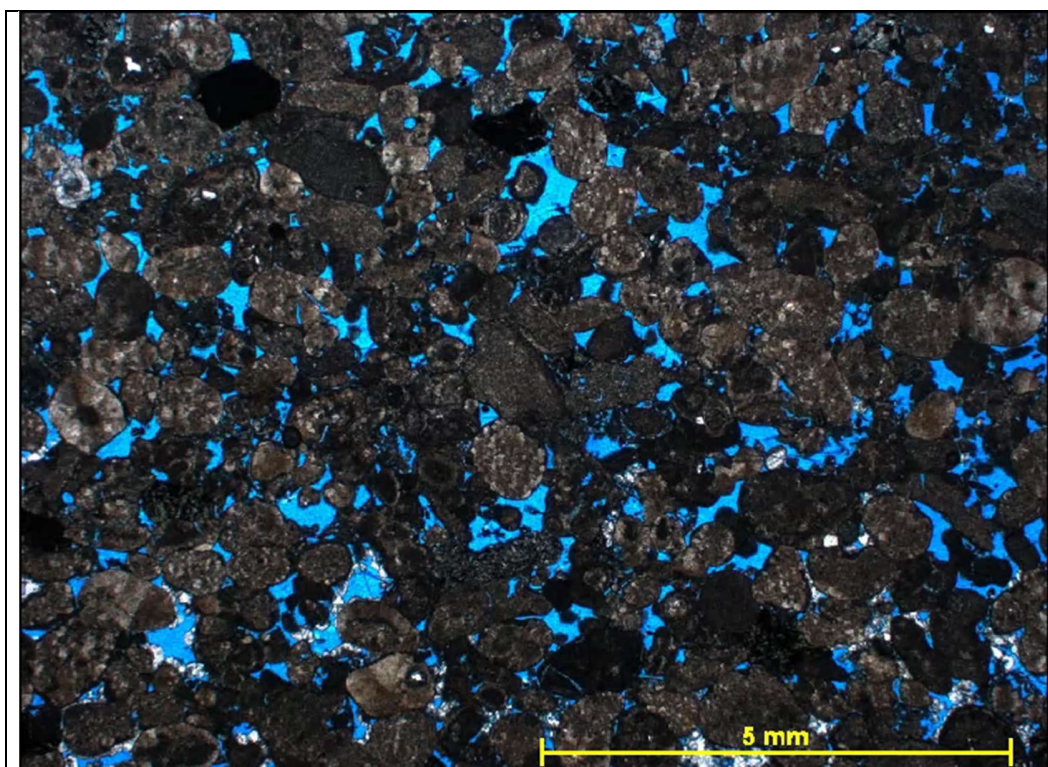
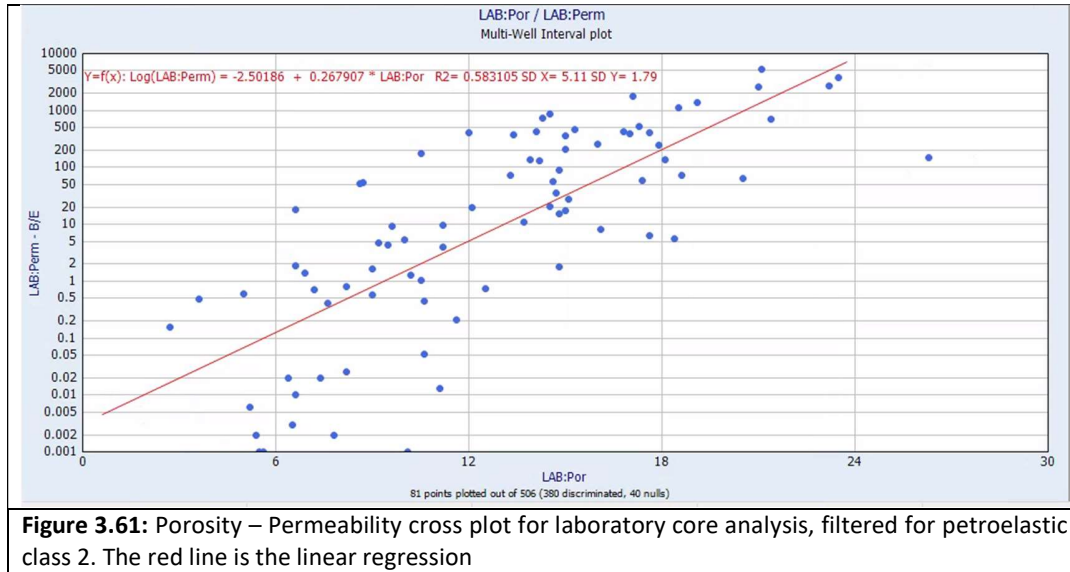


Figure 3.60: Rock thin section image representing petroelastic class 2. Grainstone with interparticle porosity. The sample is impregnated with blue epoxy resin to highlight the porosity.



3.3.3 Petroelastic Class 3

This class is represented by K_{phi} with an aspect ratio higher than 0.1. This pore space represents rocks with a relevant volumetric contribution of circular (less ellipsoidal) pores. This class is characterized mainly by presence of secondary vuggy porosity.

The histogram of T2M curve (Figure 3.63) indicates a mean value of 202Ms, what demonstrates the presence of interparticle porosity and a strong influence of vuggy porosity, dislocating the values to the right. It also presents positives deviations at velocity deviation curve and vuggy porosity in NMR porosity types curve (Figure 3.62). In addition, some intervals indicates presence of the *MudVugs* in NMR porosity curves, which can be related with the presence of big vugs filled with drilling fluid (figure 3.62).

This pore space may be formed by clasts dissolution in grainstones (moldic porosity), intraelement dissolution in stromatolites and spherulitites, or intense porosity enlargement of other facies (Figure 3.64).

Analyzing the permeability-porosity (core analysis) cross plot filtered for the Class 3 (Figure 3.65), we observe a strong correlation which indicates a homogeneous pore system. Applying the linear regression for the core analysis of class 3, we retrieve:

$$\text{Log}(\text{perm}) = -1.55782 + 0.192354 * \text{por} \quad \text{Eq.23}$$

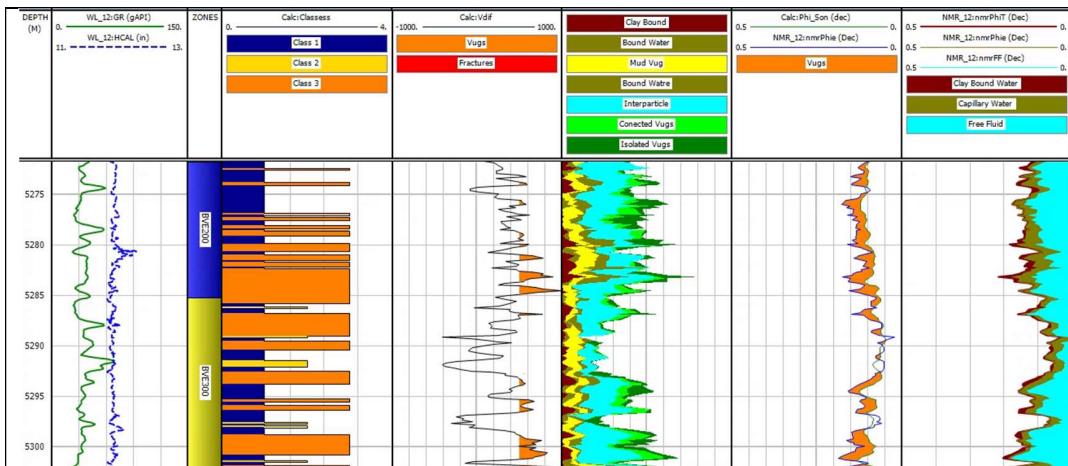


Figure 3.62: Petroelastic class 3 and porosity types logs composite for well 1-BRSA-594-SPS. Track 1: well depth. Track 2: Gamma-Ray (GR) and caliper (HCAL). Track 3: Zonation of well, zone BVE100 in green. Track 4: Petroelastic classes: Class 2 in blue, class 2 in yellow and class 3 in orange. Track: 5 Velocity deviation curve. Track 6: Nuclear Magnetic Resonance porosity type curves. Track 7: Secondary porosity curve. Track 8: Nuclear Magnetic Resonance porosity curves, Total porosity (nmrPHIT), Effective porosity (nmrPHIE) and Free Fluid (nmrFF).

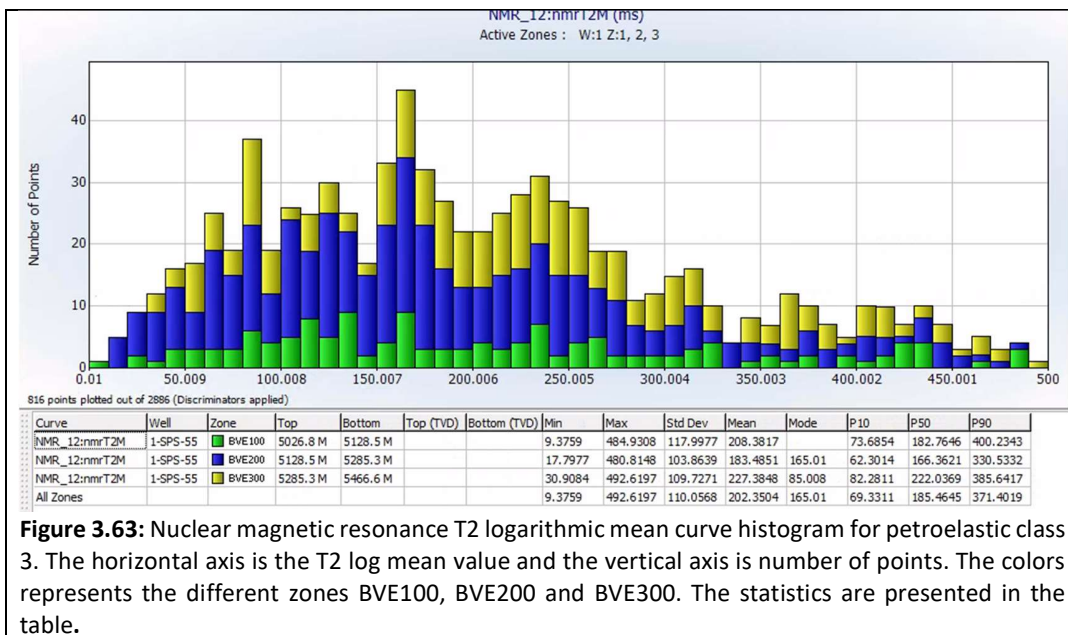


Figure 3.63: Nuclear magnetic resonance T2 logarithmic mean curve histogram for petroelastic class 3. The horizontal axis is the T2 log mean value and the vertical axis is number of points. The colors represents the different zones BVE100, BVE200 and BVE300. The statistics are presented in the table.

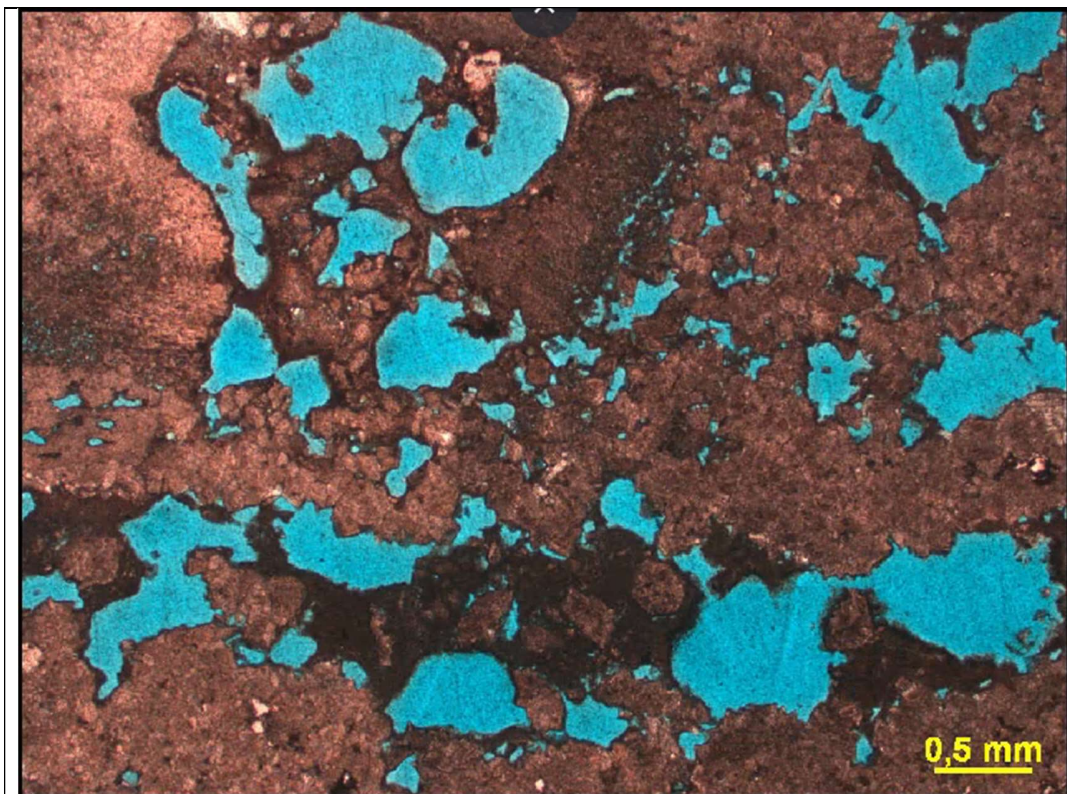


Figure 3.64: Rock thin section image representing petroelastic class 3. Grainstone with big touching and separate vugs porosities. The sample is impregnated with blue epoxy resin to highlight the porosity.

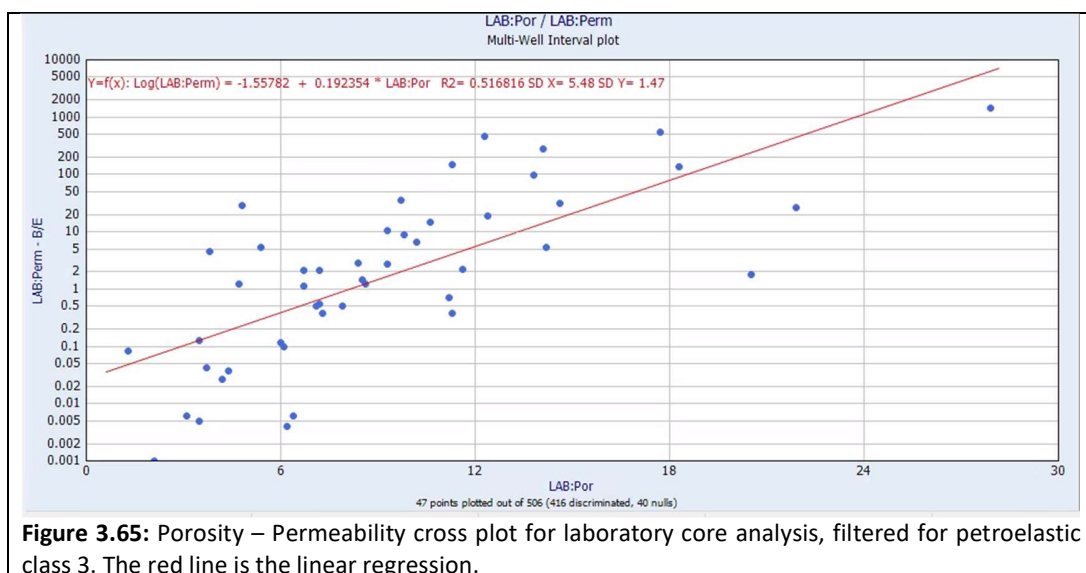


Figure 3.65: Porosity – Permeability cross plot for laboratory core analysis, filtered for petroelastic class 3. The red line is the linear regression.

3.3.4 Permeability Prediction

After developing the porosity-permeability relationship (Eq.21, Eq.22 and Eq.23) for all petroelastic facies, it was possible to calculate and predict a permeability curve. In addition, we consider that the standard deviation indicates how far the data points are from the regression line on average. From that, it was calculated an upper and a lower limit curves that create an envelope of high permeability probability. These curves were calculated and compared with the values of permeability derived from the routine core analysis. The results can be seen in the figure 3.62 and 3.63. When compared with the permeability curve derived from the NMR processing, we see that the calculated permeability curve presents a stronger correlation with the core analysis. The majority of values are included inside the permeability envelope.

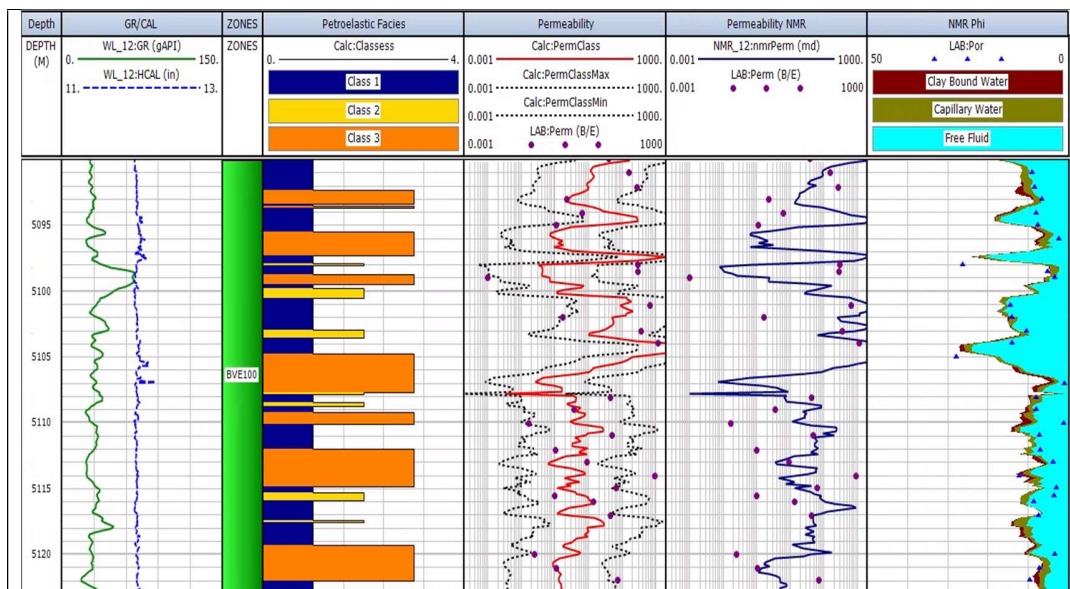


figure 3.66: Petroelastic classes and permeability curves logs composite for well 1-BRSA-594-SPS. Track 1: well depth. Track 2: Gamma-Ray (GR) and caliper (HCAL). Track 3: Zonation of well, zone BVE100 in green. Track 4: Petroelastic classes: Class 2 in blue, class 2 in yellow and class 3 in orange. Track: 5 Calculated, lower limit and upper limit permeability curves for petroelastic classes and permeability for routine core analysis. Track 6: Nuclear Magnetic Resonance permeability curves. Track 7: Nuclear Magnetic Resonance porosity curves, Total porosity (nmrPHIT), Effective porosity (nmrPHIE) and Free Fluid (nmrFF). Track 8: Nuclear Magnetic Resonance T2 distribution.

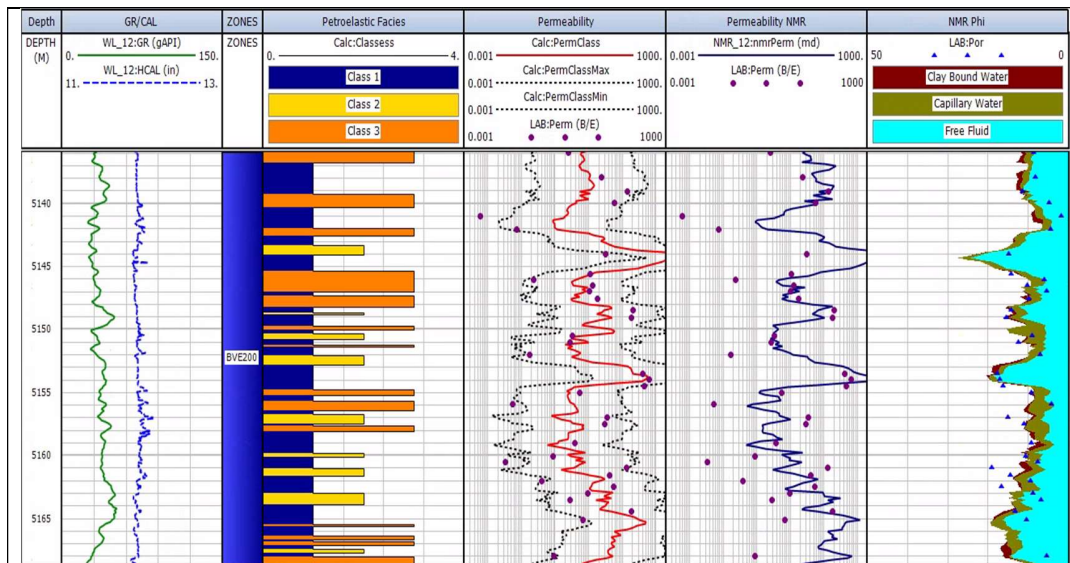


Figure 3.67: Petroelastic classes and permeability curves logs composite for well 1-BRSA-594-SPS. Track 1: well depth. Track 2: Gamma-Ray (GR) and caliper (HCAL). Track 3: Zonation of well, zone BVE100 in green. Track 4: Petroelastic classes: Class 2 in blue, class 2 in yellow and class 3 in orange. Track 5: Calculated, lower limit and upper limit permeability curves for petroelastic classes and permeability for routine core analysis. Track 6: Nuclear Magnetic Resonance permeability curves. Track 7: Nuclear Magnetic Resonance porosity curves, Total porosity (nmrPHIT), Effective porosity (nmrPHIE) and Free Fluid (nmrFF). Track 8: Nuclear Magnetic Resonance T2 distribution.

4. Conclusion

The evaluation of the pre-salt reservoir in the region of the Sapinhoá is not a simple mission. This reservoir is characterized by diverse geological facies, variety of porosity types, complex mineralogy distribution and particularly difficulty in predict permeability. These properties are very relevant to be correctly described, not only to improve the understanding of the geologic process but also to perform a great reservoir characterization.

The techniques develop in this thesis proved useful and coherent to predict reservoir properties. The methodology of working with different sets of data (well logs and core analysis) in an integrated form, proved to be effective and, more important, cross validated the results.

When analyzing the mineral composition, we saw that X-ray diffraction analysis are useful to characterize the mineralogy of the rocks samples. In addition, the elemental spectroscopy log is also an alternative to estimate correctly the compositional variety. These techniques assisted us to identify that mainly the minerals Calcite, Dolomite and Quartz compose the reservoir. Following the logging petrophysical evaluation, after characterizing the mineralogy of the rocks, it is possible to perform a porosity estimation.

Another important step is to perform the characterization of the porosities types were different techniques, using sonic and NMR logs for instance, presents the variety of pore system in the well rocks. It was identified that the well rocks present a mixture of porosity types, predominantly interparticle, separate and touching vugs.

Regarding the petroelastic model, we see that the pore space stiffness method (Mavko & Mukerij, 1995) can be applied to proper understand the variation of rock elastic moduli, although part of the theory had been developed for low porosity rocks. Particularly, models of pore space stiffness that appreciate the variety of pores geometries (Zimmerman 1984 & 1991) can show and differentiate different aspects of the reservoir rocks. We saw that the pore space could be approximated with the penny geometry.

The prediction of pore space geometry, by the pore space stiffness assessment, particularly with the K_m/K_{dry} cross plots, shown to be much effective to separate diverse rocks portions. Particularly, by the manipulation of the aspect ratio, the reservoir can be divided in three different dominant pore geometries that can be associated with the porosity types.

Therefore, combining the pore space geometries and the porosity types model we generated a proposition of three diverse petroelastic classes. These facies represent

different porosity types associations, diverse log identities and mostly important, three unique equations to predict the permeability of the reservoir.

The predicted permeability curves can be immediately applicated in the reservoir modelling, with the intention to decrease the permeability uncertainty.

This analysis can be extended to others wells in the Sapinhoá Field, as also to other fields in the Pre-salt province. Particularly, the petroelastic classes could be more particularized and correlated with studies of rock typing as well to sedimentology and diagenetic studies. This could even produce a permeability model with fewer uncertainties. In particular, the pore space stiffness assessment could be applied in a higher variety of carbonate sedimentary facies to develop a more consistent model.

Considering all the investigation, we must take into account that some uncertainties can affect the analysis. Firstly, it was assumed that only three minerals were present in the reservoir analyzed, therefore, local changes in mineralogy were neglected, and their occurrence may introduce errors in the assumed model. Secondly, the uncertainties regarding the laboratory analysis measurements and the logging vertical resolution represent an adding of inaccuracies that may affect again the results. Finally, for the petroelastic model, some moduli were assumed as constants; however, they could have minor variations due to temperature and pressures changes. From that, a computational model, that include the more minerals, temperature and pressure variations, and inaccuracies can be future developed.

REFERENCES

- American Petroleum Institute (1998). Recommended Practices for Core Analysis: Exploration and Production Department, Recommended practice 40, 2nd ed.
- Anselmetti, F. S. & Eberli, G. P. (1999). The velocity-Deviation log: A tool to predict pore type and permeability trends in carbonate drill holes from sonic and porosity or density logs. *American Association of Petroleum Geologists*, V 83, No 3, 450-466.
- Babasafari, A. A., Bashir, Y., Ghosh, D. P., Salim, A. M. A., Janjuhah, H. T., Kazemeini, S. H. & Kordi, M. (2020). A new approach to petroelastic modeling of carbonate rocks using an extended pore-space stiffness method, with application to a carbonate reservoir in Central Luconia, Sarawak, Malaysia. *The Leading Edge*, Volume 39, Issue 8, 592a1-592a10, <https://doi.org/10.1190/tle39080592a1.1>.
- Biot, M.A., (1956). Theory of propagation of elastic waves in a fluid-saturated porous solid(I. Low frequency range). *J. Acoust. Soc. Am.* 28 (2), 168-178.
- Chang, H.K., Kowsmann, R.O., Figueiredo, A.M.F., Bender, A. (1992). Tectonics and stratigraphy of the East Brazil Rift system: an overview. *Tectonophysics* 213 (1), 97-138.
- Choquette P.W. & Pray, L.C. (1970). Geologic nomenclature and classification of porosity in sedimentary carbonates. *AAPG Bulletin* 54, 2:207–250.
- Dunham, R. J. (1962). Classification of Carbonate Rocks According to Depositional Textures. In *M 1: Classification of Carbonate Rocks—A Symposium*, vol. 38, pp. 108–121. AAPG.
- Ellis, D. V. & Singer, J. M. (2007). *Well Logging for Earth Scientist*. Springer, Dordrecht, The Netherlands, 2nd ed. ISBN 978-1-4020-4602-5
- Faria, D. L. P., Reis, A. T., Souza Jr, O. G. (2017). Three-dimensional stratigraphic-sedimentological forward modeling of an Aptian carbonate reservoir deposited during the sag stage in the Santos basin, Brazil. In *Marine and Petroleum Geology*, December, 88 (2017): 676-695.
- Gassmann, F., (1951). Elastic waves through a packing of spheres. *Geophysics* 16, 673-685.
- Garing, C. (2012). Caractérisation géophysique et géochimique des interactions uide-roche à l'interface eau douce-eau salée : cas des carbonates récifaux de Majorque. *Géophysique [physics.geo-ph]*. Université Montpellier 2, 2011. <https://tel.archives-ouvertes.fr/tel-00767152>

- Gebrande, H., Kern, H., Rummel, F., (1982). Elasticity and inelasticity. In: Hellwege, K.-H. (Ed.), Landolt-Börnstein Numerical Data and Functional Relationships in Science and Technology, New Series, Group V. Geophysics and Space Research, vol. 1, Physical Properties of Rocks, subvol. B. Springer-Verlag, Berlin, pp. 1-233.
- Gomes, J. P., Bunevich, R. B., Tedeschi, L. R., Tucker M. E. & Whitaker, F. F. (2019). Facies classification and patterns of lacustrine carbonate deposition of the Barra Velha Formation, Santos Basin, Brazilian Pre-Salt. In *Marine and Petroleum Geology*, 113 (2020): 1-21. <https://doi.org/10.1016/j.marpetgeo.2019.104176>.
- Gregory, A. R. & Podio, A. L. (1970). Dual-mode ultrasonic apparatus for measuring compressional and shear wave velocities of rock samples. *IEEE : Transactions on sonic and ultrasonics*, Vol. su-17, no- 2, April 1970, 77-85
- Hill, R., (1952). The elastic behavior of crystalline aggregate. *Proc. Phys. Soc., London A*, 65, 349–354.
- Lønøy, A. (2006). Making sense of carbonate pore systems. *AAPG Bulletin* 2006;; 90 (9): 1381–1405. <https://doi.org/10.1306/03130605104>
- Lucia, F. J. (1983). Petrophysical parameters estimated from visual description of carbonate rocks: a field classification of carbonate pore space. *J Pet Technology* March: 626–637
- Lucia, F. J. (1995). Rock-Fabric/Petrophysical Classification of Carbonate Pore Space for Reservoir Characterization. *AAPG Bulletin*, 79(9):1275–1300.
- Lucia, F. J. (2007). Carbonate reservoir characterization: an integrated approach. Springer, Berlin ; New York, 2nd ed. ISBN 978-3-540-72740-8.
- Mavko, G., Mukerji, T. & Dvorkin. J. (2009). The rock physics handbook: Cambridge University Press, <https://doi.org/10.1017/CBO9780511626753>
- Mavko, G. & Mukerji, T. (1995). Seismic pore space compressibility and Gassmann's relation. *Geophysics*, Vol 60, No 6, 1743-1749.
- Mohriak, W., Nemcok M., Enciso G., (2008) South Atlantic divergent margin evolution: rift-border uplift and salt tectonics in the basins of SE Brazil, *Geological Society Special Publication*, London, 294, p 365-398. doi.org/10.1144/SP294.19
- Moreira, J.L.P., Madeira, C.V., Gil, J.A., Machado, M.A.P., (2007). Bacia de Santos. *Boletim de Geociências da Petrobras*, Rio de Janeiro vol. 15 (2), 531e549.
- Naveiro, J. T. & Haimson, D. (2015). Sapinhoá Field, Santos Basin Pre-Salt: From conceptual design to project execution and results, *Offshore Technology Conference*, Brazil, 27-29 October, 2015. 10.4043/26320-MS.

Reuss, A., (1929). Berechnung der Fließgrenze von Mischkristallen. *Angew. Mathem. Mech.* 9, 49-58.

Russell, B., and Smith, T. (2007). The relationship between dry rock bulk modulus and porosity — An empirical study: CREWES Research Report, 19, 1–14.

Schon, J. H. (2011). *Physical properties of rocks: A Workbook*. Elsevier B. V. *Handbook of petroleum exploration and Production*, V 8. ISBN:978-0-444-53796-6

Terra, G.G.S., Spadini, A.R., Franca, A.B., Sombra, C.L., Zambonato, E.E., da Silva Juschaks, L.C., Arienti, L.M., Erthal, M.M., Blauth, M., Franco, M.P., Matsuda, N.S., Carramal da Silva, N.G., Moreti Junior, P.A., D’Avila, R.S., Souza, R.S., Tonietto, S.N., Anjos, S.M.C., Campinho, V.S., Winter, W.R., (2010). Classificacao de rochas carbonaticas aplicavel as bacias sedimentares brasileiras. *Bol. Geociencias Petrobras* 18, 9e29.

Timoshenko, S. P. & Goodier, J. N. (1934). *Theory of Elasticity*. McGraw-Hill Book Company, Ed 3.

Victor, R. A. (2017). Multiscale, image-based interpretation of well logs acquired in a complex, deepwater carbonate reservoir. Ph.D Dissertation, Univ. of Texas, Austin

Voigt, W., (1910). *Lehrbuch der Kristallphysik*. Teubner-Verlag, Leipzig.

Wyllie, M.R.J., Gregory, A.R., Gardner, L.W., (1956). Elastic wave velocities in heterogeneous and porous media. *Geophysics* 21, 4170.

Xu, S., and Payne, M. A. (2009). Modeling elastic properties in carbonate rocks. *The Leading Edge*, 28, no. 1, 66–74, <https://doi.org/10.1190/1.3064148>.

Zimmerman, R. W., (1984). The effect of pore structure on the pore and bulk compressibilities of consolidated sandstones, Ph.D. thesis, Univ. of Calif., Berkeley, 1984.

Zimmerman, R. W., (1991). *Compressibility of Sandstones*: Elsevier Science Publ.